

**Applications of Finite Element Analysis to  
Model and Understand the Complexities of Muscle  
in Clinically Relevant Scenarios**

A DISSERTATION PRESENTED TO THE FACULTY OF THE SCHOOL OF  
ENGINEERING AND APPLIED SCIENCE OF THE UNIVERSITY OF VIRGINIA

IN PARTIAL FULFILLMENT OF THE REQUIREMENT OF THE DEGREE OF  
DOCTOR OF PHILOSOPHY IN BIOMEDICAL ENGINEERING

MATTHEW D. DISALVO

March 29, 2023

This dissertation is submitted in partial fulfillment of the requirements for the degree of:

Doctor of Philosophy

Author: Matthew DiSalvo

COMMITTEE:

CHAIR: George Christ, Ph.D.

ADVISOR: Silvia Blemker, Ph.D.

Jason Kerrigan, Ph.D.

Kazlin Mason, Ph.D.

Niccolo Fiorentino, Ph.D.

## Acknowledgements

Inevitably, at the end of a long journey, one looks back on the path they've traveled and sees that while the destination is their own, they did not travel alone. If I were to thank each and every individual who guided me to this point, the list would no doubt be longer than this dissertation. To those unmentioned, know that your kindness and patience have had a profound influence on the course of my life, and without you I would not have arrived at this point. There are those, of course, who I would like to directly thank, for having a considerable impact on the completion of this dissertation.

Silvia, I owe an unrepayable debt to the mentorship you have shown me over the last 5+ years. You managed to sneak me into a recruitment visit at the last minute, despite there being any number of reasons not to. When I recall our first meeting with you and the M3 lab, all I can remember the feeling of infectious joy you and your students had for the science you were doing. Somehow, despite my best efforts at disorganization, you have managed to face down my chaos with endless enthusiasm and patience, encouraging me to explore my ideas and chart my own path, but also reining me in when I was in danger of being lost in the wilderness. When I faced failure (of which there were many), or went down the deep rabbit holes, you were there to pull me back on my feet with words of encouragement and share great new ideas of how to proceed. The fact that there are any main chapters in this dissertation, let alone three chapters (on wildly different topics, no less), is a testament to your abilities as a PI. It has been the highest honor being your student, and I hope I can live up to the strong ideals, creativity, and positivity you have instilled on me during our time together.

George, you have been an absolute pleasure to work with. You were there in the beginning of my PhD journey, and gave me the space and encouragement to follow my research interests. Throughout the years, you have always been excited to hear about my work, even for research that sometimes fell slightly outside the domain of your own lab. You have made yourself available, given your time and energy, and have shared both considerable knowledge and resources from you and your students. And when I went radio-silent for long stretches of time, you were always there, waiting with patience to jump back in when the timing was right.

Kazlin, you have been an amazing collaborator. From the beginning when I started where Vi left off, you got me up to speed quickly and laid a strong foundation for developing the VP closure project to where it is today. You facilitated a system of teamwork with your students that made sure we could work together to get the right data as our project evolved, and when things went wrong or took longer than expected, you were always willing to impart advice and brainstorm the next steps. Your enthusiasm for helping others helps put in perspective how sometimes the most mundane part of research will eventually contribute something helpful to those beyond academia, and that was a big inspiration for a graduate student who sometimes needed that reminder.

Nic, thanks for agreeing to come aboard my committee with little more than a zoom chat as introduction. You have been incredibly helpful during committee events, and many your suggestions and comments have strengthened my research, and through that, this dissertation. I would also like to thank you the early advice you gave me, based on your own graduate experiences. I feel incredibly lucky that I was able to use your work and models as the major framework driving a chapter of this dissertation. I do apologize for butchering your beautiful biceps femoris model with my changes. I hope you'll forgive me.

Jason, you were amongst the earliest in my committee (starting back to my comprehensive exam), and have had the unenviable position of having to be caught up to speed very quickly at every one of my milestones. Despite this, you have been nothing but gracious and thoughtful, and at every meeting you have imparted excellent advice and driven discussions that have only strengthened my methodology and research process. I am thankful for your involvement throughout the course of my PhD, especially given your expertise and mastery of finite element topics, the common thread that entwines this entire dissertation.

To the members of the M3 lab, thank you. It is an odd sort of nostalgia that comes from being the last student left of the lab group I joined back in 2018. But getting to know the new members as time went has shown me that the lab I will soon be departing is in better hands than ever. To the two Katies, thanks for immediately making me feel welcome upon my first arrival, and getting me acclimated to the lab life. To Ben, while we did not overlap in-person much, I will always remember you for acting as my introduction to UVA as my tour guide on severely short notice.

Amanda, thank you for imparting your knowledge of VML, modeling and otherwise, and helping me bridge my experiences during my initial lab rotations. Hunter, we had some excellent discussions regarding movies and television. Adrienne, you exhibited a balanced a driven seriousness with an incredible sense of humor that kept the spirit of the lab strong. Vi, you are one of the kindest people I've ever met, and you were the social life of the lab, even getting me to emerge slightly from my introverted self.

Brian, thanks for troubleshooting my first experiences with FEBio; any skill I have with that software can probably be traced to your early intervention. Xiao, you've kicked my butt with good questions several times during my lab presentations - you definitely improved my work and helped improve my presentational skills.

To Ridhi, thanks for being a friend from the start. Your organizational skills are what I aspire to, although I know I will never reach your level. And for never being overly obnoxious when Bucknell beat Lehigh in basketball. Allie, thanks for being awesome, and

being up for a chat when I needed someone to bother for just to talk to for my own sake. Megan, thanks for being friendly to all, your passion and drive for research is inspiring. To Mario, I loved getting to chat about movies and general nerdy media. You were a fantastic lab mate, and even better neighbor in Ash Tree townhomes – thanks for taking some of my stuff when I moved!

Jacob, thanks for always being approachable and tremendously helpful on everything, no matter what it was or how trivial it might be. Emily, you were and continue to be an amazing asset to the lab and a wonderful personality. Finally, to Kimberly, Yasmina, and Amanda: I regret that we did not get many chances for interactions as I would have liked due to unfortunate timing, but I trust you will keep the spirit of the lab alive and doing amazing things with your time with Silvia and UVA.

As an additional thanks connected to UVA, I'd like to thank Dr. Minton Cooper of UVA orthopaedics (and his amazing team). Because of him, I will be able to defend this dissertation standing on my own two feet. I can also claim I'm part cyborg now, which is kind of cool.

As for personal acknowledgements, I would first like to thank my parents. At every stage in my life, you were there to support me and encourage me to find my passion. I would not have had the opportunities I had without your willingness to fight for me and my dreams. I am in awe of the sacrifices you made to get me to the path I am on today, and everything I have, and ever will ever accomplish will have been thanks to you. Dad, thanks for fostering my love of science and engineering through early and repeated exposure to high-quality science fiction. Mom, thank you for pushing me forwards when I needed a nudge, but being there to catch me when things went wrong.

Next, I would like to thank my brother Ted, a.k.a. the MOTIVATOR. You have been the best brother I could have ever asked for, and you have helped drag me out of some of the darkest points of my life when I was flailing. Go Blue Devils.

Finally, I would like to thank Tara. If there is anyone who can be called a co-expert on the subject of this dissertation, it's you. For 5+ long years, you have suffered my incessant description of every minute detail, every sputtering of jargon, and every lamentation of failure for the course of my PhD, and you did so willingly with unending patience, grinning the warmest smile on the planet. You have been there from start of our mutual beginnings at UVA, and I can affirmatively say that without you, I don't think I would have made it to this point. Spending time with you was what I looked forward to after long days of research, whether that be hitting the North Grounds gym, or going hiking along the Shenandoah mountains on the weekends. You lifted me up from despair at my lowest lows, and celebrated even my smallest victories. When things got tough for me, you were the person I leaned on. I loved going on adventures with you in Charlottesville and beyond, and am looking forward to continuing our journey together. Thank you for being part of this adventure.

This dissertation is for all of you.

**Applications of Finite Element Analysis to Model  
and Understand the Complexities of Muscle in  
Clinically Relevant Scenarios**

Matthew DiSalvo

2024

Copyright © Matthew DiSalvo 2024

## **Abstract**

Muscle is a complex tissue with a hierarchical structure that works together to perform optimized functions. Developing theoretical frameworks to understand the relationship between muscle structure and function is a targeted goal in biomechanics; however, the complexity of muscle tissue necessitates advanced modeling approaches. The finite element (FE) method has provided new opportunities to explore questions regarding the form and function of muscle with regards to clinical applications. In this dissertation, I developed and applied novel approaches for creating, simulating, and analyzing finite-element models of muscle to explore the implications of three relevant areas. First, I created a model of volumetric muscle loss in the rat tibialis anterior to understand the complex relationship between injury size/location/shape influences muscle force. Second, I constructed a constitutive model of muscle mechanics that implements the force-velocity behavior as an open-source plugin for free FE software, in order to investigate how the force-velocity behavior influences muscle tissue strain distributions. Third, I develop a new model of soft palate closure that incorporated, for the first time, how activation of the superior constrictor muscle influences velopharyngeal function. This model was validated with MRI participant data, successfully predicted the outcomes of MRI-measured phonation, and provided new hypotheses how muscle function relates to common closure patterns. Taken together, these advances in the FE modeling of muscle provided a broad range of insight into muscle behavior and pave the way for future developments and tools to be harnessed for clinical applications.

## Table of Contents

<b>Acknowledgements</b>	<b>i</b>
<b>Abstract</b>	<b>iv</b>
<b>Table of Contents</b>	<b>v</b>
<b>Table of Figures</b>	<b>vi</b>
<b>Table of Equations</b>	<b>vii</b>
<b>1. Introduction</b>	<b>2</b>
<b>2. Background</b>	<b>7</b>
2.1 What is Muscle?	8
2.2 Finite Element Analysis	11
2.3 Constitutive Model of Muscle	14
2.4 Clinical Issue 1: Volumetric Muscle Loss Diminishes Muscle Force	16
2.5 Clinical Issue 2: Strain Injuries in Biceps Femoris Long Head During Sprinting	18
2.6 Clinical Issue 3: Velopharyngeal Dysfunction	19
<b>3. Finite Element Models of Volumetric Muscle Loss Injuries of the Rat Tibialis Anterior Predicts Patterns of Force-Loss</b>	<b>22</b>
3.1 Abstract	23
3.2 Introduction	23
3.3 Methods	25
3.4 Results	30
3.5 Discussion	37
<b>4. Force-Velocity Behavior Impacts Strain Distribution in FE Muscle Models</b>	<b>40</b>
4.1 Abstract	41
4.2 Introduction	42
4.3 Methods	44
4.4 Results	51
4.5 Discussion	61
<b>5. A Measurement Based Finite Element Model of Velopharyngeal Closure Including Lateral Wall Activation</b>	<b>65</b>
5.1 Abstract	66
5.2 Introduction	66
5.3 Methods	69
5.4 Results	77
5.5 Discussion	82
<b>6. Conclusions</b>	<b>88</b>
6.1 Summary	89
6.2 Contributions	90
6.3 Future Directions	93
6.4 Final Thoughts	95
<b>7. Appendix</b>	<b>97</b>
<b>8. Citations</b>	<b>102</b>

## Table of Figures

### Figures

2.1 Sketch of muscle hierarchy	9
2.2 Muscle force-length properties	10
2.3 Muscle force-velocity curve	11
2.4 Discretization of a problem domain	12
2.5 VML from tibial fracture	17
2.6 Illustration of VML in a TA muscle	17
2.7 Illustration of rat TA force measurement	18
2.8 BFLH insertion and origin	18
2.9 Strain injury occurs at running swing phase	19
2.10 Normal velopharyngeal closure	20
2.11 Velopharyngeal dysfunction	21
3.1 Intact TA model	28
3.2 TA Smax sweep and injury comparison	30
3.3 VML model result bar graphs	33
3.4 Standard VML group results	33
3.5 6 mm punch group results	34
3.6 Thin 1 mm group results	34
3.7 Standard VML (Multicut) group results	35
3.8 Thin 1 mm (Multicut) group results	36
3.9 Volume, cross-sectional area, and aponeurosis intersect versus force-loss	36
4.1 Single element and cylindrical model setup	48
4.2 Tapering cross-section and BFLH model setup	49
4.3 Single element force-velocity curve	52
4.4 Cylindrical model force-velocity curve	52
4.5 Tapering cross-section fiber strain colormap	54
4.6 Tapering cross-section fiber strain distribution	55
4.7 Average fiber strain and velocity for BFLH models at running speeds	57
4.8 BFLH model fiber strain colormap	59
4.9 BFLH fiber strain distribution	60
5.1 Diagram of anatomical measurements	72
5.2 Shaded anatomy of interest from MRI	72
5.3 Velopharyngeal FE model setup	74
5.4 Measuring posterior closure	76
5.5 Average change in measurements at phonation	80
5.6 Classifying closure patterns and posterior closure	81
7.2 (Appendix) Tapering cross-section strain relaxation for Chapter 4	100
7.3 (Appendix) Rest and phonation measurement scatter plot for Chapter 5	101

### Tables

3.1 List of TA VML models	29
3.2 Constitutive model parameters for TA	30
4.1 FV Material properties	46
5.1 Recruited participant data	69

5.2 Descriptions of MRI measurements	71
5.3 Muscle material properties	73
5.4 Velum and raphe material properties	74
5.5 Average MRI measurements	78
5.6 Average Phonation Measurements	79
7.1 (Appendix) Model result table for Chapter 3	97
<b>Table of Equations</b>	
2.1 FE Matrix Form	12
2.2 – 2.7 Invariants	14
2.8 Uncoupled strain energy	15
2.9 Dilatational strain energy	15
2.10 Along-fiber shear	15
2.11 Cross-fiber shear	15
2.12 Strain energy due to along-fiber shear	15
2.13 Strain energy due to cross-fiber shear	15
2.14 Strain energy due to fiber stress	15
2.15 Total fiber stress	15
2.16 Total fiber force	15
2.17 Passive fiber force	15
2.18 Active fiber force	16
2.19 Deviatoric strain energy	16
4.1 Uncoupled strain energy	44
4.2 Dilatational strain energy	44
4.3 Fiber stretch	45
4.4 Fiber velocity	45
4.5 $F_{scale}$	45
4.6 Total fiber force	47
4.7 New strain energy due to fiber stress	47

## Chapter 1

### Introduction

*The good news about computers is that they do what you tell them to do. The bad news is they do what you tell them to do.*

*-Ted Nelson*

**Chapter 1: Introduction**

The coupling of computational models with muscle research has greatly assisted our understanding of muscle biomechanics. From Galen to Da Vinci, physicians and anatomists have nearly always relied on studies of human cadavers and extrapolation from animals to gain an understanding of our skeletal muscle system. It was not until the 20<sup>th</sup> century for what we might consider significant progress was made on understanding the deeper mechanisms of living muscle. In the last 100 years, there has been an explosive growth in medical technology, giving us new ways to observe muscle down to its finest details and measure its behavior both internally and externally. Experiment after experiment, science has given us a working model of muscle behavior, even to the level of interactions of the molecular building blocks in individual sarcomeres, the repeating contractile element that gives muscle its function. However, despite our marching advance, more questions continue to reveal themselves. Computational modeling provides us another method to tackle experimental questions that would range between incredibly intrusive to effectively impossible, especially when dealing with human anatomy. They allow us to test predictions about our understanding of muscle, and sometimes reveal exciting new behaviors that might never otherwise be detected. Computers also allow a level of experiment customization that practical methods would be hard-pressed to achieve, down to recreating and testing a person's own individual anatomy, or even inventing new configurations to test and compare.

A computer model's usefulness is also a reflection on the experimental question. When you build a model of something, you accept what you have is a shallow imitation of the real

thing. Biology is too complex and too dynamic to allow us to build a fully accurate recreation. However, if you tailor a model to the core of a question, there might just be enough of the true nature to get something useful out of it. This is also the case with finite element modeling. There is a long history of studying how muscle reacts when its poked, prodded, stretched, and squished, so we have some idea of how it should function as a material at different scales. With finite element modeling, we can take our well-tested assumptions about muscle material mechanics, and place them new configurations and apply them to new problems that could not be attempted before.

Each core chapter of this dissertation utilized the finite element method to accomplish a predictive analysis of muscle for a clinically relevant experimental question. Each one was built around a different question that each involves a different muscle, but all share a common thread of similar techniques and tools, and contributions to a better understanding of whole-muscle behavior in ways that can benefit human health. In Chapter 3, I explored the potential force-loss implications of large muscle injuries at different locations, based around real regenerative medicine experiments performed with rat muscles, in a muscle commonly afflicted by similar injuries in humans. In Chapter 4, I looked at the relationship of fiber strain changes due to the force-velocity effect and running speed in a muscle that is frequently injured in sprinters, and built a new tool that can benefit future experimenters in their own study of fiber strain. In Chapter 5, I built a model of speech-based velopharyngeal closure based on measurements from real people, in order to lay the groundwork for future predictive models useful for surgical planning for those with repaired cleft palate.

Chapter 3 details to the development of a finite element model of the rat tibialis anterior (TA) muscle, and a variety of volumetric muscle loss injuries tested using that model geometry to gain insight on how injury size and location can influence the muscle's ability to

generate force. There were two aims for this project. **1)** To develop a FE model of the rat TA that can accurately predict force generation from both healthy muscles, and a model that can also predict how much force is lost from surgically induced VML injury. **2)** Test a variety of injury volumes, locations, and shapes, and use the resulting model comparisons to infer the driving factors for force-loss. A TA geometry was built from rat MRI imaging, and scaled to match expected measurements from 12-week-old female Lewis rats (N = 8). Parameter sweeping of the chosen muscle material properties showed that the TA model could match the expected force of healthy isometric activation. A battery of 78 injury models were run, based on both literature-reported surgical injury patterns or speculative injury shapes. An injury pattern based on a common method was found to closely match the expected force-loss for another group of 12-week-old female Lewis rats (N = 4) who had undergone VML surgery, providing evidence that the modeling approach may be useful as a predictive measure. Additionally, the variety of injuries illustrated the significance of both cross-sectional area and the TA's distal aponeurosis over volume as drivers of force-loss in VML injuries. The manuscript for chapter 3 is currently titled "A Series of Finite Element Models of Volumetric Muscle Loss Injuries of the Rat Tibialis Anterior Predicts Patterns of Force-Loss", with co-authors George J. Christ and Silvia S. Blemker, and is in preparation for submission to a scientific journal.

Chapter 4 chronicles a newly developed constitutive model, based on a previously developed transversely isotropic, nearly incompressible, hyperelastic material, that represents muscle behavior and is implemented in the popular open-source FE software FEBio (Maas et al., 2012). Harnessing the plugin capabilities of FEBio, the project aimed to **1)** produce a force-velocity (FV) capable muscle material for use in quasi-static simulations. Additionally, the project also planned to use the new material to **2)** determine the impact of the FV relationship on muscle fiber strain in a variety of conditions, most notably the strain in muscle fibers of a biceps

femoris long head (BFLH) under sprinting conditions at a variety of speeds. To accomplish these two goals, I wrote a plugin for FEBio in C++ to implement the FV behavior in the existing muscle material. Extensive testing in single element and multiple element models (cylindrical and tapering cross-section models) showed the behavior of the new material was within expectations. Additionally, in the tapering cross-section and the BFLH FE models, the FV material had notable impact on fiber strain, tied to the maximum velocity parameter, and whether the muscle was undergoing lengthening or shortening. The work in Chapter 4 has been compiled into the paper “The need for speed – does the force-velocity property significantly alter strain distributions within skeletal muscle?”, with co-author Silvia S. Blemker. The paper is currently under review for publication by the Journal of Biomechanics.

Chapter 5 describes the work in developing a new model velopharyngeal closure, based around the actions of the levator veli palatini (LVP) and superior pharyngeal constrictor (SPC) muscles, bring the velum in contact with the posterior and lateral pharyngeal walls. The goals of this project were to **1)** build and validate a generalized model of velopharyngeal closure and validate the model’s predictive behavior using MRI data from 12 adult subjects (6 male, 6 female), and to **2)** use the validated model to make predictions about velopharyngeal closure patterns by looking at the required combinations of muscle activation that best optimize the anatomy for closure. The resulting anatomy was successful in matching the average measurements at rest, as well as the change of anatomical measurements from /s/ phonation. Additionally, the model was able to mirror the expected behavior of the velopharyngeal mechanism with regards to closure patterns, further supporting the potential implications as a clinical tool for those looking to modify the velopharyngeal sphincter, such as in cases of those with velopharyngeal dysfunction due to a repaired cleft palate. The manuscript for the chapter is currently in preparation for journal submission to the Journal of Speech, Language,

and Hearing Research, and is titled “A Measurement Based Finite Element Model of Velopharyngeal Closure Including Lateral Wall Activation”, co-authored by Silvia S. Blemker and Kazlin N. Mason.

In summation, the models developed in each of the listed provide contributions broadly to the field of computational biomechanics as well as specific clinical applications. New ways of building muscle finite element models were developed to tackle important questions in each of the topics, and may provide stepping-stones for additional developments in the future. A brief background primer on each clinical issue is available in section 2.4 through 2.6, and also in the introduction sections of Chapters 3, 4, and 5.

## Chapter 2

### Background

*There's something very important I forgot to tell you.*

*-Egon Spengler (Ghostbusters, 1984)*

## 2.1 What is Muscle?

Muscle is an answer to an essential evolutionary question: how do you generate movement (and do it fast enough to be advantageous)? With selective pressure increasing organism size and more complex body plans, there was significant advantage in solutions that scaled up from beyond those that evolved for individual cellular movements (flagella, cilia, etc.). There is evidence that a muscle precursor of organized simultaneous contraction may have evolved from epithelial cell cooperation (Nickel et al., 2011), but also evidence that important myosin motor proteins may predate multicellular organisms (Steinmetz et al., 2012), suggesting there may have been multiple convergent paths to muscle. Eventually, the rise of chordates, then later vertebrates, also coincided with the development of dedicated axial muscles (Sefton and Kardon, 2019), which became increasingly more specialized, varied, and numerous as evolution marched on. As a result, the skeletal muscle now powering motion in mammals is a tissue that is efficient, specialized, and highly effective at accomplishing its task.

Skeletal muscle, structurally, consists of repeating units of sarcomeres, a structural organization of interdigitated myosin and actin proteins, titin, and other proteins that allow for contraction and force-generation through ATP cross-bridge cycling (Mukund and Subramaniam, 2020). Arranged serially and in parallel, groups of sarcomeres make up myofibrils, which in turn make up muscle fibers. Groups of muscle fibers are further arranged into muscle fascicles, that span the body of a muscle to drive force from tendon to tendon. Controlling the contractibility of muscle are groups of neurons called motor units that interface with groups of muscle fibers, that initiate contraction through synaptic release of acetylcholine, spurring a depolarization chain reaction that propagates down a muscle fiber, eventually resulting in calcium ions binding to troponin and giving myosin space initiate cross-bridging with actin. By varying the number of

motor units activated, a muscle can be modulated to range from just contracting only a small percentage of its fibers to a full contraction to generate maximum force.

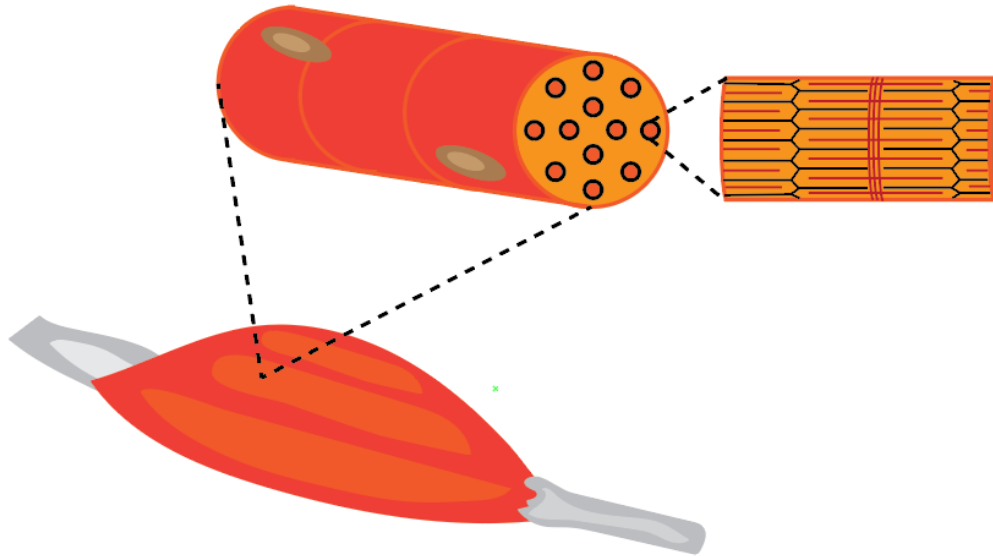


*Figure 2.1: Muscle is a hierarchical tissue, made up of muscle fibers, which are in turn made up of sarcomeres, the contractile unit of muscle.*

The structural arrangement of muscle gives rise to several properties that have critical implications for its biomechanical behavior. The first property is a force-length behavior (Fig. 2.2). As muscle fibers shorten, the ability to produce force diminishes as actin strands overlap each other, limiting the number of free sites available for myosin cross-bridges. While lengthening, the actin can get pulled past myosin, also preventing cross-bridges. In the center of these extremes, is an optimal length in which overlap of the actin and myosin is maximized, allowing for the most amount of potential cross-bridges. However, lengthening also causes resistance from sarcomere elements such as titin, which can contribute more and more force as sarcomeres are stretched.

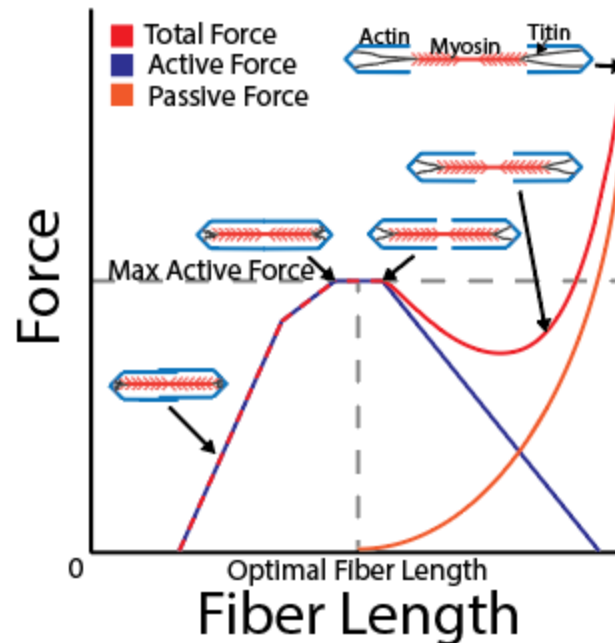
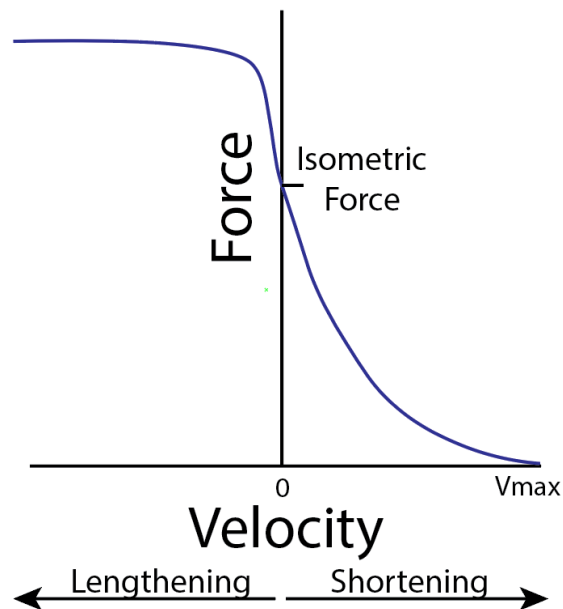


Figure 2.2: Diagram of force-length properties, with an illustration of sarcomere alignment at each different length.

The second property is force-velocity behavior (Fig 2.3), in which shortening velocities result in force-loss, while lengthening velocities result in additional force compared to isometric conditions. The common interpretation of the force-loss behavior is that when fibers shorten too quickly, cross-bridges are either lost or unable to form in the first place, as actin slides past myosin heads at the rate of attachment (Huxley, 1957). Lengthening, however, increase sarcomere force independent of muscle length. While less is known about the exact molecular mechanisms of lengthening force-velocity, there are thoughts that structural changes in passive-resistance elements such as titin in the presence of calcium which can contribute to viscoelastic effects that both enhance force-production and may contribute to residual force-enhancement (Hessel et al., 2017). Other theories involve the exposure of extra binding sites on myosin heads as it is pulled with actin (Rassier, 2008). It remains an area of active investigation and discussion among muscle physiologists (Alcazar et al., 2019). The end result is a double-hyperbolic behavior that gives muscle an extra layer of dynamic response.



*Figure 2.3: The force-velocity curve for muscle.*

Muscles take advantage of these properties to optimize based on their required task. Due to sarcomere in-series arrangement and co-current activation, longer muscle fibers can contract more quickly and can generate greater length change than shorter fibers. Smaller fibers can generate more force with less length change than longer fibers, but tend to be slower to contract due to less sarcomeres in series (Kruse et al., 2021). Even greater modulation comes from the different types of muscle fibers, optimizing for combinations of speed, strength, and stamina through glycolytic or oxidative methods of ATP cycling (Schiaffino and Reggiani, 2011). Strategic arrangement of muscle shapes, fibers pennation angles, and tendons all further influence muscle function (Lieber and Ward, 2011).

## **2.2 Finite Element Analysis**

Finite element (FE) analysis (Hughes, 2000) is a technique which involves the discretization of a domain into smaller subdomains called elements, made up of a series of nodes. For partial differential equations (PDE), with known solutions at designated boundaries, there may exist

solutions of the PDE throughout a domain space. Given the complexity of geometry of many problem spaces, direct integration of PDEs, particularly high-level ones, becomes increasingly difficult. Instead, the solution through the problem space may tackled through transforming the problem into a series of numerical approximations. This is done discretizing the problem space into elements, which are small areas of volume defined by a series of nodes (the number of which can vary depending on desired element shape and control of intra-element interpolation) (Fig 2.4). A series of linear equations are then set up in matrix form (eq. 1.1), in which can then solve for a vector of unknown states at the location of each node (which in the case of mechanics, this is relating the displacement ( $u$ ) of the nodes to the force ( $f$ ) experienced on the nodes through the inversion of a stiffness matrix ( $K$ )).

$$[K]\{u\} = \{f\} \quad (2.1)$$

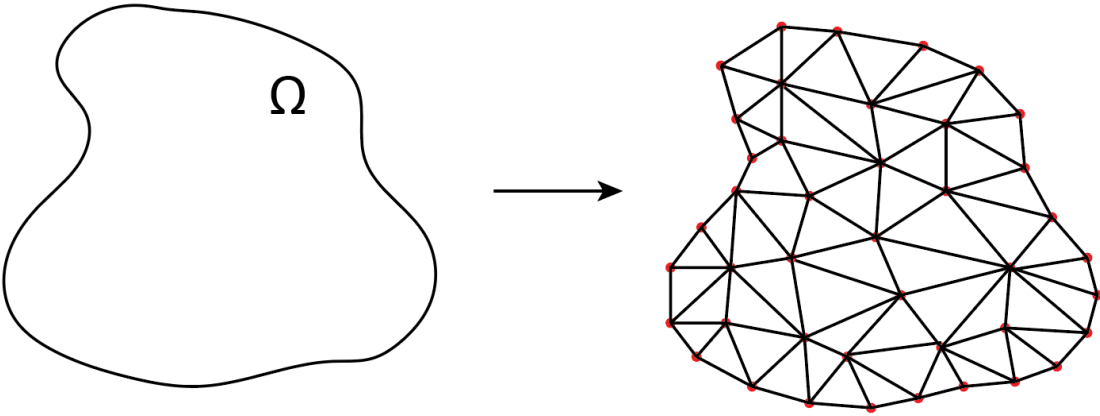


Figure 2.4: The transformation of a problem domain  $\Omega$  to a series of smaller domains, consisting of nodes and elements.

While useable by hand calculation, usually for small problems with few nodes, this can get extremely unwieldy very quickly. Where the FE method really shines is through the use computers. Computers can iterate and solve a mind-boggling number of equations, and do it inconceivably faster than humans can. The trick is balancing the detail of an FE model with the

desired accuracy of an answer. A tolerance level can be set on a residual (an expected answer to the PDE in question) in order to allow for close numerical approximation of the answer. However, the required computational time typically increases as tolerances become tighter. Additionally, more nodes, and better interpolation through using higher-order basis functions will better converge on the true analytical solution, but also add to computational cost. Often, many FE experiments will run convergence studies, which track FE model fidelity versus the solution – as the answer gets more accurate, there should be less and less change in the calculated output, providing a gauge for a stopping point against adding more elements into a model.

FE modeling particularly used in the field of mechanics. Providing a definition (called a constitutive model) of a material's directional responses to stress and strain (and potentially other factors for more complex definitions) independent of that material's aggregate size and shape belongs to the field of continuum mechanics. With a constitutive model, a problem of mechanical response states can be defined through referencing geometry and boundary conditions and solving analytically. However, problems are rarely simple enough to easily use analytical approaches, and thus are prime candidates for use of FE modeling. In FE modeling, the constitutive model defines the intra-element equations interpolated within elements, such that a simulation can predict the localized mechanical responses to boundary conditions set on the elsewhere in the problem space. In mechanical and civil engineering, this is an extremely powerful tool in helping test designs against potential failure states, without needing to physically test an example (which could get prohibitively expensive, especially for civil engineers). For biomechanics, the same advantages of FE modeling exist, especially when dealing with mechanical responses of tissues or anatomy that are either difficult to measure on

a practical standpoint, or impossible on an ethical one. A huge challenge, however, is using a constitutive model to represent enough detail about a tissue to provide accurate results.

### 2.3 Constitutive Model of Muscle

Muscle behavior is defined by the path of muscle fibers and their relative internal arrangements. Therefore, effective approaches to FE modeling of muscle has to overcome the challenge providing a workable constitutive model that accounts for essential properties such as force-length and fiber directionality. One solution defines muscle as a transversely-isotropic, nearly incompressible, hyperelastic material (Blemker et al., 2005). The material uses the classic three invariants and two additional invariants based on the definition of fiber direction (Eq. 2.2 through Eq. 2.7), where  $F$  is the deformation gradient,  $A$  is a vector field defining the material's fiber's starting orientation,  $a$  is the current fiber vector as a unit vector,  $C$  is the right Cauchy-Green deformation tensor,  $J$  is the Jacobian, and  $\lambda$  is fiber length.

$$\lambda a = F \cdot A \quad (2.2)$$

$$\bar{I}_1 = \text{tr}C \quad (2.3)$$

$$\bar{I}_2 = \frac{((\text{tr}C)^2 - \text{tr}C^2)}{2} \quad (2.4)$$

$$\bar{I}_3 = \det C = J^2 \quad (2.5)$$

$$\bar{I}_4 = \lambda^2 = A \cdot C \cdot A \quad (2.6)$$

$$\bar{I}_5 = A \cdot C^2 \cdot A \quad (2.7)$$

The material also accounts for incompressibility by separating the dilatational and deviatoric strain energy (Eq. 2.8). The dilatational term can further be defined as a function of the strain energy of along-fiber (Eq. 2.12) and cross-fiber (Eq. 2.13) shear, where  $G_1$  and  $G_2$  represent the along-fiber and cross-fiber shear moduli.

$$\Psi = \Psi_{iso} + \Psi_{vol} \quad (2.8)$$

$$\Psi_{iso}(\bar{I}_1, \bar{I}_4, \bar{I}_5, \alpha) = W_1(B_1(\bar{I}_4, \bar{I}_5)) + W_2(B_2(\bar{I}_1, \bar{I}_4, \bar{I}_5)) + W_3(\lambda(\bar{I}_4), \alpha) \quad (2.9)$$

$$B_1 = \sqrt{\frac{\bar{I}_5}{\bar{I}_4} - 1} \quad (2.10)$$

$$B_2 = \cosh^{-1}\left(\frac{\bar{I}_1\bar{I}_4 - \bar{I}_5}{2\sqrt{\bar{I}_4}}\right) \quad (2.11)$$

$$W_1 = G_1(B_1)^2 \quad (2.12)$$

$$W_2 = G_2(B_2)^2 \quad (2.13)$$

The strain energy as a result of the active and passive properties of muscle fibers ( $W_3$ ) is related through equations 2.14 through 2.18, where  $\sigma_{max}$  is the maximum isometric stress,  $\lambda_{ofl}$  is optimal fiber length,  $\alpha$  is muscle activation (0 to 1, with 0 representing zero fiber activation and 1 representing total fiber recruitment),  $P_1$  through  $P_4$  are scalars, and  $\lambda^*$  is the length at the start of linear fiber force from passive stretching.

$$\lambda \frac{\partial W_3^{muscle}}{\partial \lambda} = \sigma_{total}^{fiber}(\lambda, \alpha) \quad (2.14)$$

$$\sigma_{total}^{fiber}(\lambda, \alpha) = \frac{\sigma_{max} f_{total}^{fiber}(\lambda, \alpha) \lambda}{\lambda_{ofl}} \quad (2.15)$$

$$f_{total}^{fiber} = f_{passive}^{fiber} + \alpha f_{active}^{fiber} \quad (2.16)$$

$$f_{passive}^{fiber} = \begin{cases} 0, & \lambda \leq \lambda_{ofl} \\ P_1 \left( e^{P_2 \left( \frac{\lambda}{\lambda_{ofl}} - 1 \right)} - 1 \right), & \lambda_{ofl} < \lambda < \lambda^* \\ \frac{P_3 \lambda}{\lambda_{ofl}} + P_4, & \lambda \geq \lambda^* \end{cases} \quad (2.17)$$

$$f_{active}^{fiber} = \begin{cases} 9\left(\frac{\lambda}{\lambda_{ofl}} - 0.4\right)^2, & \lambda \leq 0.6\lambda_{ofl} \\ 9\left(\frac{\lambda}{\lambda_{ofl}} - 1.6\right)^2, & \lambda \geq 1.4\lambda_{ofl} \\ 1 - 4\left(1 - \frac{\lambda}{\lambda_{ofl}}\right)^2, & 0.6\lambda_{ofl} < \lambda < 1.4\lambda_{ofl} \end{cases} \quad (2.18)$$

Finally, the deviatoric strain energy is defined as the bulk modulus ( $K$ ) times one-half of the square of the natural log of the Jacobian (Eq. 2.19).

$$\Psi_{vol} = \frac{K}{2} \ln(J)^2 \quad (2.19)$$

With this constitutive model, FE models can be made that scales from individual fascicles all the way up to whole muscle. This constitutive model is used in the research detailed in Chapters 3, 4 and 5, referred frequently as ‘muscle material’, as that name is used by the software FEBio in its material list option. Notably, this constitutive material captures force-length properties, it does not allow for force-velocity behavior, the implementation of which is the subject of Chapter 4.

#### 2.4 Clinical Issue 1: Volumetric Muscle Loss Diminishes Muscle Force

Volumetric muscle loss (VML) has been defined as “...the traumatic or surgical loss of skeletal muscle with resultant functional impairment.” (Grogan et al., 2011). In humans, this is often the result of extreme injuries that can originate from events such as high-energy bone fractures (Fig 2.5) or combat trauma (Testa et al., 2021), either directly from the event or during surgical intervention (such as muscle debridement to prevent necrosis, etc.). It can permanently decrease a quality of life as muscle is unable to regenerate the damaged areas enough to regain the muscle’s former mobility and force production (Corona et al., 2015). There is significant investment in resources in biomedical research to overcome these challenges, specifically in the development of implantable biomaterials to support and induce new muscle growth (Greising et al., 2019; Langridge et al., 2021)



Figure 2.5: A-E: Healing after a high-energy tibial fracture. F: Damage to muscles results in significant decrease in leg muscle functionality, particularly the dorsiflexors (a group that includes the TA). Figure is reprinted from literature source (Garg et al., 2015).

A commonly used animal model to test potential therapeutics is the rat tibialis anterior (TA). It has several advantages over other muscles, including that it is commonly injured in humans, its force can be measured *in-vivo* through dorsiflexion experiments (Mintz et al., 2016), and it is near the anterior surface of the rat leg, providing easier access than many other muscles. In a typical experiment, a section of the rat TA will be removed (Fig 2.6) near the muscle mid-belly (Wu et al., 2012), and either left open as an injured control, or the injury will be filled with the experimental therapeutic. Repeated dorsiflexion measurements can then be used to calculate the change in the maximum force at tetanus to determine the efficacy of the experimental treatment (Fig 2.7).

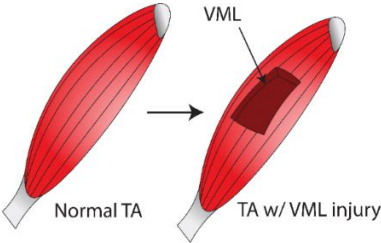


Figure 2.6: Illustration of a VML injury surgically created in a rat TA.

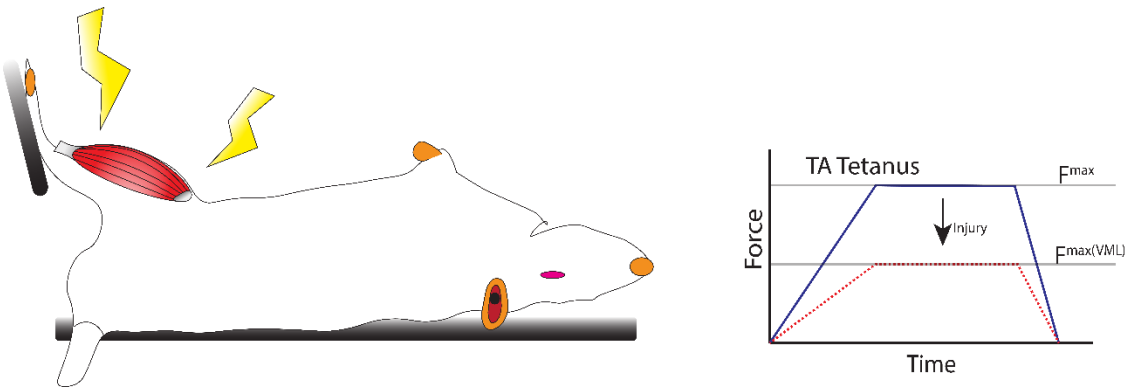


Figure 2.7: Diagram of a rat dorsiflexion experiment with the TA. The rat's leg is secured at 90 degrees to a servomotor, that measures the result torque generated from electrical stimulation in the TA. Force is measured at the frequency required for tetanus, and is used for comparative purposes.

**2.5 Clinical Issue 2: Strain Injuries in Bicep Femoris Long Head During Sprinting**

The biceps femoris long head (BFLH) is a hamstring muscle (Fig 2.8) that is frequently injured in agility athletes (Proske et al., 2004). During running, the BFLH undergoes significant eccentric contraction at the later stage of the running gait cycle during the transition from knee flexion to extension (Fig 2.9). Additionally, the BFLH is very likely to be reinjured in those same group of athletes (Ekstrand et al., 2012).

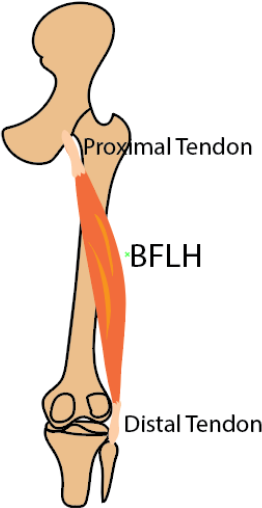
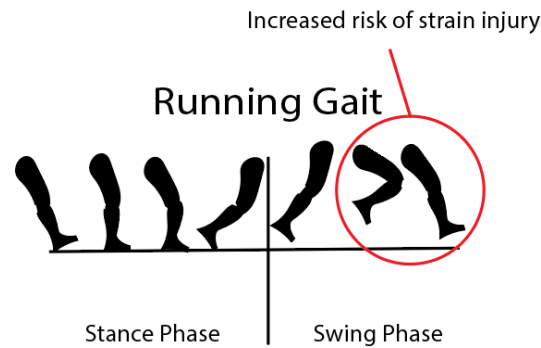


Figure 2.8: the BFLH spans from the ischial tuberosity and inserts into the fibula head.



*Figure 1.9: During the swing phase, the extension of the knee stretches the BFLH while it is undergoing activation.*

Previous FE studies of the BFLH have shown that large amounts of fiber strain accumulate near the thinner proximal aponeurosis, especially at high sprinting speeds (Fiorentino et al., 2014; Fiorentino and Blemker, 2014), which has been marked as a potential risk area for injury based on individual variability (Evangelidis et al., 2015). There is significant interest in understanding the patterns of strain within the BFLH in order to develop injury-prevention strategies and treatments (Heiderscheit et al., 2010)

### **2.6 Clinical Issue 3: Velopharyngeal Dysfunction**

Human speech relies on an system to muscles to control the amount of air exiting the mouth and nasal cavity (Perry, 2011). A large number of muscles facilitate this process, but much of the primary action of velopharyngeal closure (Fig. 2.10) comes from the contraction of the levator veli palatini (LVP) muscle, which drives the soft palate (also known as the velum) into the posterior wall, preventing the movement of air. Additionally, there muscles that surround the velopharyngeal space, such as the superior pharyngeal constrictor, which help lateral closure of the space. The combination of activation among the velopharyngeal muscles dictates the closure patterns, with the majority of the population having a LVP-primary coronal closure pattern (Jordan et al., 2017; Shadi et al., 2022). However, when a person is unable to achieve effective closure, the result is nasally speech (Young and Spinner, 2024). Velopharyngeal

dysfunction is the inability to close air from the nasal cavity during speech (Woo, 2012), either through issues with anatomy (Fig 2.11) or neuromuscular control. A large percentage of those with velopharyngeal dysfunction come from those with repair cleft palates (Hopper et al., 2014), who will often need corrective surgery later in childhood. Several surgical methods exist to modify the anatomy to help achieve closure, including flap transfers and wall augmentations (Nam, 2018). Predicting the outcomes of these surgeries, particularly on a subject-specific basis, is a sought-after goal in the surgical community. Finite element models have been developed to accomplish this on some basis (Inouye et al., 2015; Tran et al., 2022), but so far have not captured the true three-dimensionality by including lateral wall boundaries or their muscles. A better understanding of how to incorporate the lateral wall into model simulations may be an effective step in better predictive models.

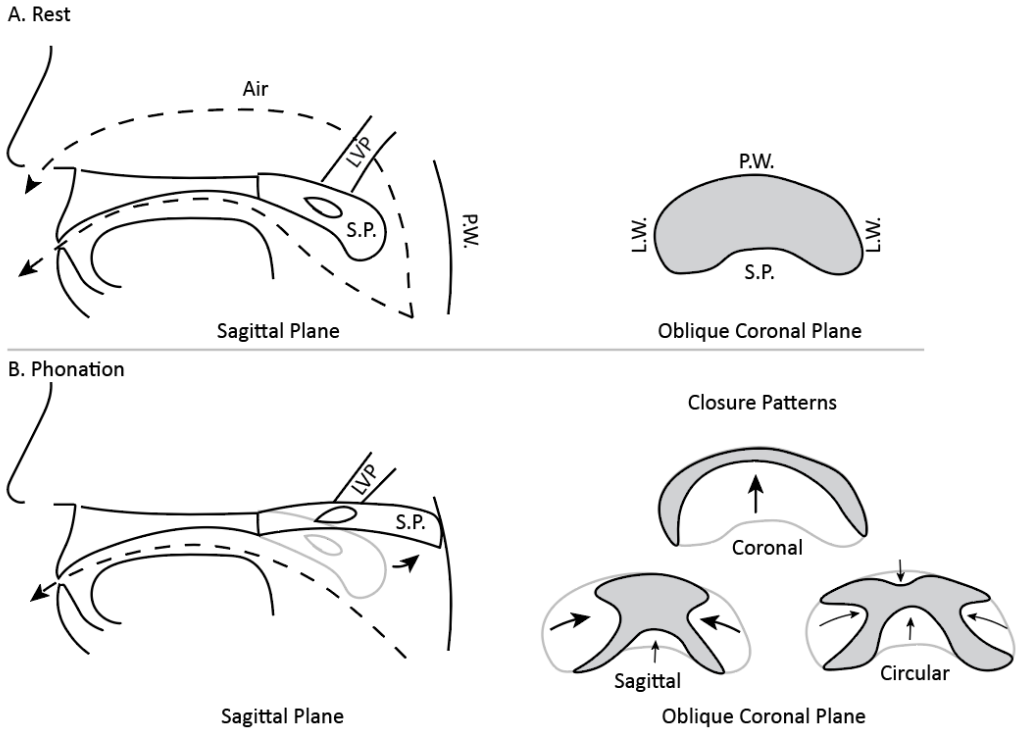


Figure 2.10: Velopharyngeal closure in the sagittal and oblique coronal planes. LVP – levator veli palatini. S.P. – soft palate. P.W. – posterior wall. L.W. – lateral wall. A. at rest, the LVP and LW (consisting of a series of muscle, including the superior pharyngeal constrictor) are inactive, providing a gap between the nasal cavity and the throat that allows air to flow freely. B. During phonation, the LVP and the L.W. muscles activate, closing the pharyngeal port. This is accomplished primarily in three different way. The first is the coronal closure pattern, in which the LVP does

the majority of closure by driving the S.P. both posterior and superior into the posterior wall. The second is a sagittal pattern, in which the L.W. muscles drive most of the closure by driving the sides of the velopharyngeal port inwards. The third main closure pattern is the circular pattern, in which both the wall muscles and the LVP muscle work together.

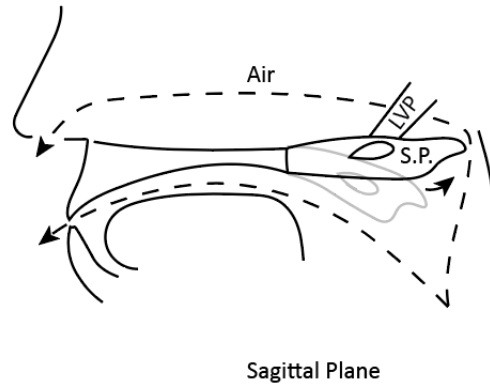


Figure 2.11: Velopharyngeal dysfunction is caused when air is able to move past the pharyngeal port during phonation. This can be due to a insufficiently sized or injured soft palate (as is often the case for those with repaired cleft palate), or a failure of the appropriate muscles to sufficiently activate.

### Chapter 3

#### **Finite Element Models of Volumetric Muscle Loss Injuries of the Rat Tibialis Anterior Predicts**

#### **Patterns of Force-Loss**

Acknowledgements: Silvia S. Blemker, George J. Christ

*'Tis but a scratch!*

- *The Black Knight (Monty Python and the Holy Grail, 1975)*

### 3.1 Abstract

Volumetric muscle loss can result in permanent muscle impairment, and is a topic of active investigation to better understand ways to use muscle regeneration to improve clinical outcomes. Understanding the form and function of how VML injuries lead to force-loss is an important step in designing potential treatments. The rat tibialis anterior (TA) muscle is commonly used by VML researchers as a model for force-loss and to gauge the efficacy of potential treatments. However, the unique pennation structure due to an internal distal aponeurosis makes force-loss predictions difficult; a better understanding of how VML interacts with the geometry of the TA muscle may give clues to build more effective treatments. In order to gain a better understanding of VML in muscle, we designed a finite element (FE) model of a rat tibialis anterior, and validated the model with force-data taken from 12-week-old female Lewis rats. We subjected the model to 78 unique injuries among 5 injury styles, varying injury volume, shapes, and proximal-distal location, and found the amount of force-loss for each. We then used our model to compare with the force-loss of rats with a similar VML injury type. We found that the maximum cross-sectional area ( $R^2 = 0.523$ ) of an injury was a better predictor for force-loss than volume ( $R^2 = 0.277$ ), and that an injury's overlap with the distal aponeurosis was correlated with a force-preserving effect ( $R^2 = 0.507$ ).

### 3.2 Introduction

*Muscle*

Skeletal muscle has the ability to effectively regenerate after injury, following a process of cellular reorganization, remodeling, and regrowth in damaged areas (Bodine-Fowler, 1994; Karalaki et al., 2009; Tidball, 2011). However, a significantly large and violent muscle injury can overwhelm the muscle's ability to self-repair, causing volumetric muscle loss (VML) (Greising et al., 2018). VML injuries can result in permanent decreases in muscle that can severely impact quality of life (Corona et al., 2015; Testa et al., 2021).

A large portion of VML injuries occur in the lower extremity, causing persistent debilitation in locomotion and everyday tasks (Corona et al., 2015). High energy trauma, such as from complex bone fractures from automobile accidents, or combat wounds from military service, can directly or indirectly lead to VML. Tackling these challenges requires development of new generations of therapeutics designed to assist muscle with natural regenerative abilities (Langridge et al., 2021).

Rats are a commonly used model to study VML. The ease of isolation of the hindlimb muscles, which are common sites of VML in humans, is beneficial for in-vivo functional testing to test force-deficit and recovery following potential therapies. The tibialis anterior (TA) muscle of rats is a commonly utilized muscle, as it is anterior facing and easily accessed through surgical means without requiring removal of the muscle (Mintz et al., 2016; Wu et al., 2012), allowing for *in-vivo* testing via measurement of dorsiflexion against an apparatus.

Additionally, the effective action of the muscle is ankle dorsiflexion, which can be isolated to mostly the TA through the severing of the extensor digitorum longus (EDL). However, within the tissue engineering field, there are a variety of different techniques for VML injury, including rectangular sectioning via scalpel (Wu et al., 2012), as well as biopsy punches (Dolan et al., 2022a). These can lead to variability in injury location, volume, and cross-sectional area

disruption. A better understanding of how injury geometry can influence VML functional measurement, especially in a geometrically complex muscle such as the TA, may be useful in helping design and plan future regenerative experiments.

The finite element method is a potentially useful tool in uncovering the hidden intricacies of muscle mechanical behaviors that may not be feasible to physically measure in a real experiment (Dao and Tho, 2018a). Advances in muscle modeling methods have allowed for complex 3D geometric modeling, including realistic fiber mapping within elements to simulate fibers spanning from aponeurosis to aponeurosis (Handsfield et al., 2017), and has even been previously used to study locational effects of a VML injury in the rat latissimus dorsi (Passipieri et al., 2019; Westman et al., 2019). Therefore, we believe FE modeling may provide an excellent avenue to explore a variety of VML injuries in the rat TA. In this study, we aim to use finite element modeling to build a better understanding of the driving factors behind force-loss in the rat TA with volumetric muscle loss.

### **3.3 Methods**

#### *3D Modeling*

A Lewis rat was imaged with a Siemens/Bruker ClinScan 7T MRI (T1-weighted) to capture the distal left hindlimb in accordance with animal safety protocols. The DICOM stack was imported into the visualization software Slicer (Fedorov et al., 2012), where the TA muscle-tendon anatomy was identified and segmented. The segments were interpolated to form volumes, which were exported as a stereolithography (STL) file, and imported into MATLAB (MathWorks, USA). STL nodes on the surface of the muscle volume and distal aponeurosis/tendon volume were isolated using a MATLAB script, and then further exported into the 3D modeling software Inventor (Autodesk, USA). The coordinates of the imported nodes were used to reconstruct the

TA and tendon geometry, using the loft function between cross-sections comprised of the imported nodes.

The resulting CAD assembly included a proximal tendon cap, a full TA muscle body, and a distal internal aponeurosis that proceeds distally to become a portion of the distal tendon. The final muscle body had a volume of 418.9 mm<sup>3</sup>, scaled based on muscle volume data (Koning et al., 1987), with a muscle length of 30 mm.

Finite element meshing of the assembly was performed in Cubit (Coreform, USA), which generated an imprinted tetrahedral mesh for each component. Additionally, VML injury boundaries were generated by Boolean intersections of 3D templates of injury shapes with the completed muscle assembly. 10 meshes were made: 9 with different injury sizes and locations and to ensure smooth geometries around the shape of the injuries, and 1 without any incorporated injury in the mesh to test for optimized material parameters. The 10 meshes averaged  $502877 \pm 209998$  tetrahedral elements.

#### *FE Setup*

The CAD model (Fig. 2i) was imported into the finite element software FEBio (Maas et al., 2012), where an isometric boundary condition was applied by enforcing 0 displacement on the furthest surfaces on the proximal and distal tendons, holding the muscle-tendon unit length fixed during simulations. The muscle component of the assembly was assigned a combination of a hyperelastic Mooney-Rivlin material with a transversely isotropic, nearly incompressible, hyperelastic material (Blemker et al., 2005) with parameters similar to a FE model of the human biceps femoris long head (Fiorentino et al., 2014). The tendon material was assigned as a neo-Hookean material with a Young's modulus within range of previous measures of rat achilles tendon (Lambertz et al., 2000; Leahy et al., 2022; Vafek et al., 2018). Computational fluid

dynamics (Handsfield et al., 2017) using the proximal and distal aponeurosis sites as an inlet/outlet pair generated a fiber map for the muscle material, generating an estimated pennation angle of 12 degrees, measured in ImageJ (Schneider et al., 2012) against the plane of the internal aponeurosis against the directions of the generated fibers about midway through the muscle belly, within range of previously reported values (Eng et al., 2008). A quasi-static simulation was performed by activating the muscle material from 0 to 1 over a simulation time of 1 second, representing full fiber recruitment and contraction. The surfaces of the proximal and distal tendon were fixed with boundary conditions to prevent displacement or rotation, allowing for isometric behavior. The muscle's force was measured as the reaction force at the distal tendon at the final time step at  $t = 1$  second.

Torque data from control rats (N=8, 12 week old Lewis rats, Female, BW  $182.36 \pm 6.98$  g) from a cohort used in a previous study (Dienes et al., 2019) was used to determine the expected distal tendon force through conversion of moment arms of a 40 mm rat foot attachment of the servomotor and an expected 3.4 mm moment arm during dorsiflexion of the TA's insertion site across the ankle (Johnson et al., 2008). The result was a force of  $5.71 \pm 0.49$  N. The  $S_{\max}$  (also called  $\sigma_{\max}$ ) of the muscle material was swept with an intact model (no VML boundaries present in the mesh) from 0.28 to .5 MPa to match the resulting model force with the previous data (Fig. 3.2A). All VML model meshes produced a force within 5% of that value. For VML models, a full TA with the boundary of each injury in their mesh was run to give a baseline force for injury comparison, in order to account for any differences of mesh schema and fiber generation that arise with slightly different meshes. For VML injury models, the elements within the injury boundary were removed from the model, and the resulting force decrease was calculated and recorded (Fig. 3.3).

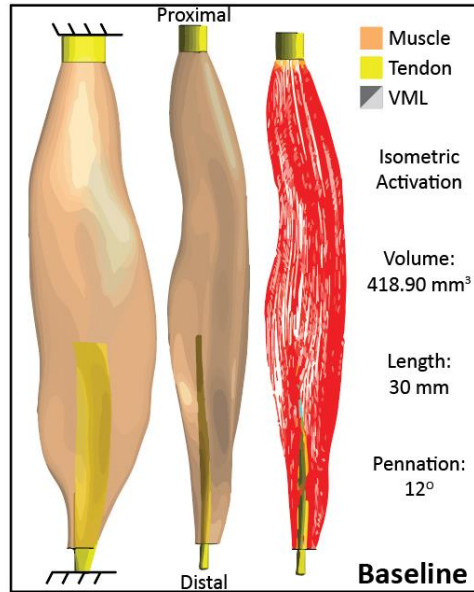


Figure 3.1: An anterior and lateral look at the TA model. The model has a proximal and distal tendon cap, as well as an internal aponeurosis at the distal end. Fibers span from the proximal tendon to the plane of the distal aponeurosis.

### VML Injury Setup

5 groups of injury were devised (Table 3.1), constituting 78 unique injuries from 9 different meshes. The first were a group of 5 injuries positioned on the anterior muscle face spanning between the proximal and distal aponeuroses, generated from a 10 mm long (proximal-distal) x 5 mm wide (medial-lateral) template, referred to as a standard VML injury (Fig. 3.4i). A designated injury (D1) was selected for comparison with a group of 4 12-week-old Lewis Rats (BW:  $181.03 \pm 13.6$  g,  $5.24 \pm 0.12$  N intact force) due to the 3 mm depth, central location, a “scoop”-like cross-section, and no overlap with the internal distal tendon, reflecting a likely surgically induced VML of this class. and no overlap with the internal distal tendon. The second group consisted of 6 mm diameter cylindrical cuts positioned proximally, distally, or centered, with the centered cut consisting of two injuries to make a partial depth injury, or a full depth injury, in order to replicate 6 mm biopsy punches (Fig. 3.5i). The third group consisted of three

thin 1 mm (proximal-distal) cuts, arranged proximally, distally, or in the center, one centered 10 (proximal-distal) x 1 (medial-lateral) mm cut (Fig. 3.6i). The fourth group was a collection of eight individual sections that together span the anterior surface of the TA, with a width of about 5 mm (medial-lateral) (Fig. 3.7i). Finally, the last group was a group of 7 sections of 1 mm (proximal-distal) that spanned the depth of the TA at the center (Fig. 3.8i). To initialize the simulations, the relevant injury areas were removed from the model mesh by commenting out the associated FE elements from the baseline model. The simulation conditions were identical to the baseline simulation setup. The reaction force at the end of the distal tendon was measured to compare force-loss. Cross-sectional area (CSA) loss was determined by measuring the muscle CSA normal to the ACSA plane (proximal-distal), and finding the greatest ratio of injury CSA to total CSA along the entire length of the injury.

*Table 3.1: List of models. Each mesh is labeled with a letter, injury group, number of injuries present in the mesh, a brief description of the injury.*

<b>Model Mesh</b>	<b>Model Group</b>	<b># of Injuries in Mesh</b>	<b>Injury Description</b>
<b>A</b>	Standard VML	1	~ 10 x 5 mm, center
<b>B</b>	Standard VML	2	~ 10 x 5 mm, proximal or distal
<b>C</b>	Standard VML	1	~ 10 x 5 mm, rounded
<b>D</b>	Standard VML	1	~ 10 x 5 mm, rounded, deeper
<b>E</b>	6 mm Biopsy Punch	5	6 mm diameter, center, proximal, or distal
<b>F</b>	Thin 1 mm	3	1 mm thickness, center, proximal, or distal
<b>G</b>	Thin 1 mm	1	~ 10 x 1 mm, center
<b>H</b>	Standard VML (Multicut)	8 (36 combinations)	~ 5 mm wide, variable length
<b>I</b>	Thin 1 mm (Multicut)	7 (28 combinations)	1 mm thickness, variable depth

3.4 Results

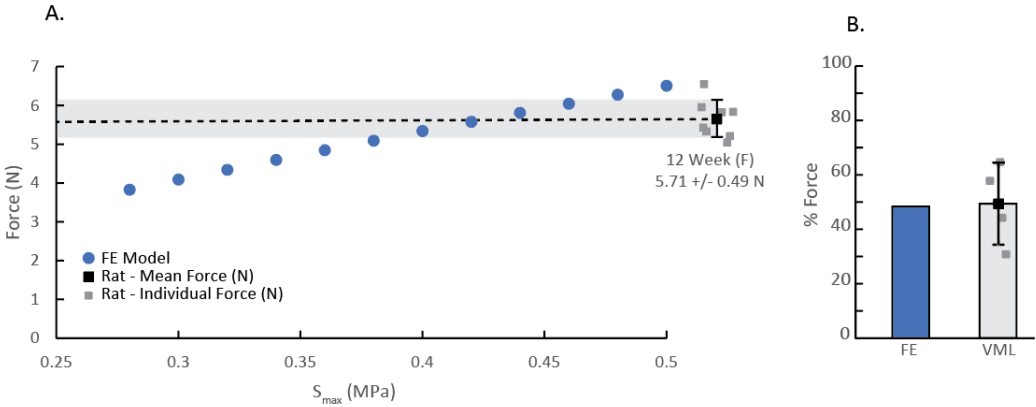


Figure 3.2: A. Several iterations of an intact model were run, varying the  $S_{max}$  parameter. Based on the results, a value of 0.42 MPa was chosen. B. The standard VML model D, which was designed to have the closest dimensions to the VML injury by having a 10x5x3 mm depth, produced a similar amount of force as the 12-week-old VML rats (compared to their control intact muscles).

Table 3.2: Muscle and tendon parameters selected for the TA muscle.

Muscle Tissue		
Muscle Material		
$S_{max}$	0.42	MPa
P1	0.04	*
P2	6.6	*
$\lambda_{off}$	1	*
$\lambda_{max}$	1.4	*
G1	$3.87 \times 10^{-4}$	MPa
G2	$22.4 \times 10^{-4}$	MPa
K	500	MPa
Mooney-Rivlin		
C1	0.1	MPa
C2	0	MPa
K	50	MPa

<i>Tendon Tissue</i>		
<i>neo-Hookean</i>		
E	450	MPa
v	-.4	*

\* Unitless  
Parameter

*Model Validation*

The sweep of the Smax parameters produced models with forces near to the  $5.71 \pm 0.49$  N of the 12-week-old rats with intact muscles (Fig 3.2A). The value of 0.42 MPa generated a model with 5.58 N. The model (D1) with the VML injury dimensions of 10x5x3 mm with no aponeurosis overlap, (3 mm being an expected depth for that style type of injury) produced a similar amount of force as the group of 4 12-week-old female Lewis rats (4 weeks after surgery, with the comparative intact force scaled to the increase of bodyweight of  $17.78 \pm 5.65$  %) (Fig 3.2B) with that injury type.

*VML Models*

The models varied in the percentage of force, volume, and cross-sectional area compared to their respective intact models (Fig. 3.3). The standard VML models produced a large amount of variability in their force loss, despite four out of five having similar volume loss of about 20% (Fig. 3.4). The proximally positioned B1 produced the most force loss compared to the other standard VML injuries near 20% volume loss, but the D1 model with greater volume and cross-sectional area disruption than the other models in that group produced the greatest force-loss.

In the 6 mm biopsy punch group (Fig. 3.5), the E4 model (full depth injury) produced the most force-loss. In the thin 1 mm group (Fig. 3.6), the lengthwise cut G1 produced the most force-loss, but did so much less efficiently per volume than the other cuts in that group,

especially F2, which disrupted the muscle's cross-section as it tapers towards the proximal aponeurosis.

For the multicut variant models of the standard VML (Fig. 3.7), the maximum cross-sectional area loss was relatively similar, so most variability appears to come from volume-loss and position. Models that included H 1, (the section closest to the proximal aponeurosis) were the most volume efficient at lowering model force. Models that included combinations with section H 8, the section above the distal aponeurosis and slightly smaller cross-sectional area loss, suffered in a decrease of force-loss efficiency. In the thin 1 mm multicut model (Fig. 3.8), force-loss behaves in an exponential fashion, with model I 1 7 (all sections 1 through 7 removed) approaching 100% force-loss despite being relatively little increase in additional volume-loss.

Superimposing the results of all the injury models into single plots was also used to determine whether volume or cross-section was the driving factor in force-loss (Fig. 3.9). When fitted to a second-degree polynomial, the CSA (Fig. 3.9iii) had a higher  $R^2$  ( $R^2 = .523$ ) than the volume (Fig. 3.9i) plot ( $R^2 = .277$ ). Additionally, looking that efficiency of force-loss by normalizing by volume-loss, the volume plot (Fig. 10ii) had a poor correlation ( $R^2 = -0.089$ ) compared to CSA (Fig. 3.9iv) ( $R^2 = .570$ ).

Finally, the models that had some section of the injury boundary above the distal aponeurosis were plotted against force-loss (Fig. 3.9v). While most injuries did not fall under this category, several standard VML multicut models did (those that included sections H 6, H 7, and H 8), as well A1, B2, E1, and F1. Overlap with the aponeurosis was strongly correlated with diminishing force-loss ( $R^2 = .507$ ), with the model H 1 6 with the lowest amount of relative overlap with the injury length (proximal-distal) also producing the highest forces. Additionally, normalizing by volume-loss (Fig. 3.10vi) produced an even stronger correlation ( $R^2 = .842$ ).

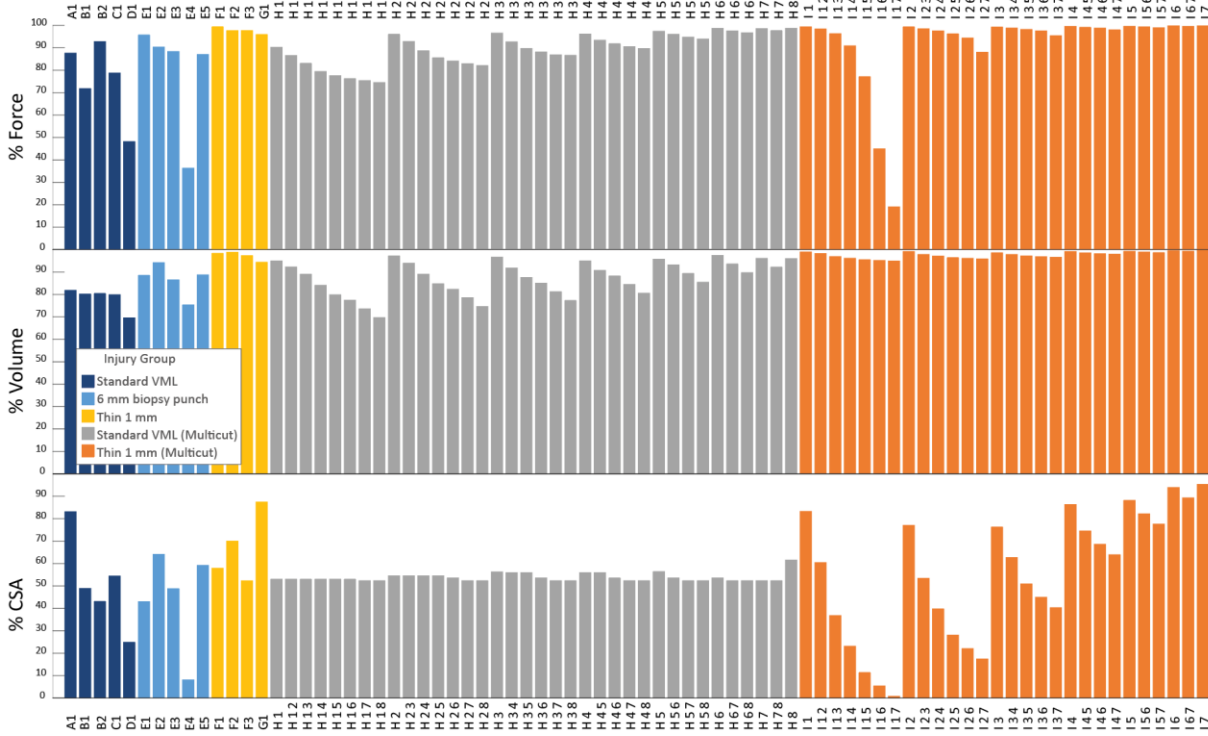


Figure 3.3: The complete results for all VML models. The values in the Y axis are normalized to the force measured in their respective intact models, for example A1's force was compared to A's force (Figure 2).

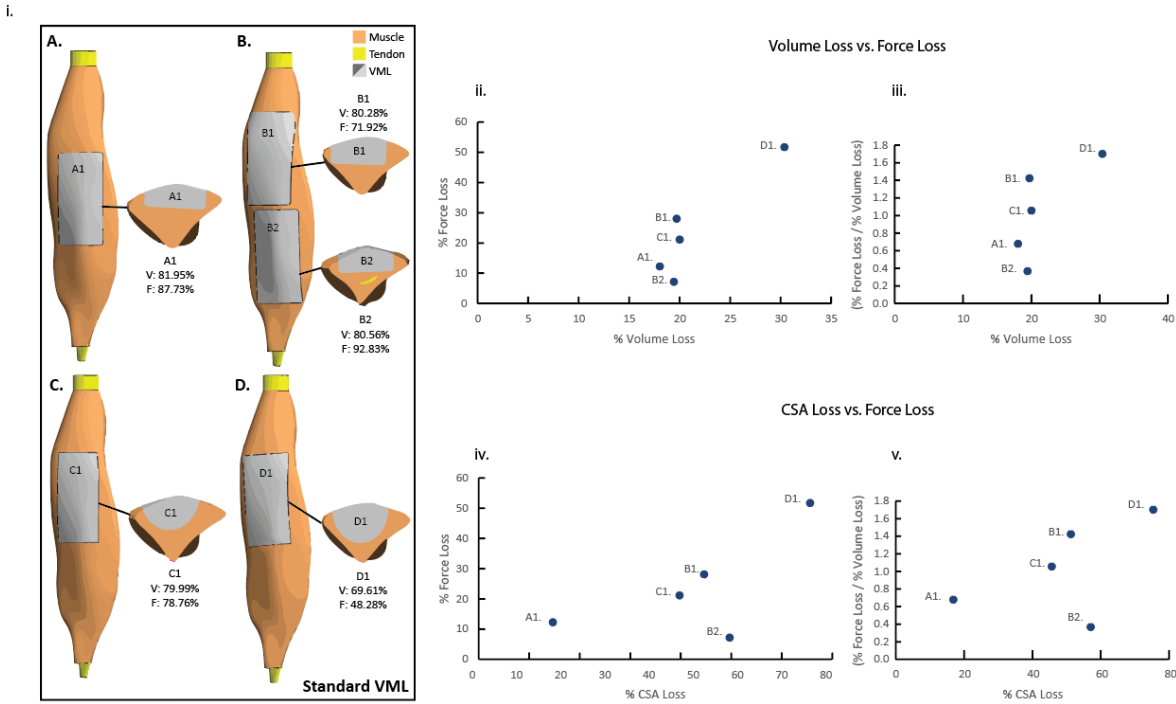


Figure 3.4: i: VML injury types in the Standard VML group, listing the percent volume (V) and force (F) compared to their lettered intact model (Figure 2). ii: Percent force-loss compared to percent volume-loss. iii: percent force-loss

(normalized to volume-loss) compared to volume-loss. iv: Percent force-loss compared to percent CSA loss. v: percent force-loss (normalized to volume-loss) compared to percent CSA loss.

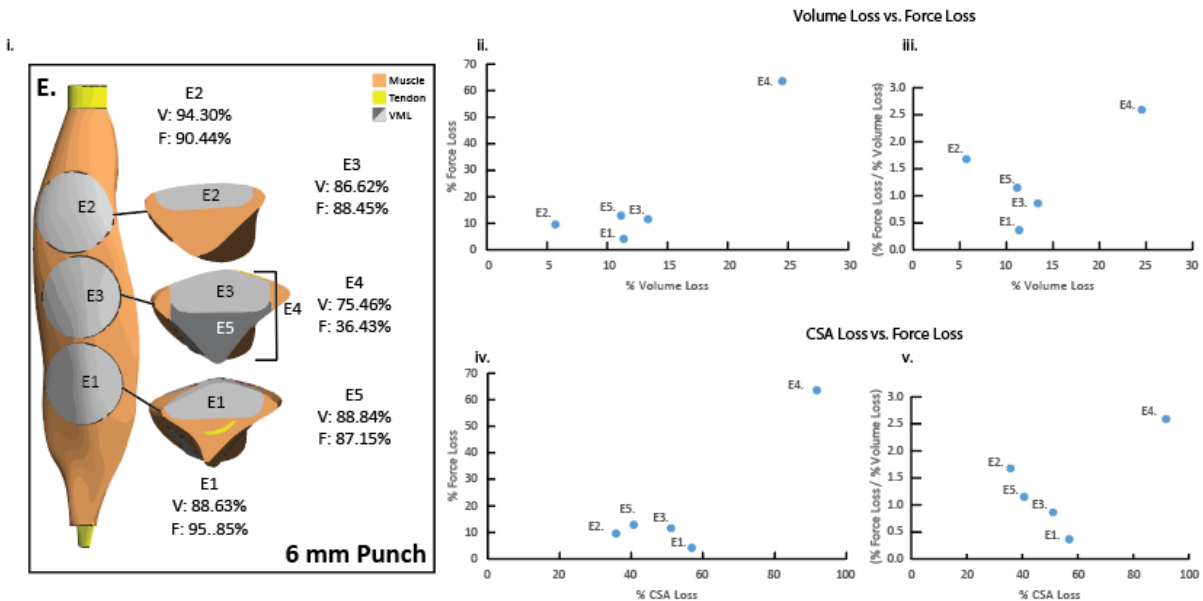


Figure 3.5: i: VML injury types in the 6 mm Punch group, listing the percent volume (V) and force (F) compared to their lettered intact model (Figure 2). ii: Percent force-loss compared to percent volume-loss. iii: percent force-loss (normalized to volume-loss) compared to volume-loss. iv: Percent force-loss compared to percent CSA loss. v: percent force-loss (normalized to volume-loss) compared to percent CSA loss.

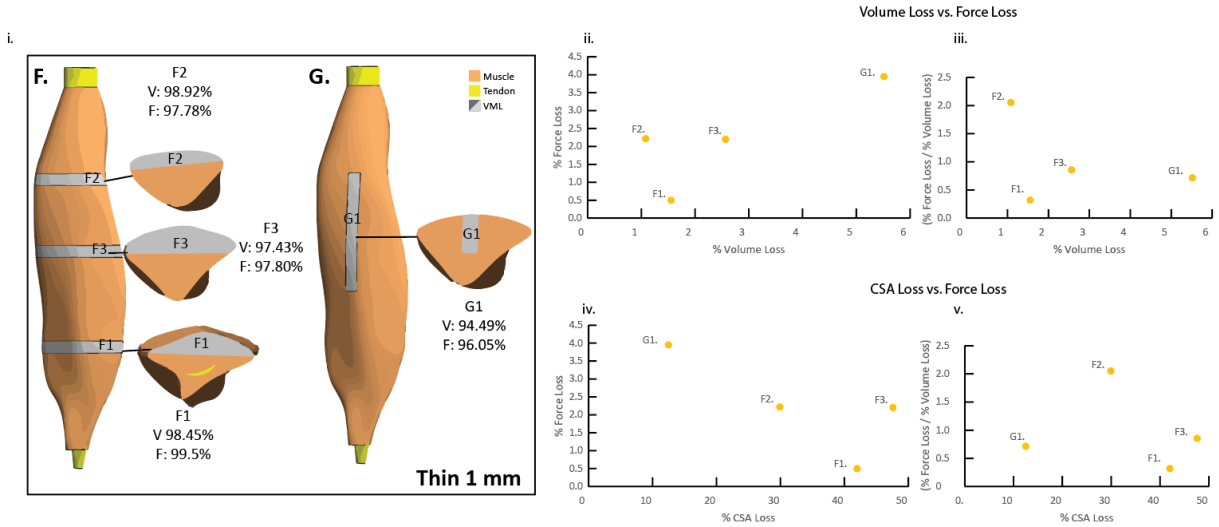


Figure 3.6: i: VML injury types in the Thin 1 mm group, listing the percent volume (V) and force (F) compared to their lettered intact model (Figure 2). ii: Percent force-loss compared to percent volume-loss. iii: percent force-loss (normalized to volume-loss) compared to volume-loss. iv: Percent force-loss compared to percent CSA loss. v: percent force-loss (normalized to volume-loss) compared to percent CSA loss.

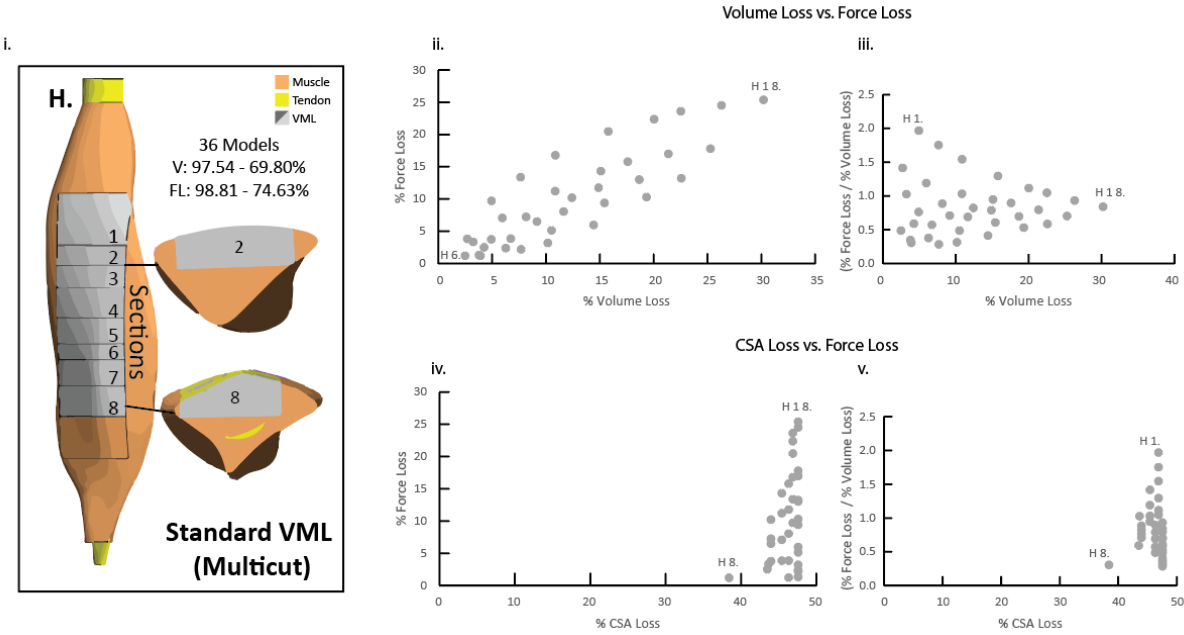


Figure 3.7: i: VML injury types in the Standard VML (Multicut) group, listing the percent volume (V) and force (F) compared to their lettered intact model (Figure 2). The sections 1 through 8 illustrate mesh boundaries that can be used to remove elements to make a variably dimensioned injury. An additional section was meshed below section 8, but was not used. Models in this class are designated as H X Y, with X being the first section removed in a set, and Y the last section removed. For example, H 3 6 would mean that the sections 3, 4, 5, and 6 were removed from the model. ii: Percent force-loss compared to percent volume-loss. iii: percent force-loss (normalized to volume-loss) compared to volume-loss. iv: Percent force-loss compared to percent CSA loss. v: percent force-loss (normalized to volume-loss) compared to percent CSA loss.

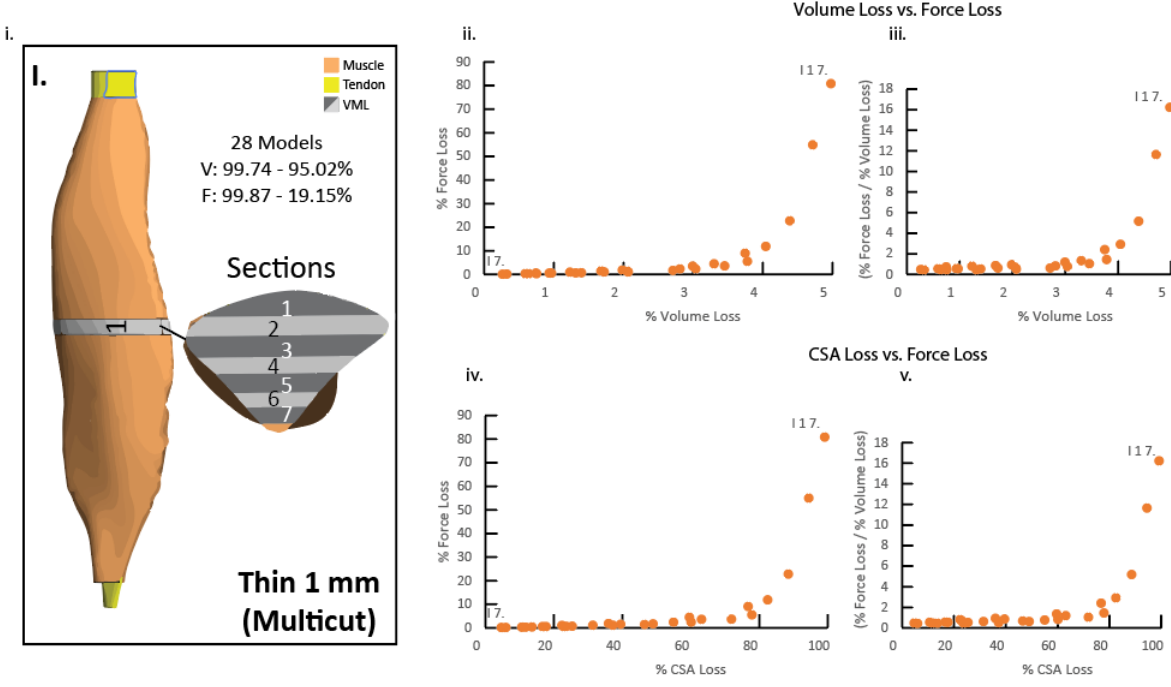


Figure 3.8: i: VML injury types in the Thin 1 mm (Multicut) group, listing the percent volume (V) and force (F) compared to their lettered intact model (Figure 2). The sections 1 through 8 illustrate mesh boundaries that can be used to remove elements to make a variably dimensioned injury. An additional section was meshed below section 8, but was not used. Models in this class are designated as I X Y, with X being the first section removed in a set, and Y the last section removed. For example, I 3 6 would mean that the sections 3, 4, 5, and 6 were removed from the model. ii: Percent force-loss compared to percent volume-loss. iii: percent force-loss (normalized to volume-loss) compared to volume-loss. iv: Percent force-loss compared to percent CSA loss. v: percent force-loss (normalized to volume-loss) compared to percent CSA loss.

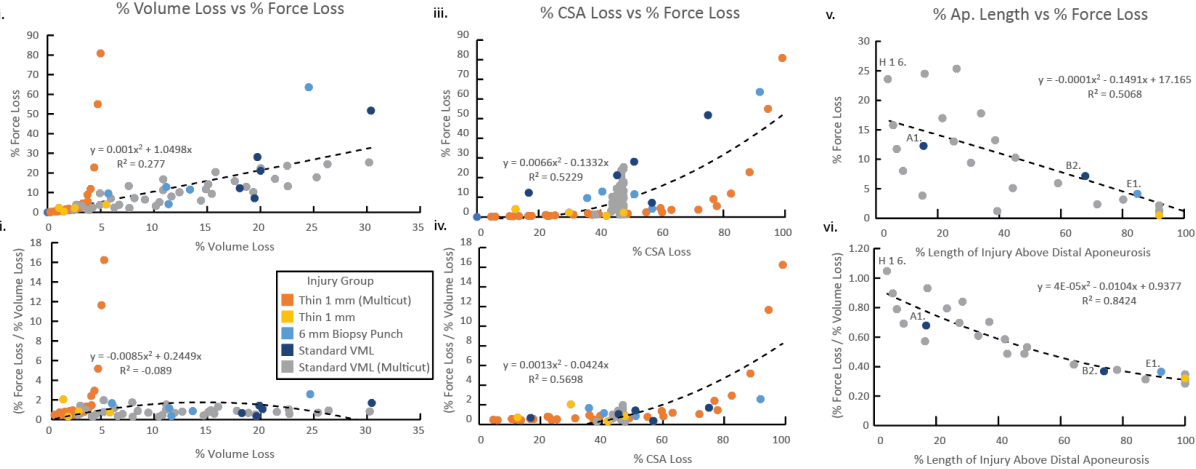


Figure 3.9: i: Force-loss versus volume-loss from all VML models. ii: Force-loss (normalized to volume-loss) versus volume-loss from all VML models. iii: Force-loss versus CSA-loss from all VML models. iv: Force-loss (normalized to volume-loss) versus CSA-loss from all VML models. v: The percentage of force-loss compared to what percentage of a

*model's proximal-distal length overlap the aponeurosis length, for those models that did so. vi: The percentage of force-loss (normalized to volume-loss) compared to what percentage of a model's proximal-distal length overlap the aponeurosis length, for those models that did so. All trendlines are 2<sup>nd</sup> order polynomials. Trendlines in i, ii, iii, and iv are intersected at  $x = 0$ .*

### 3.5 Discussion

The large number of models developed in the course of this work, several of which were aimed to represent traditional VML injuries in rat models (Mintz et al., 2020; Wu et al., 2012), alternate methods using a 6 mm biopsy punch (Dolan et al., 2022a), and theoretical injuries to give further insight on volume and locational effects. The standard VML models, which cover a roughly 10 x 5 area on the anterior surface of the TA in these models, could also be stand-ins for the larger 10 x 7 x 3 mm surgically induced injuries that are also used in VML studies, possibly on bigger TA volumes than those used for this model. The difference in results of the standard VML (models A1, B1, B2, C1, D1) and the biopsy punch (E1, E2, E3, E4, E5), shows that even among similar injury geometries, a great deal of variability can be generated through alterations in location and depth. Experimenters should continue to take care in accounting for variability of any induced injury for measurement purposes, as some positional changes or volume changes might greatly expand a cohort's measured standard deviation of force-loss. Even so, FE modeling may provide predictive avenues to estimate force-loss in rats before any injuries are induced, given enough details about the amount injury dimensions and location, such as how the D1 model closely matched the results of a central surgically induced VML injury in the group of 12-week-old Lewis rats (Fig. 3.1B).

A previously developed FE model of VML in rat latissimus dorsi muscle (Westman et al., 2019) found the a strong connection between the number of disrupted end-to-end fibers with force-loss. While the TA model developed for this work has more complexity with fiber arrangement and muscle geometry, the results of our work continue to support those conclusions. CSA was more closely associated with force-loss than volume, which in a

physiological sense, would be analogous the amount of end-to-end fibers disrupted, especially near the proximal end of the TA muscle where the fibers converge as the muscle tapers into the proximal tendon. Therefore, any VML injury located proximally would be a greater potential impact on force-loss, which also supported by several of the models. In the standard VML (Fig. 3.4) models, B1 produced both more overall force-loss and force-loss per volume-loss than any of the other injuries around 20% volume-loss. Additionally, F2 from the thin 1 mm model (Fig. 3.6) and H 1 (Fig. 3.7) were the most efficient at generating force-loss per volume-loss. We can likely conclude that VML injuries near muscle architecture that might be considered a fiber “bottleneck” would be especially effective at generating force-loss than equivalent injuries elsewhere in the muscle. Additionally, the results of injury length overlapping with aponeurosis length (Fig 3.9v, vi) are interesting. The TA’s internal aponeurosis for the distal tendon creates a unique pennation where the fibers above and below the plane of the aponeurosis converge inwards. The loss some of these fibers through injury appear to compensated with the ability of the aponeurosis to act as a supporting structure, and anchor the remaining fibers around the injury site, and to continue to generate end-to-end force. It is the noted practice of those creating standard VML style injuries (Mintz et al., 2020; Wu et al., 2012) to avoid interfering with the distal aponeurosis, and the model results suggest that is well founded on a force-loss level, as near that location may produce less force-loss than desired, and that any disruption or severing of that internal aponeurosis would opposingly have an extreme deleterious effect on the muscle’s ability to transmit force and severely limit any potential force recovery. Either way, staying away from the aponeurosis in inducing a VML injury for a repair assessment appears to be good sense.

An additional notion is arrived at with the stronger correlation to CSA with force-loss than volume. Depending on an injury’s dimensions, it may be sufficient to attempt to bridge a

cross-section between parts of the surviving muscle around an injury site than to generate new, fully contractile muscle tissue at a location. Indeed, muscle's response to preserve force-generation in regions it cannot fully repair is fibrosis (Mahdy, 2019), which accomplishes force-bridging. As such, functional fibrosis is a topic of investigation in the VML space (Dolan et al., 2022b). However, based on model results, the injuries at which would be the best candidates for this kind approach are likely small enough that typical muscle regeneration could occur. It remains a design challenge, then, to deal with VML injuries that both are significant losses in muscle volume as well as significant disruptors in cross-sectional area; scaffolding approaches (Corona et al., 2014; Passipieri et al., 2017) that can both encourage muscle regeneration while providing intermediate stages for space-filling and force-transmission in the injury site may provide an effective balance.

#### C.O.I. Statement

The authors have no conflicts of interest to declare.

#### Acknowledgements

The authors would like to expressively thank (in no particular order) Dr. Julie Passipieri, Dr. Jack Dienes, Dr. Amanda Westman, Michael Rariden, and Sydney Shriver, as well as the other members of the Christ Lab, past and present, for their invaluable help in sharing experimental data and building the framework for this project.

## Chapter 4

### Force-velocity Behavior Impacts Strain Distribution in FE Muscle Models

Acknowledgements: Silvia S. Blemker

*I feel the need – the need for speed!*

- Peter “Maverick” Mitchell (*Top Gun*, 1986)

#### 4.1 Abstract

Skeletal muscles are complex structures with nonlinear constitutive properties. This complexity often requires finite element (FE) modeling to better understand muscle behavior and response to activation, especially the fiber strain distributions that can be difficult to measure *in vivo*. However, many FE muscle models designed to study fiber strain do not include force-velocity behavior. To investigate force-velocity property impact on strain distributions within skeletal muscle, we modified a muscle constitutive model with active and passive force-length properties to include force-velocity properties. We implemented the new constitutive model as a plugin for the FE software FEBio and applied it to four geometries: 1) a single element, 2) a multiple-element model representing a single fiber, 3) a model of tapering fibers, and 4) a model representing the bicep femoris long head (BFLH) morphology. Maximum fiber velocity and boundary conditions of the finite element models were varied to test their influence on fiber strain distribution. We found that force-velocity properties in the constitutive model behaved as expected for the single element and multi-element conditions. In the tapered fiber models, fiber strain distributions were impacted by changes in maximum fiber velocity; the range of strains increased with maximum fiber velocity, which was most noted in isometric contraction simulations. In the BFLH model, maximum fiber velocity had minimal impact on strain distributions, even in the context of sprinting. Taken together, the combination of muscle model geometry, activation, and displacement parameters play a critical part in determining the magnitude of impact of force-velocity on strain distribution.

KEYWORDS: Skeletal Muscle, Finite Element, Muscle Fiber, FEBio, Force-Velocity, Constitutive Modeling

## 4.2 Introduction

Over the last two decades, it has become clear that skeletal muscle exhibits complex nonuniform strain distributions during contraction (Azizi and Deslauriers, 2014; Pappas et al., 2002), which ultimately influences muscle force generation. This advancement in understanding emerged from measurements of tissue-level deformations in muscle using *in vivo* techniques, including cine MRI (Fiorentino et al., 2013; Hodgson et al., 2006; Pappas et al., 2002; Zhong et al., 2008), sonomicrometry (Gillis and Biewener, 2002; Soman et al., 2005), and ultrasound (Bennett et al., 2014; Leitner et al., 2020). While the overall conclusion that strain distributions are nonuniform is consistent across the literature, the precise patterns of deformation vary substantially across studies because local strain distributions are impacted by a wide variety of factors, such as muscle architecture, neuromuscular activation, muscle tissue properties, internal aponeurosis morphology, and more (Azizi and Deslauriers, 2014; Rehorn and Blemker, 2010). It is challenging to quantify how these factors influence muscle deformation through experiments alone, due to the difficulty in experimentally isolating the influence of each factor.

Computational modeling provides an excellent framework for capturing and understanding complex muscle deformation and contraction, isolating the influence of biomechanical factors, performing what-if experiments, and explaining cause-and-effect relationships. Indeed, finite element muscle modeling studies have shown that complex 3D muscle morphology (Blemker and Delp, 2005; Fiorentino and Blemker, 2014; Knaus et al., 2022; Rahemi et al., 2015; Röhrle and Pullan, 2007), aponeuroses (Chi et al., 2010; Fiorentino and Blemker, 2014; Knaus et al., 2022; Rehorn and Blemker, 2010), and interactions with neighboring tissues and muscles (Maas et al., 2003) all contribute to strain distributions. Due to

the nonlinear nature of the passive and active force-length characteristics of muscle, varying degrees of muscle activation and length change also lead to varied degrees of strain heterogeneity. For example, conditions of elevated activated lengthening, such as during sprinting, lead to greater levels of strain heterogeneity and thus higher localized strains, which provides an explanation for increased susceptibility of the hamstrings to strain injury (Fiorentino et al., 2014). While these simulations account for the nonlinear active and passive force-length characteristics of muscle fibers, they do not incorporate the force-velocity property of muscle (Hill, 1938). It stands to reason that the force-velocity property could have a balancing effect on force transmission between in-series fiber segments, as individual sarcomeres lengthen and shorten individually to compensate for their neighbors (Morgan, 1990; Morgan and Proske, 2006). Therefore, it is plausible that strain distributions predicted by finite-element simulations would be impacted by the force-velocity property.

Implementation of the force-velocity property in constitutive models of skeletal muscle tissue has been successful (Ehret et al., 2011; Marcucci et al., 2017; Ross et al., 2021); however, these formulations remain reliant on specialized software packages that limits dissemination to other researchers. Furthermore, it remains unclear how much the force-velocity relationship impacts strain distributions predicted by finite element models. Taking advantage of recent developments in free and open-source finite element modeling, such as FEBio (Maas et al., 2012) with its robust plugin system (Maas et al., 2018), can provide additional avenues to use and share specialized formulations of constitutive models.

The goals of this study were to: 1) develop, implement, and numerically validate a force-velocity constitutive model of muscle within FEBio that can be easily shared and implemented in both existing and new finite element models, and 2) use the force-velocity constitutive model to determine if, and under what conditions, the force-velocity property impacts tissue-level strain

distributions. To explore this question, we created models with both simplified and complex geometries, simulated during both simplified and physiological conditions, including a model of the biceps femoris long head undergoing eccentric activation during sprinting.

### 4.3 Materials and Methods

#### *Implementation of the Force-Velocity Behavior in FEBio*

We built upon a previously developed constitutive model of muscle (Blemker et al., 2005) that was implemented as an option in FEBio under the name “muscle material” as an uncoupled elastic material. The muscle is a transversely-isotropic, hyper-elastic, nearly-incompressible material that models muscle’s active and passive properties, using an uncoupled formulation of strain energy:

$$\Psi(C, a_0) = \Psi_{iso} + \Psi_{vol}(J) \quad (4.1)$$

Where  $C$  is the right Cauchy-Green deformation tensor,  $a_0$  is the fiber vector, and  $J$  is the Jacobian. The deviatoric part of the strain energy equation is further broken down into three components, which include contributions of strain and fiber contraction:

$$\Psi_{iso} = W_{along-fiber\ strain} + W_{cross-fiber\ strain} + W_{fiber\ contraction} \quad (4.2)$$

A detailed explanation of the terms and derivation can be found in the description of the previous model (Blemker et al., 2005).

The  $W_{fiber\ contraction}$  term in this constitutive model incorporates the active force-length behavior but lacks the active force-velocity behavior. Therefore, we extended FEBio’s open source C++ implementation for this constitutive model with modifications written in Microsoft Visual Studio 2015, in order to produce a plugin that provides an additional option to include force-velocity behavior. Onwards, we will refer to the new constitutive model using the

abbreviation FV (force-velocity), while the previously developed model will be referred to as NFV (no force-velocity). The FV material features include all the capabilities of the NFV material, with the addition of a user defined, multiple parameter force-velocity curve, and the additional post-processing ability to record and display muscle fiber velocity for elements at each timestep. To foster sharing of the of FV material, the plugin and example files will be made available on simTK.org.

The material fiber direction in the undeformed configuration is defined using the unit vector  $a_0$ . Fiber stretch  $\lambda$  is calculated by the following equation, where  $F$  is the deformation gradient and  $J$  is the Jacobian:

$$\lambda = \|F a_0\| J^{-1/3} \quad (4.3)$$

The fiber velocity is then calculated at each time step as a time derivative of the fiber stretch:

$$v = -\frac{d\lambda}{dt} \quad (4.4)$$

In this question, a positive velocity corresponds to shortening fibers. The force-velocity behavior (Edman, 1988; Hill, 1938) is implemented as  $f_{scale}$ :

$$f_{scale} = \begin{cases} d, & v < -v_{max} \\ \frac{d(d-1)\left(1-\frac{-v}{v_{max}}\right)}{1+k_{cc}k_{ec}\frac{-v}{v_{max}}}, & -v_{max} \leq v \leq 0 \\ \frac{1+\frac{-v}{v_{max}}}{1-k_{cc}\frac{-v}{v_{max}}}, & 0 < v \leq v_{max} \\ 0, & v > v_{max} \end{cases} \quad (4.5)$$

The constant  $d$  is the maximum force ratio at the eccentric horizontal asymptote,  $v$  is fiber velocity at a given timestep,  $V_{max}$  is the maximum velocity, and  $k_{cc}$  and  $k_{ec}$  represent constants of curvature for the concentric and eccentric portions of the force-velocity curve, respectively. In our models, the values for the constants  $d$ ,  $k_{cc}$  and  $k_{ec}$  (Table 4.1) were defined such that the lengthening and shortening portions of the FV curve are mirrored, and that the  $k_{cc}$  and  $d$

generated a curve that aligns to a previous generalization of the force-velocity curve (Zajac, 1989).

Table 4.1: FE Material Properties

<b>Muscle Tissue (All Models)</b>		
<i>Muscle Material (FV and NFV)</i>		
$\sigma_{\max}$	0.125	MPa
P1	0.04	*
P2	6.6	*
$\lambda_{\text{off}}$	1	*
$\lambda_{\max}$	1.06	*
G1	$3.87 \times 10^{-3}$	MPa
G2	$2.24 \times 10^{-2}$	MPa
K	$5.0 \times 10^2$	MPa
<i>FV Properties (FV)</i>		
$K_{\text{cc}}$	6.667	*
$K_{\text{ec}}$	1.4375	*
d	1.7244	*
$V_{\max}$	0.1 - 10	Fiber Lengths/s
<b>Tendon Tissue (BFLH Models)</b>		
<i>Mooney-Rivlin</i>		
C1	45	MPa
C2	0	MPa
K	5000	MPa
<i>Uncoupled Fiber with Exp-Power Law</i>		
$\alpha$	0	*
$\beta$	2.5	*
$\xi$	500	MPa

\*: unitless parameter

Since the force-velocity relationship only applies to active muscle contraction,  $f_{scale}$  modulates the active component ( $f_{active}$ ) of the total fiber force, as follows:

$$f_{total}^{fiber} = f_{passive}(\lambda) + \alpha f_{scale}(v) f_{active}(\lambda) \quad (4.6)$$

The detailed equations for  $f_{passive}$  and  $f_{active}$  are provided in Blemker et al., 2005. Fiber force is then related to the muscle strain energy function:

$$\lambda \frac{\partial W_{fiber\ contraction}}{\partial \lambda} = \sigma_{max} f_{total}^{fiber}(\lambda, f_{scale}, \alpha) \frac{\lambda}{\lambda_{opt}} \quad (4.7)$$

where  $\sigma_{max}$  is the maximum isometric stress,  $\alpha$  is the activation level (between 0 and 1), and  $\lambda_{opt}$  is the fiber stretch at which the sarcomeres within the corresponding tissue reach optimal length.

### ***Single Element Model***

To numerically confirm that the stress calculations from the FV constitutive model were consistent with the expected force-velocity relationship, a single 8-node hexahedral element (1 mm<sup>3</sup>) model (Fig. 4.1A) was created in FEBio 2.9.1 with the fiber direction assigned in the x direction. All eight nodes in the element were assigned prescribed displacements in the x direction to simulate shortening and lengthening. Four nodes on one face with zero displacement and four on the opposite face with a displacement varying over a range of 2 fiber lengths per second shortening to lengthening. Shortening and lengthening conditions were applied after reaching isometric maximum activation ( $\alpha = 1$ ) over 1 second. Additional nodal displacements in the y and z directions were defined to maintain volume within the element depending on the rate of prescribed x displacement. The stress along the fiber direction was measured immediately after the displacement initiated and normalized to the peak isometric stress before strain.

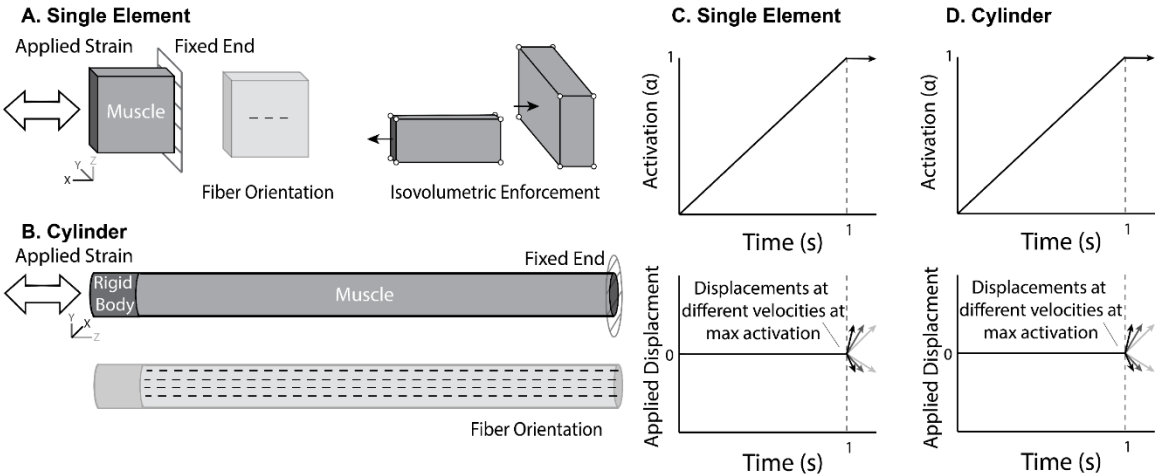


Figure 4.1: A: Geometric representation of the single element models. B: Geometric representation of the cylindrical models. C: Activation and applied displacement curves for single element models. D: Activation and applied displacement curves for cylindrical models.

**Multi-Element Cylindrical Model**

To confirm the functionality of the constitutive model’s behavior in a model with multiple elements, a cylindrical model (2,112 hexahedral elements, length = 10 mm, radius = 0.5 mm) was built (Fig. 2.1B). The fiber direction within all the elements were directed longitudinally. The model was initially prescribed a ramped isometric activation ( $\alpha = 1$ ) over 1 second. Immediately afterwards, one end of the cylinder underwent a prescribed concentric or eccentric displacement at a fixed rate to mimic a catch and release fiber experiment (Katz, 1939). Immediately following the displacement, the reaction force at the end of the cylinder was compared to the maximum reaction force measured during the isometric activation. Simulations were performed with prescribed to velocities ranging from -2 to 2 fiber lengths per second. The results of this simulation were also compared with a wide range of published force-velocity measurements (Edman, 1988; Hill, 1938; Roots et al., 2007; Stienen et al., 1992; Weidner et al., 2022) (Fig. 4.4).

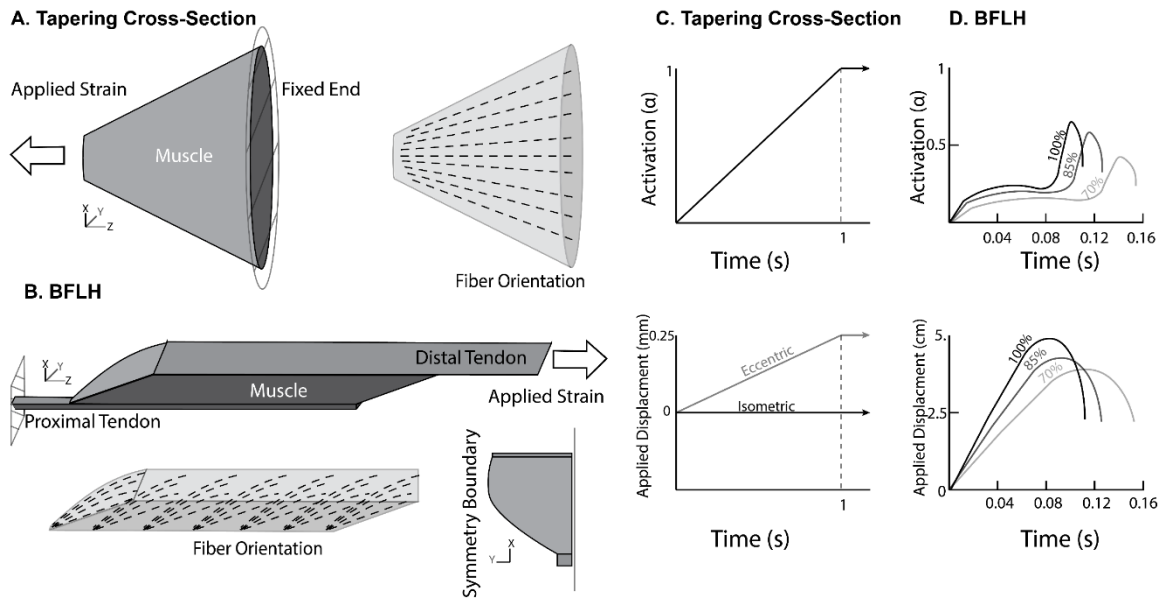


Figure 4.2: A: Geometric representation of the tapering cross-section models. B: Geometric representation of the BFLH models. C: Activation and applied displacement curves for tapering cross-section models. D: Activation and applied displacement curves for BFLH models.

### Tapering Cross-Section Model

The purpose of the tapering cross-section model was to examine the impact of the force-velocity property on strain distributions in a setting that is known to experience nonuniform strains due to converging fibers. The model consisted of 40,504 tetrahedral elements and had a shape of a flat-headed cone (Fig 4.2A) with a wide end of a radius of 5 mm, a length of 6 mm, and a narrow end radius of 1 mm. The radii sizes at the ends were chosen to match the 5:1 proximal to distal aponeurosis width ratio of a previous model of the bicep femoris long head (Rehorn and Blemker, 2010), with a length chosen such that the end-to-end fibers had a pennation average of  $17.5^\circ$  among all elements, with variation depending on the radius of the model (the outermost radius had a pennation of  $33.7^\circ$ , while the center had a pennation of  $0^\circ$ ). The  $17.5^\circ$  average pennation corresponds closely to the average pennation found in measurements of the bicep femoris long head at  $60^\circ$  knee flexion (Timmins et al., 2015). Fibers directions were defined to converge from the wider face into the narrow end. The model was allowed to ramp up to maximum activation ( $\alpha = 1$ ) over 1 second isometrically, or

with a prescribed active lengthening. In the prescribed active lengthening models, a 0.25 mm displacement was applied normal on the nodes of the narrow face, while zero displacement was enforced on the nodes on the wide face. The material properties were based on the muscle properties of a bicep femoris long head model (Fiorentino et al., 2014) (Table 4.1), with the maximum velocity parameter defined at 0.1, 1, or 10 fiber lengths per second, as well as a model that did not incorporate the force-velocity behavior. Varying  $V_{\max}$  in this way allowed us to explore the impact of varying fiber characteristics from slow to fast myosin isoforms (Bottinelli et al., 1996).

### ***Biceps Femoris Long Head Model***

We used a previously developed model (Fiorentino et al., 2014) of the bicep femoris long head (BFLH) that had been applied to exploring the mechanisms of hamstring injuries by predicting strain distributions within the muscle during high speed running. The model's geometry (Fig. 4.2B) and dimensions were replicated to produce a new finite element model with the FV muscle constitutive model. The geometry (21,297 elements) was meshed with 4 node tetrahedral elements using Coreform Cubit. Fiber mapping in the BFLH muscle was performed by assigning fiber vectors to each tetrahedral element based on a vector map of the previous model's fiber distribution, resulting in a pennation angle of 15°. The fiber directions in both tendons were defined uniformly, pointing longitudinally along the Z axis. Three components (proximal tendon/aponeurosis, muscle, and distal tendon/aponeurosis) were meshed independently. Contact between the muscle and the tendon/aponeuroses was enforced by the tied facet-on-facet option in FEBio. Previous dynamic simulations of sprinting at 70%, 85%, and 100% of maximum speed (Chumanov et al., 2007) were used to prescribed time-varying displacement and activation profiles (Fig. 2B), as in Fiorentino et al., 2014. Material

parameters of the muscle were the same as the previous BFLH model (Fiorentino et al., 2014), and tendon properties from a previous model of an aponeurosis (Knaus et al., 2022). In order to examine the impact of the force-velocity function, simulations were performed with the NFV muscle material (Blemker et al., 2005) and with FV muscle material with varied definitions for maximum contraction velocity ( $V_{\max} = 1, 2, \text{ or } 10$  fiber lengths per second).

### ***Data Analysis***

For the tapering cross-section model simulations, post-processing was performed in Mathworks MATLAB by extracting the fiber strain ( $\lambda - 1$ ), fiber velocities, and node locations from each element from the FEBio Studio. Comparison of both fiber strain and fiber velocities distributions was performed at the end of the isometric and active lengthening simulations at  $t = 1$  second, the time at which muscle activation and any prescribed lengthening through boundary conditions become static.

Post-processing of simulation BFLH strain distributions results were performed in MATLAB using data from FEBio Studio in the same manner as the tapering cross-section model. Average fiber strain (along with the range for the muscle component) was tracked through all simulations speeds and  $V_{\max}$  iterations with respect to simulation time. Fiber velocity average and range was low-pass filtered with respect to simulation time. Localized spatial distributions of fiber velocity and fiber strain per element were analyzed in the 70% speed simulations at three time points: 1) highest lengthening velocity, 2) highest shortening velocity, and 3) peak fiber strain.

## **4.4 Results**

### ***Single Element and Cylinder Results***

For all results, shortening fiber velocities are considered positive while lengthening fiber velocities are considered negative, consistent with the common definition of the muscle force-

velocity curve (Edman, 1988; Hill, 1938). Single element tests confirmed correct adherence to the implemented force-velocity relationship (Fig. 4.3). The multi-element cylindrical model also predicted a force-velocity behavior consistent with the defined equation as well as a wide variety of published experimental observation (Fig. 4.4).

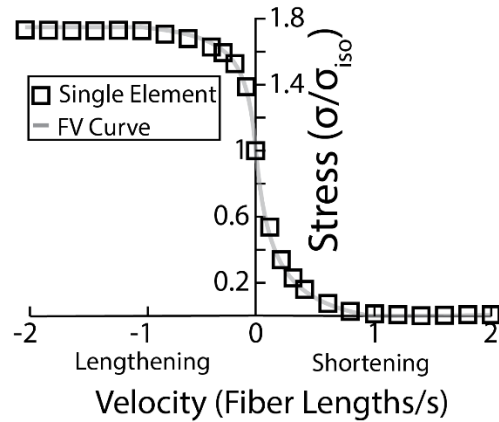


Figure 4.3: Single element stress overlaid on the input FV curve.

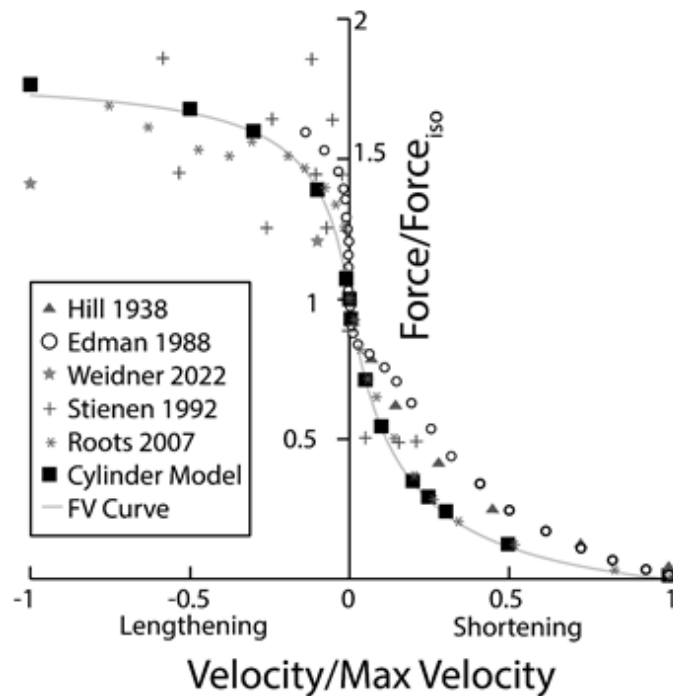


Figure 4.4: Cylindrical model results applied over the input FV curve, normalized to their maximum velocities. The cylindrical results are model lengths per second (the model representing a single fiber). FV results from several

*experiments in literature are also included (Edman, 1988; Hill, 1938; Roots et al., 2007; Stienen et al., 1992; Weidner et al., 2022).*

### ***Tapering Cross-Section Results***

The tapering cross-section models with the FV material showed a change in the distribution of fiber strain near the narrow and wide ends (Fig. 4.5), as well as total model force, when compared to the NFV models for both the isometric and eccentric models (Fig. 4.6). The NFV models experienced both higher maximums and lower minimums of fiber strain than the FV models. This effect was more pronounced in the isometric condition (NFV had a 53.5% higher peak of the average fiber strain than  $V_{\max} 0.1$ ) as compared to the active lengthening condition (NFV had a 9.0% higher peak of the average fiber strain than  $V_{\max} 0.1$ ). This effect diminished with increasing  $V_{\max}$  in both the isometric (NFV had a 2.8% higher peak of the average fiber strain than  $V_{\max} 10$ ) and active lengthening (NFV had a 2.4% higher peak of the average fiber strain than  $V_{\max} 10$ ). The forces predicted by the models were also influenced by the force-velocity properties, with FV  $V_{\max} 0.1$  producing 161% of the force of the NFV with the active lengthening conditions, and 85% of the NFV's force with the isometric conditions. Mapping the element fiber velocities in the context of the force-velocity curve revealed that in the lower  $V_{\max}$  models, the fiber velocities span a wider range across lengthening and shortening regions of the force-velocity curve, as compared to the range observed in the higher  $V_{\max}$  models. Additionally, the fibers towards the narrow end (which experienced higher fiber strain) of the model fell upon the lengthening side of the force-velocity curve, while the fibers at the wider end (experiencing lower fiber strain) were on the shortening side of the force-velocity curve.

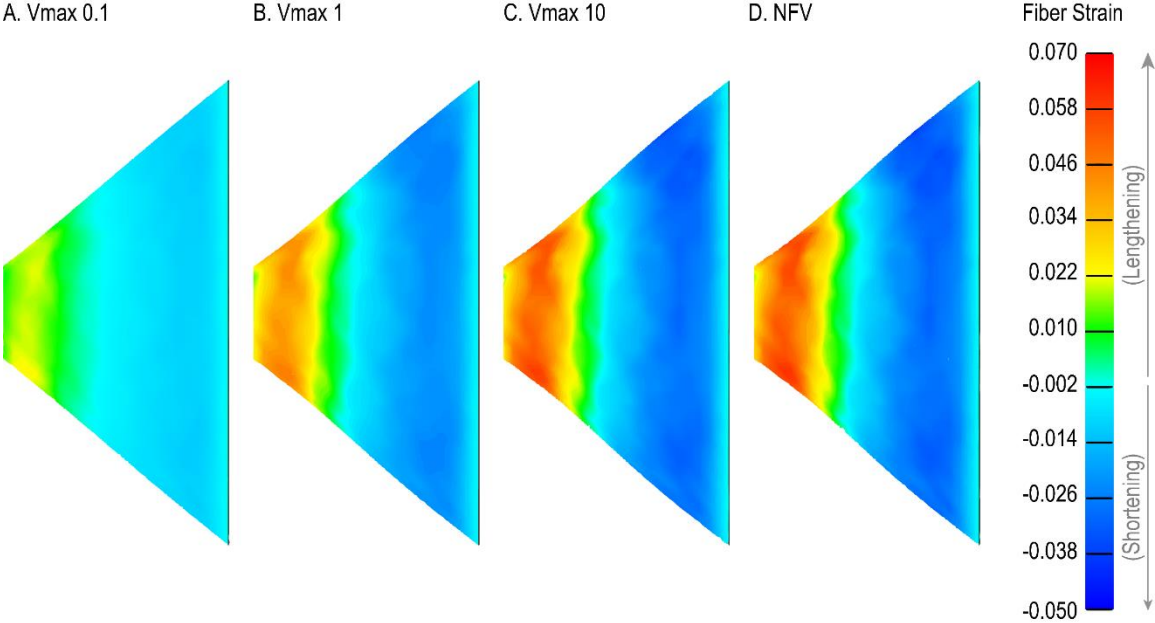


Figure 4.5: Color map of fiber strain for the tapering cross-section models under the isometric conditions at  $t = 1$  second at a side viewpoint. A:  $V_{max}$  of 0.1 fiber lengths per second. B:  $V_{max}$  of 1 fiber lengths per second. C:  $V_{max}$  of 10 fiber lengths per second. D. NFV model. Differing element size in the model towards the narrow end accounts for slight strain asymmetry across that edge.

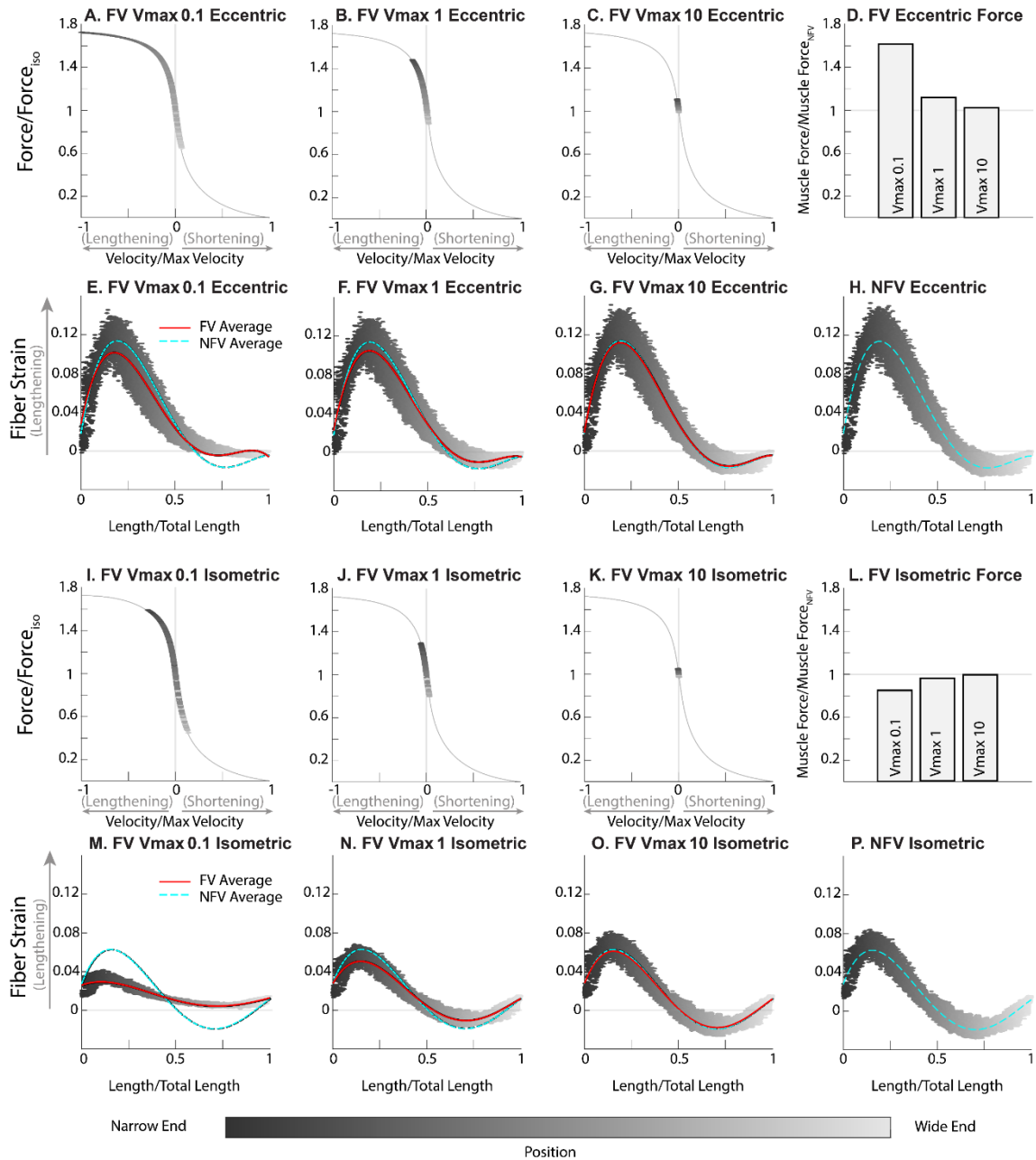


Figure 4.6: Normalized force-velocity distributions, normalized reaction force, and fiber strains for the tapering cross-section model. A-C: Normalized force-velocity distributions for the elements in the eccentric activation models. Gray-scale corresponds to the element's position along the length of the model. D: The force generated by the eccentric activation models normalized by the NFV force. E-H: The fiber strain distributions for the eccentric activation models (blue dotted line: NFV fiber strain mean, red solid line: model fiber strain mean, points: individual elements). I-K: Normalized force-velocity distributions for isometric activation models. Gray-scale corresponds to the element's position along the length of the model. L: Force generated by the isometric models compared to the NFV isometric model. M-P: Fiber Strain distributions of the isometric models. Vmax is in fiber lengths/s.

**BFLH Results**

Similar to previous simulations of the BFLH behavior during sprinting (Fiorentino et al., 2014), the local fiber strain increased with increased sprinting speed, also causing increasing local maximum along-fiber strain (Fig. 4.7). The average fiber strain was highest near the proximal aponeurosis, and lowest near the distal aponeurosis in all BFLH models and conditions, mirroring the strain distributions seen in previous simulations (Fiorentino et al., 2014). The computed fiber velocities also showed an increase in magnitude in conjunction with increasing model speed. The addition of the force-velocity property altered the fiber strain distribution in the 70% speed models throughout the simulation times, with greater effect at lower  $V_{\max}$  models (Fig. 4.9). Like the tapering cross-section models, there was modulation in model reaction force (measured at the end of the proximal tendon) with greater differences from the NFV reaction force observed at lower  $V_{\max}$ . The range of fiber strains were affected minimally, with the most noticeable difference occurring at the shortening velocity maximum time (Fig 4.9M through P). At this time point, the NFV having elements experiencing slightly higher maximum and lower minimum fiber strains (fiber strain ranged from 0.07 to 0.56 in NFV) than any of the FV model, with tighter distributions (although higher average fiber strain) occurring at the lower  $V_{\max}$  models (for example, fiber strain ranged 0.16 to 0.51 in  $V_{\max}$  0.1).

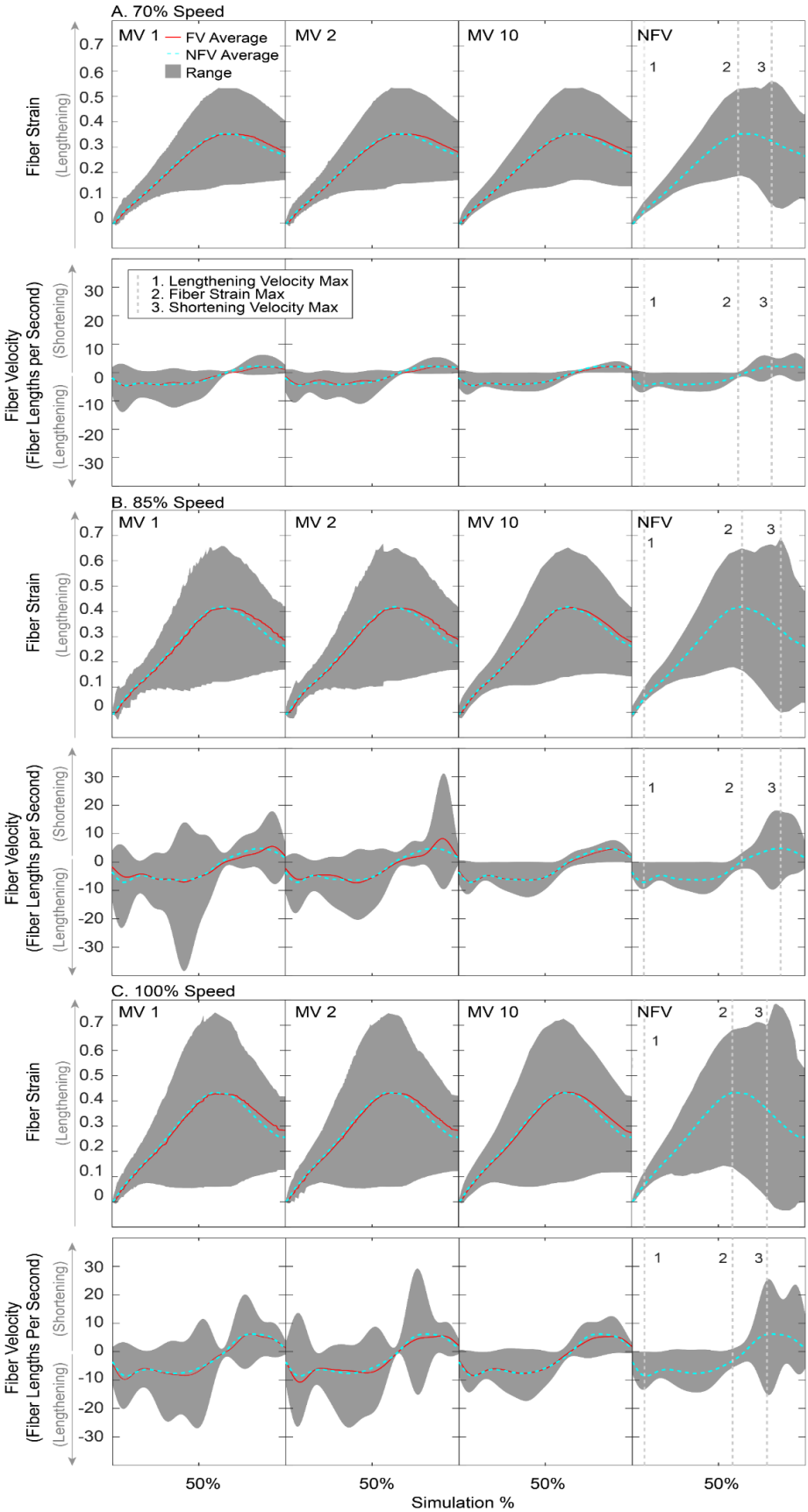


Figure 4.7: Average fiber strain and fiber velocity for A: 70% Speed, B: 85% Speed, and C: 100% Speed models at  $V_{max}$  (MV) of 1, 2, 10 fiber lengths per second, and NFV. Solid red lines: average values. Lengthening velocity is denoted as negative in the fiber velocity plots. Blue dotted lines: NFV averages. Vertical dotted lines: times of interest in the NFV model (1: time of lengthening velocity max, 2: time of maximum fiber strain, 3: time of shortening velocity max). Shaded regions: data range.

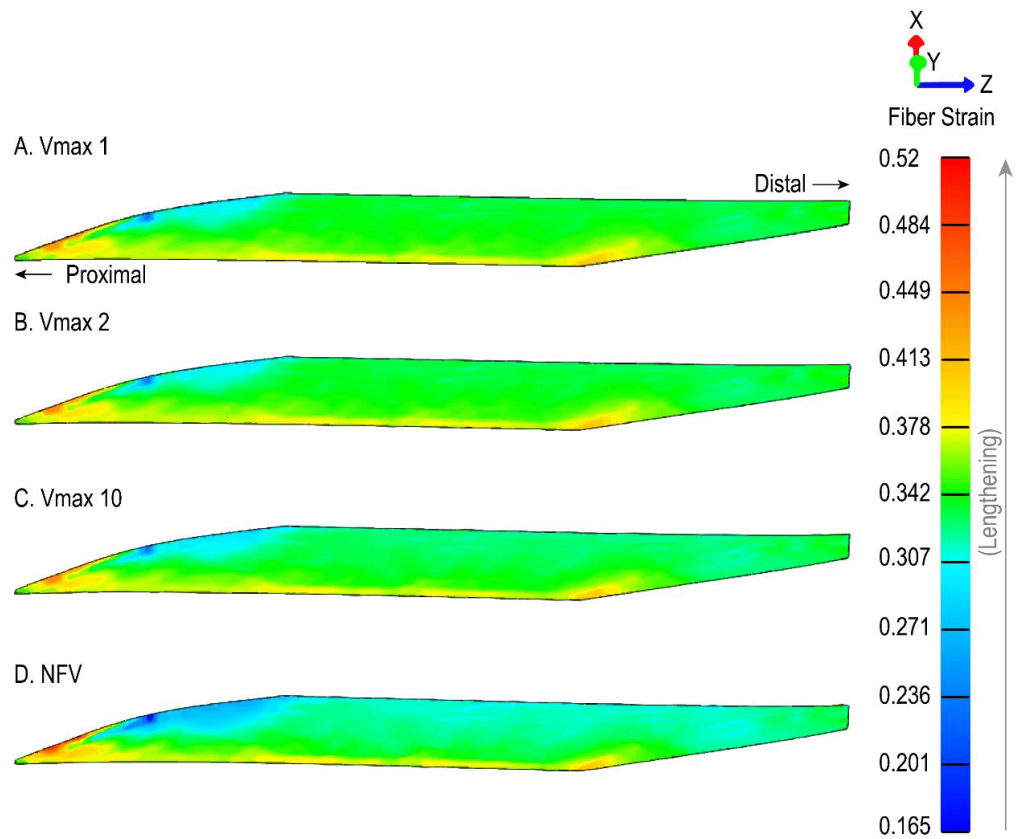


Figure 4.8: Color map of fiber strain for the BFLH at the time of maximum shortening velocity experienced by the 70% Speed NFV model ( $t = 0.123$  s). Viewpoint is angled at the lateral surface (tendons excluded) A:  $V_{max}$  of 1 fiber lengths per second. B:  $V_{max}$  of 2 fiber lengths per second. C:  $V_{max}$  of 10 fiber lengths per second. D: NFV model

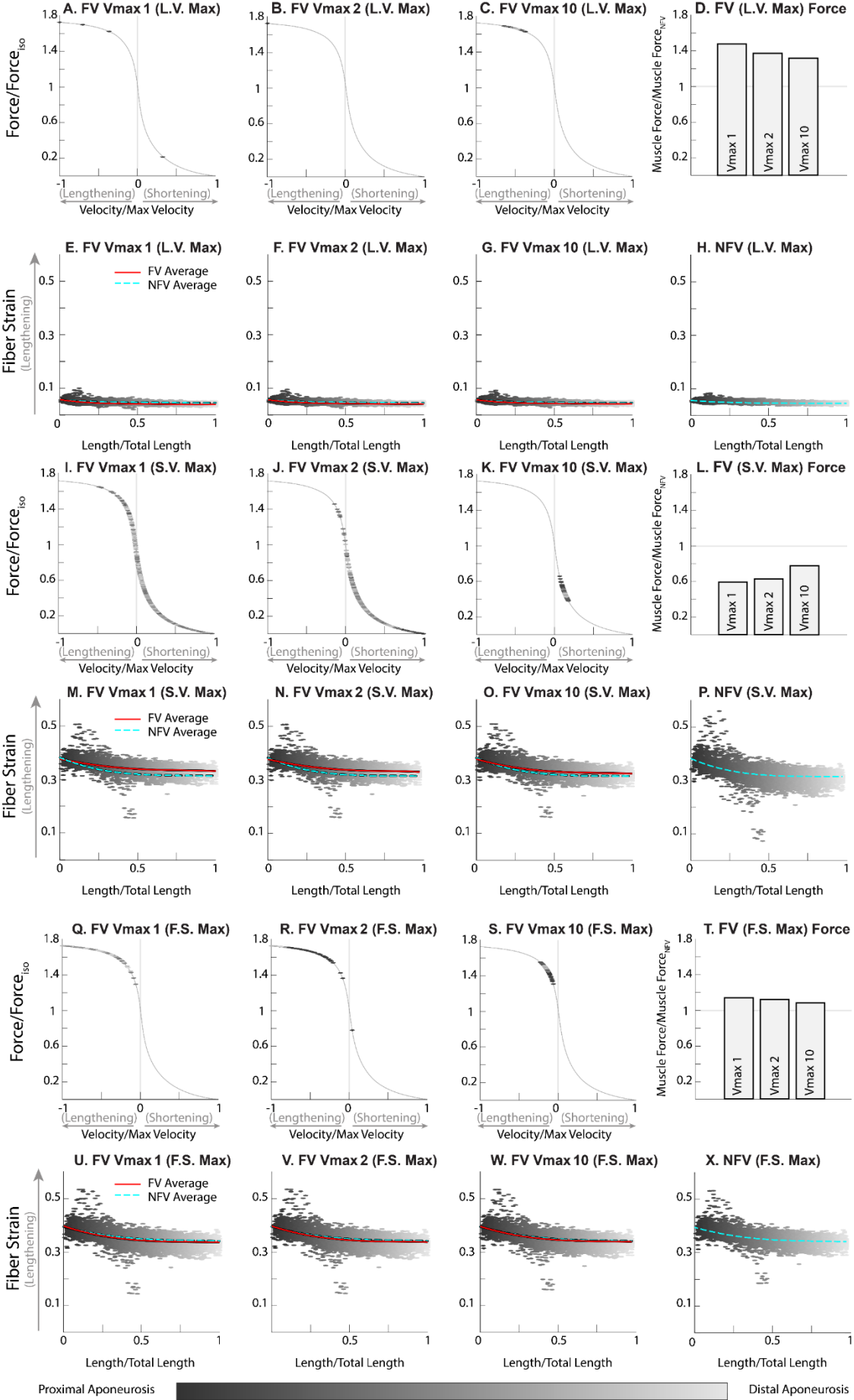


Figure 4.9: Force-velocity distributions, total reaction force, and fiber strains for the 70% speed BFLH models (L.V.: lengthening velocity, S.V.: shortening velocity. F.S.: fiber strain). A-C: Normalized force-velocity distributions for the elements at the time of maximum lengthening velocity. Gray-scale corresponds to the element's position along the length of the model. D: The force at the lengthening velocity max, normalized by the NFV force at that time. E-H: The fiber strain distributions for the lengthening velocity max models (blue dotted line: NFV fiber strain mean, red solid line: model fiber strain mean, points: individual elements). I-K: Normalized force-velocity distributions for the models at the time of the shortening velocity maximum. Gray-scale corresponds to the element's position along the length of the model. L: Force generated by the models at the maximum shortening velocity, compared to the NFV model at the same time. M-P: Fiber Strain distributions of the models at shortening velocity maximum. Q-S: Normalized force-velocity distributions for the models at the time of the fiber strain maximum. Gray-scale corresponds to the element's position along the length of the model. T: Force generated by the models at maximum fiber, compared to the NFV model at the same time. U-X: Fiber Strain distributions of the models at fiber strain maximum.  $V_{max}$  is in fiber lengths/s.

#### 4.5 Discussion

The goals of this paper were to create a muscle constitutive model that incorporates the force-velocity property (the “FV material”) in order to analyze the impact of the force-velocity property strain distributions within muscle tissue. The FV material was validated with both a single element and a multi-element cylindrical model. Two example cases examined if, and under what conditions, the force-velocity property influences strain distributions. In the case of a simplified converging model, notable effects of the FV property were observed: addition of the force-velocity property led to more uniform strains with more of an effect at lower values of  $V_{max}$ . However, in the case of a model of the BFLH muscle simulated with sprinting conditions, there were minimal effects. Taken together, these results illustrate that the force-velocity property has the potential to influence strain distributions, though less pronounced in higher speed situations. Furthermore, we present a new constitutive model that incorporates the force-velocity as a plug-in to FEBio, which we share on simtk.org.

The general effect of the force-velocity relationship is to equilibrate strains, leading to more uniform strain distributions; however, this effect was highly condition dependent. This effect was most pronounced in the FV tapering cross-section models, under isometric conditions, with lower  $V_{max}$  exhibiting more uniform strain than the NFV models. At lower  $V_{max}$ , the fibers are more sensitive to the force-velocity behavior, and thus are more likely to shift

active force above or below isometric values. At higher values of  $V_{\max}$ , the effects of the force-velocity models diminished because the force had a lower sensitivity to changes in fiber velocity. Interestingly, it has been shown that muscles with a higher composition of fast fibers (that express myosin type II) are more susceptible to contraction-induced injury, as compared to muscles with more slow fibers (that express myosin type I) (Garrett et al., 1984; Lieber and Fridén, 1988). Our findings that strain distributions tend to become more uniform for lower  $V_{\max}$  are consistent with this concept and provide potential mechanism for difference in injury susceptibility between fiber types.

The appreciable increase in BFLH fiber strain among effort levels is consistent with previous findings (Chumanov et al., 2011; Fiorentino et al., 2014). The average fiber strain predicted by the models that force-velocity effects diverged slightly from the NFV model, with greater difference occurring in models with lower  $V_{\max}$  values. Additionally, fiber strain was more uniform during shortening conditions as compared to lengthening conditions, for all models. This result indicates that, for values of  $V_{\max}$  that we tested, the magnitude and direction of the muscle-tendon strain impacts strain distributions more than the value of  $V_{\max}$ . Interestingly, at the point of peak musculotendon shortening velocity in the BFLH simulations, the average fiber strain was higher in the FV models as compared to the NFV models, despite a narrowed range of minimum and maximum values. The higher average fiber strains in the FV models are due to the force limit imposed by the shortening portion of the force-velocity curve. Similar to the impact on strain distributions, the impact of including the FV properties the average tissue-level strain depends on the conditions and the muscle architecture.

Other previously developed constitutive models of muscle have included force-velocity properties but differ from the FV material implementation. For example, one modeling approach simulated the impact of mixing fiber with different speed characteristics in a Hill 3-

element model (Marcucci et al., 2017), but with simulations that captured only the shortening portion of the force-velocity curve. Another study developed a constitutive model capturing active force-length, passive force-length, and active force-velocity properties including both the shortening and lengthening regions in a similar hyperbolic implementation (Ehret et al., 2011), but did not include asymptotic boundaries for values beyond  $V_{\max}$  as we did for our FV constitutive model.

It is important to acknowledge the limitations in our implementation of the FV constitutive model. The FV material's calculation determines velocity based on change in fiber stretch over the time step, which introduces potential noise in the calculations, especially for smaller timestep sizes and when there are rapid changes in prescribed boundary conditions or activation. These noise affects may result in extra effort in managing finite element settings to produce a successfully converging model. This effect is most impactful when the  $V_{\max}$  is small, making model elements more likely to experience both rapid and large changes in active fiber force due to only small changes in fiber velocity. Furthermore, the plugin is designed to work in quasi-static simulations (such as the BFLH simulations performed), whereas the experimental observed force-velocity behavior is a dynamic response, in which the muscle mass leads to inertial effects that can alter the muscle-tendon dynamics (Ross et al., 2021; Ross and Wakeling, 2016). Future work can incorporate inertial effects and validate this model in the context of explicit, dynamic finite element simulations.

The results of this paper provided the foundation for understanding how the force-velocity behavior influences the heterogeneity of muscle behavior at the muscle tissue level. We have incorporated and shared FV muscle material as a plugin in FEBio, and the model allows for backwards compatibility on previous FE models (Choi et al., 2015; Knaus et al., 2022; Tran et al., 2022; Westman et al., 2019). The current FV material could easily be expanded to include

more complexities of the dynamic, time dependent muscle behavior, such as including residual force enhancement (Herzog et al., 2006; Rassier and Herzog, 2004) or passive muscle viscoelasticity (Best et al., 1994; Lim et al., 2019; Rehorn et al., 2014); continued improvements in muscle constitutive modeling will allow for incorporation of more recent discoveries in the area of muscle mechanics to be incorporated in muscle models, further expanding applications of muscle modeling in the broad scientific community. The plugin and model files will be available on SimTK.org.

### **Acknowledgements**

We wish to acknowledge NIH grants 5U01AR069393 and 1R01AR078396. We like to thank the FEBio development team for the freely accessible software and documentation manuals. Additionally, we would like to thank Gerard Ateshian and Steve Maas for their valuable assistance on the FEBio Developers Forum.

### **Conflict of Interests Statement**

The authors have no conflicts to report.

## Chapter 5

### A Measurement Based Finite Element Model of Velopharyngeal Closure Including Lateral Wall

#### Activation

Acknowledgements: Silvia S. Blemker, Kazlin N. Mason

*They only say: 'The Doors of Durin, Lord of Moria. Speak, friend, and enter.'*

*- Gandalf the Grey (The Fellowship of the Ring, 1954)*

### **5.1 Abstract**

Different velopharyngeal closure types reflect individuals' unique anatomy and neuromuscular activation patterns. In the case of velopharyngeal dysfunction, a deficiency in anatomy and/or muscle activation prevents effective closure. The lateral pharyngeal wall plays a critical role in helping produce closure, but is often neglected in predictive models where emphasis is entirely on the velum's contact with the posterior wall. To address this gap, we developed a novel finite element model that includes the velum, the levator veli palatini muscle, the superior constrictor muscle, the lateral and posterior pharyngeal wall, and the pharyngeal raphe, using measurements from MRI images taken from 12 participants. Closure simulations were performed and compared with in vivo speech imaging data collected from the same 12 participants performing an /s/ phonation. By using differing combinations of activation of both the lateral wall and levator veli palatini we could provide insight into the relationship between muscle activation and closure patterns.

### **5.2 Introduction**

Velopharyngeal closure is a significant factor influencing the production of speech sounds. Inadequate closure, through anatomical dysfunction, articulatory mislearning, or a combination of both, can result in challenges related to speech, resonance, and overall intelligibility (Kummer, 2011; Woo, 2012). Although speech therapy regimens can often address these issues successfully for many patients (Glade and Deal, 2016; Marsh, 2004), situations involving velopharyngeal insufficiency (VPI) may necessitate surgical intervention, especially in cases of repaired cleft palate (de Blacam et al., 2018; Glade and Deal, 2016).

Prior to surgical interventions, assessment of the velopharyngeal mechanism must occur. These assessments include anatomical mapping and assessment through nasoendoscopy, video fluoroscopy, as well as magnetic imaging; functional assessments through acoustic nasometry are additionally utilized (Lam et al., 2006; Perry et al., 2014; Shprintzen and Marrinan, 2009). On the imaging side, nasoendoscopy provides real-time imaging of velopharyngeal closure, but provides a birds eye view of the VP space, and both fiberoptic distortion and patient compliance can impact visualization (Mason and Black, 2023). Video fluoroscopy, however, can provide views in the lateral, top, and anterior planes for assessment (Dudas et al., 2006; Sullivan et al., 2023), but the best fidelity remains MRI. MRI is the only non-invasive imaging modality that allows for visualization of the velopharyngeal muscles in multiple planes of view. However, MRI is not currently used regularly in clinical practice (Mason, 2024). Typically, qualitative visual assessment of a patient's velopharyngeal anatomy is completed clinically with nasoendoscopy, where contact of the velum with the lateral and posterior pharyngeal wall can be seen during phonation, resulting in a subjective classification of velopharyngeal closure pattern (Jordan et al., 2017; Perry et al., 2018; Shadi et al., 2022).

The primary classifications of velopharyngeal closure patterns are coronal (velum dominant), sagittal (lateral wall dominant), and circular (combined lateral wall and velum activity, potentially with Passavant's ridge (Lin et al., 2019)). Variability in the relative contributions of velopharyngeal structures for differing closure patterns has been reported (Kuehn et al. 1982). Even in cases of coronal patterns, where primary movement occurs in the anterior-posterior direction via movement of the velum, there is still usually some lateral wall movement through activation of the superior pharyngeal constrictor, even if not necessary for full effective closure (Kuehn et al., 1982). Therefore, understanding and evaluating the lateral

wall's significance in active closure remains an essential challenge in developing new investigative and clinically predictive methods.

There has been an increased focus towards coupling computational approaches using finite element modeling to applications for surgical planning, with the goal to provide simulations of velopharyngeal closure in both healthy and dysfunctional anatomy (Inouye et al., 2015; Tran et al., 2022). Finite element (FE) analysis is a computational technique heavily utilized in mechanical engineering that uses definitions of the mechanical behavior of tissues at a continuum level, broken down into geometric subunits called elements, that define a larger problem space defined by the user (Dao and Tho, 2018b). In this manner, researchers can recreate realistic human anatomy from subject measurements, often times directly from MRI segmentations, and study the behavior and response of that anatomy by changing the conditions that the model experiences over time, such as inducing muscle activation of a system and observing that system's response.

To best capture the velopharyngeal mechanism in a FE model, specific anatomical features must be included. In many cases, this has only included the velum, the levator veli palatini (LVP) muscle, and posterior pharyngeal wall as a boundary condition (Tran et al., 2022). However, the lateral pharyngeal wall is a significant contributor to velopharyngeal closure (Kuehn et al., 1982; Perry, 2011; Tran et al., 2022), especially in sagittal and circular closure patterns. Unfortunately, this anatomic contribution has been absent from many prior FE models (Berry et al., 1999; Inouye et al., 2015, 2016, p. 20; Tran et al., 2022). The lateral pharyngeal wall includes several muscles and tissues important for velopharyngeal closure. Most prominently resides the superior pharyngeal constrictor (SPC) (Perry, 2011). This muscle is responsible for contraction of the lateral wall during swallowing as well as speech. It spans from the pterygomandibular raphe (anterior) to the pharyngeal raphe (posterior), wrapping muscle fibers

around the velopharyngeal sphincter which converge upwards into the pharyngeal raphe (Standring, Susan, 2021). Inclusion of the SPC muscle in FE models would increase the fidelity and usefulness of models aimed for clinical applications assessing a patient’s velopharyngeal closure and closure patterns. This requires both an accurate geometry to enclose the pharyngeal region in the model, as well as an active muscle material approach to represent the muscle behavior of the SPC as it contracts in coordination with other VP muscles and structures.

To address these challenges, a novel FE model of the velopharyngeal mechanism was developed to include the lateral pharyngeal wall as an active component of velopharyngeal closure. The model was tested and validated against normative subject-specific MRI data to recreate normal and complete velopharyngeal closure. Unique contributions from individual muscle activations were then employed to identify the impact of differing anatomic contributions from the lateral pharyngeal wall, LVP muscle, and/or velum for achieving velopharyngeal closure.

**5. 3 Materials and Methods**

*Participants*

Twelve participants (6 female; 6 male) between 19 to 33 years of age (Table 5.1) were recruited. Participants were free from craniofacial, velopharyngeal, and musculoskeletal defects. Resonance was confirmed to be within normal limits with nasometry (Nasometer Model 6450).

*Table 5.1: Recruited subject data*

Subject	Sex	Age (years)	Height (m)
1	F	20	1.676

2	F	25	1.702
3	F	20	1.676
4	F	22	1.626
5	F	23	1.626
6	F	23	1.626
7	M	19	1.727
8	M	29	1.905
9	M	31	1.778
10	M	19	1.727
11	M	19	1.803
12	M	33	1.702

Subjects completed a 3D whole-head MRI scan (Siemens MAGNETOM Prisma fit) to capture velopharyngeal anatomy. 3D anatomic scans were T2-weighted with sampling perfection with application optimized contrast using different flip angle evolution (SPACE) in a capture window ranging from 223x223x153.6 mm to 256x256x153.6 mm dependent on subject size. Repetition time (TR) was 2500 ms and echo time (TE) 268 ms, with an average acquisition time of 4 minutes 4 seconds of image capture while subjects remained at rest. Participants additionally completed sustained phonation scans during the production of /s/ (TR 1600 ms, TE 69 ms) to acquire data on velopharyngeal muscle properties in multiple planes of view. Average acquisition time for phonation scans was eight seconds to acquire both midsagittal and oblique coronal images, and 11 seconds to acquire an axial image.

Anatomical measurements on the MR images were completed in 3D Slicer (Fedorov et al., 2012), which allows for image markup, measurements, and 3D segmentation while maintaining anatomic geometry for image aspect ratio, scaling dimensions, and image

resolution. Anatomical measurements (Fig 5.1 & 2) were completed for each individual participant's anatomy at rest and during phonation. Definitions of each measurement are provided in Table 5.2. MR images from participant 12 were additionally utilized as the baseline for the 3D model development, and segmentations of the soft palate (velum), the levator veli palatini (LVP) muscle, and the lateral and posterior pharyngeal walls bordered by the superior pharyngeal constrictor were completed to facilitate development of model geometry.

Segmentations were exported as STL files. Points on the surface boundary of the STL files were then imported into Inventor (Autodesk, Inc., San Francisco, CA), and used to reconstruct the anatomy to the right of the midsagittal plane of the segmented anatomy in a 3D computer-aided design (CAD) format.

*Table 5.2: Description of measurements from MRI imaging.*

Measurement	Plane	Description
LVP major axis (mm)	Midsagittal	Longest linear central distance of LVP cross-section
LVP minor axis (mm)	Midsagittal	Shortest linear central distance of LVP cross-section
Velum-LVP angle (degrees)	Midsagittal	Angle between the LVP minor axis and a straight line from the LVP center to the velum's boundary of the hard palate
Velar length (mm)	Midsagittal	Spline distance of the posterior velum surface from the top of the velum's hard palate boundary to the velum's most inferior point
Velar thickness (mm)	Midsagittal	Linear velum width aligned with the center and orientation of the velum
Effective velar length (mm)	Midsagittal	Linear distance between LVP cross-section center to the velum's border with the hard palate
VP Distance (mm)	Oblique	Linear distance between the posterior surface of the velum and the posterior pharyngeal wall
	Coronal	
Distance between points of origin (mm)	Oblique	Linear distance between the left and right LVP origin sites
	Coronal	
Extravelar LVP length (mm)	Oblique	Spline distance of the LVP length that spans from the surface of the velum to the LVP origin
	Coronal	
Intravelar LVP length (mm)	Oblique	Spline distance of the LVP length that resides within the velum
	Coronal	
VP width - inferior velum (mm)	Axial	Linear distance between the lateral pharyngeal walls at the anterior, middle, and posterior location of the velum as measured from the velum's most inferior point
VP width - superior velum (mm)	Axial	Linear distance between the lateral pharyngeal walls at the anterior, middle, and posterior location of the velum as measured from the velum's most superior point

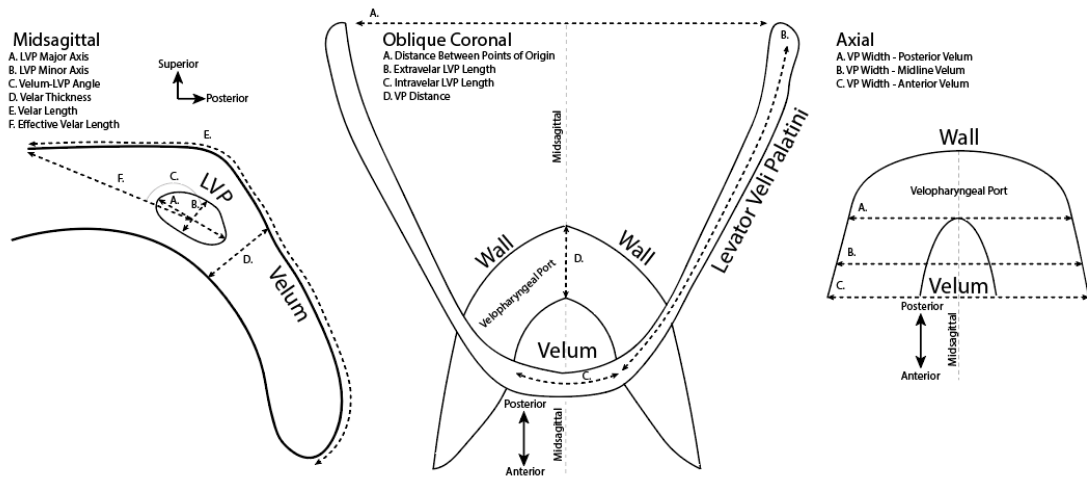


Figure 5.1: Schematic representation of the key MRI measurements. Anatomy is simplified and is not to scale.

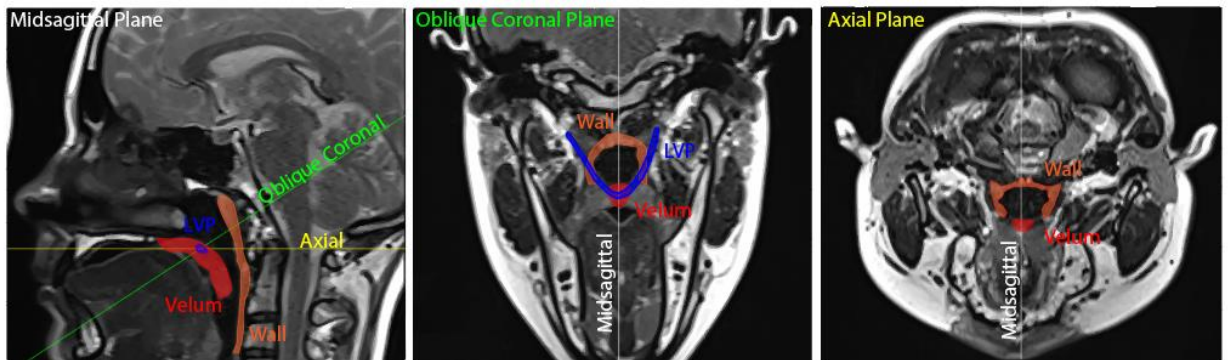


Figure 5.2: Visualization of segmentations obtained for the anatomic region of interest utilized in the 3D FE model.

### Model Geometry and Simulations

The rebuilt geometry was meshed with 4-node tetrahedral elements in Cubit (Coreform, Orem, UT), and imported into the finite element software FEBio Studio (Maas et al., 2012). The model geometry (52150 total elements) consisted of 4 parts: the LVP (16040 elements), the

velum (23171 elements), a combined lateral and posterior pharyngeal wall (12163 elements), and the posterior pharyngeal raphe (776 elements) (Fig. 5.4A). An additional 1 mm wall thickness was added in FEBio Studio on the anterior normal surface of the wall (1281 six node-penta elements) Computational fluid dynamic simulations (Handsfield et al., 2017) generated fiber vectors for the elements of the LVP and pharyngeal wall (partially representing the superior pharyngeal constrictor) to recreate anatomical origin-to-insertion fascicle orientations (Figure 3A). The pharyngeal wall and LVP were assigned as a hybrid material, consisting of a transversely isotropic, nearly incompressible, hyperelastic material that functions as a muscle material (Blemker and Delp, 2005) combined with a Mooney-Rivlin material (Table 5.3). Both the LVP and pharyngeal wall. The velum and raphe parts were both assigned neo-Hookean materials (Table 5.4), but with differing Young’s moduli (E). The material properties were based on previous finite element simulations of velopharyngeal closure (Tran et al., 2022) and measurements of velum stiffness (Birch and Srodon, 2009).

Table 5.3: Material Properties (Levator Veli Palatini and Pharyngeal Wall)

Part	Levator Veli Palatini and Pharyngeal Wall									
Material Name	Muscle Material							Mooney-Rivlin	(Both)	
Parameter	$\sigma_{max}$	$P_1$	$P_2$	$\lambda_{ofl}$	$\lambda_{max}$	$G_1$	$G_2$	$C_1$	$C_2$	k
Value	0.3	0.05	6.6	1	1.4	$5 \times 10^{-4}$	$5 \times 10^{-5}$	0.01	0	10.055
Units	MPa	*	*	*	*	MPa	MPa	MPa	MPa	MPa

Table 5.4: Material Properties (Velum and Pharyngeal Raphe)

Part	Velum		Raphe	
Material Name	neo-Hookean		neo-Hookean	
Parameter	E	v	E	v
Value	5.85 x10 <sup>-4</sup> to 1.41 x10 <sup>-3</sup>	0.45	1.37x10 <sup>4</sup>	0.49
Units	MPa	*	MPa	*

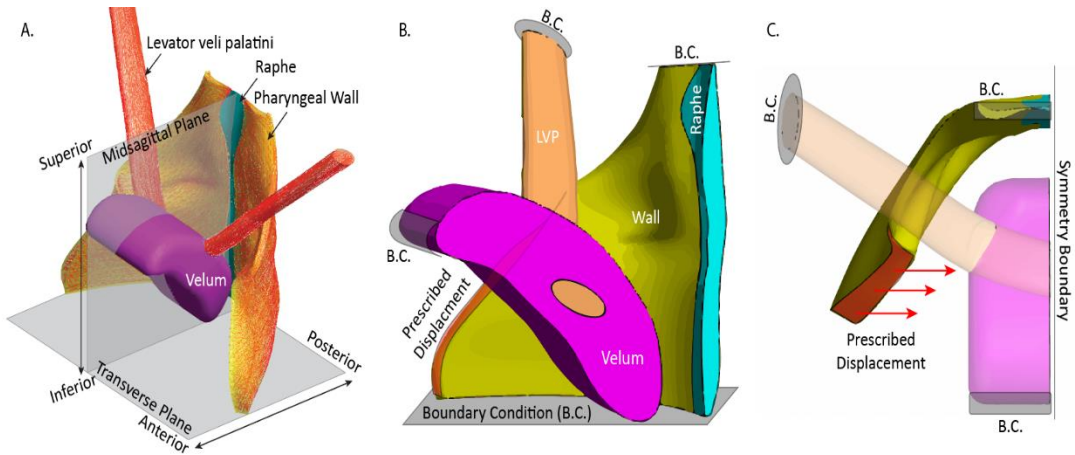


Figure 5.3: The developed FE model. A: A visualization of the model mirrored across the midsagittal plane to show the full physiology. The LVP and pharyngeal wall are defined with a transversely-isotropic, nearly incompressible, hyperelastic material with defined muscle fiber directions that span from muscle origins to insertions (red lines). B: The muscle model showing the superior and inferior boundary conditions on the wall and raphe, the anterior boundary condition on the velum, and the area of prescribed displacement on the pharyngeal wall. C: An axial/transverse view of the model, showing the midsagittal region's symmetry boundary.

Fixed boundary conditions were applied on the inferior and superior side of the pharyngeal wall (and raphe), the anterior side of the velum (where the hard palate connect with the velum), and the superior side of the LVP (the muscle's origin) to allow no movement or rotation (Figure 5.3B). The midsagittal plane, encompassing parts of the raphe, velum, and intravelar LVP were also constrained with a symmetry condition, which fixes those surfaces to

the midsagittal plane but also allows translational and rotational movement within. A portion of the pharyngeal wall (corresponding to the wall's attachment point at the pterygomandibular raphe, Figure 5.3B, 3C) has a unique boundary condition, fixing movement and rotation except for prescribed displacement towards the midsagittal plane. Contact interfaces were defined between the posterior surface of the velum, and the anterior facing surfaces of the wall and raphe, as well as between the LVP and the wall, giving the model contact points to simulate velopharyngeal closure.

Simulations of velopharyngeal closure were performed by ramping the activation of the LVP and wall parts, contracting the muscle material along the direction of the muscle fibers sequentially. First, a 1 mm prescribed displacement of the anterior pharyngeal wall (the pterygomandibular region) was applied. Next, the LVP was stimulated from 0% to 15% or less (simulation dependent) to represent various heights of velum/posterior wall contact. Finally, the muscle material in the pharyngeal wall was activated from 0 to 100% to induce lateral wall motion.

#### *Model Measurements*

To compare the FE model's results with subject MRI data, model geometry was measured using the same benchmarks as the MRI imaging. The FE model was manipulated to project in the appropriate planes for each measurement, which were taken using the software ImageJ (Schneider et al., 2012). The FE model was compared to the averaged measurements at rest, and at phonation, as well as the change in measurements between the averages of rest and phonation.

#### *Model Closure*

To provide a measure of closure for the FE models, the FE models were projected into the transverse plane. The area of the open region directly posterior to the velum at total muscle rest was measured using ImageJ. At time-steps of interest, an overlay of the transverse view of the activated models was placed over the rest model in Illustrator (Adobe, San Jose, CA) (Fig 5.4). By finding the new area of the gap posterior to the velum, a percentage of closure was calculated.

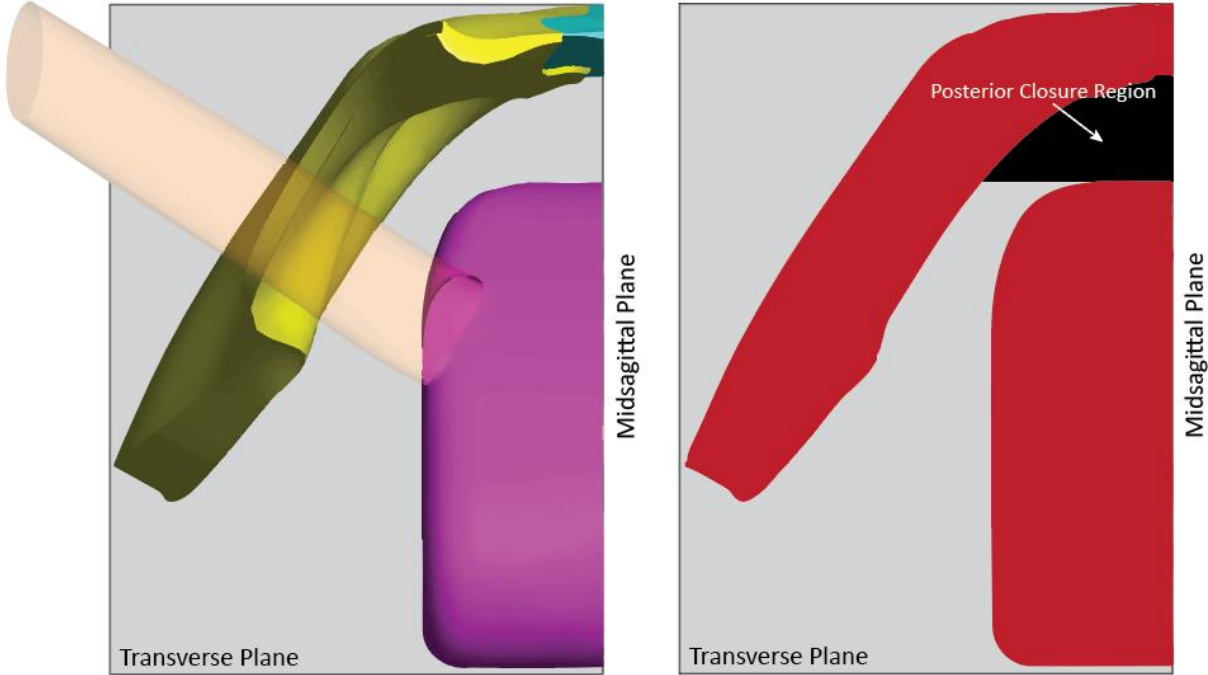


Figure 5.4: An axial/transverse projection of the model geometry was used to measure the gap region directly posterior to the velum.

## 5.4 Results

### *Model Measurements*

The FE model geometry design fit within one  $\sigma$  of the total average measurements, except for effective velar length while at rest (Table 5). At phonation, a candidate model (5% LVP activation, 4.16% wall activation) was found that fit well with the measured average measurements for phonation (10 out of 16 measurements within  $\sigma$ ) and the average difference in measurements from rest to phonation (16 out of 16 measurements within  $\sigma$ , based on differences of average with standard deviations) (Table 5.6, Figure 5.5).

Table 5.5: Average and standard deviation of subject MRI measurements, and the FE model measurement, at rest.

Measurements at Rest		
Feature	Participants (N=12)	FE Model at Rest
LVP major axis (mm)	7.2 ± 3.9	7.8 <sup>a</sup>
LVP minor axis (mm)	2.7 ± 1.2	2.8 <sup>a</sup>
Velum - LVP angle (degrees)	94.5 ± 11.9	94.3 <sup>a</sup>
Velar length(mm)	39.6 ± 4.8	41.6 <sup>a</sup>
Velum thickness (mm)	9.8 ± 3.1	9.3 <sup>a</sup>
Effective velar length (mm)	25.5 ± 5.6	18.1
Dist. between origins (mm)	60.5 ± 8.2	61.6 <sup>a</sup>
VP width inf. velum ant. (mm)	47.1 ± 4.3	51.0 <sup>a</sup>
VP width inf. velum mid. (mm)	44.8 ± 4.0	42.4 <sup>a</sup>
VP width inf. velum pos. (mm)	38.2 ± 4.9	35.6 <sup>a</sup>
VP width sup. velum ant. (mm)	26.5 ± 5.0	31.3 <sup>a</sup>
VP width sup. velum mid. (mm)	26.4 ± 5.2	29.0 <sup>a</sup>
VP width sup. velum pos. (mm)	22.5 ± 5.4	27.7 <sup>a</sup>
VP distance (mm)	15.5 ± 3.3	15.8 <sup>a</sup>
LVP extravelar length (mm)	33.0 ± 3.9	34.8 <sup>a</sup>
LVP intravelar length (mm)	23.4 ± 4.1	22.9 <sup>a</sup>

<sup>a</sup> within measurement range

Table 5.6: Average and standard deviation of subject MRI measurements, and the FE model (5% LVP, 4.16% wall activation), at sustained phonation.

Measurements at Phonation				
Feature	Participants (N=12)	Participants Change	Model	Model Change
LVP major axis (mm)	6.4 ± 2.7	-0.7 ± 4.8	8.0 <sup>a</sup>	0.2 <sup>a</sup>
LVP minor axis (mm)	2.4 ± 1.0	-0.2 ± 1.6	2.7 <sup>a</sup>	-0.1 <sup>a</sup>
Velum - LVP angle (degrees)	123.5 ± 8.7	29.0 ± 14.7	125.2 <sup>a</sup>	30.9 <sup>a</sup>
Velar length(mm)	44.5 ± 3.5	4.9 ± 5.9	52.2	10.6 <sup>a</sup>
Velum thickness (mm)	8.0 ± 2.4	-1.8 ± 3.9	9.7 <sup>a</sup>	0.4 <sup>a</sup>
Effective velar length (mm)	28.5 ± 5.4	3.0 ± 7.8	20.0	1.9 <sup>a</sup>
Dist. between origins (mm)	62.6 ± 7.1	2.1 ± 10.8	61.6 <sup>a</sup>	0.0 <sup>a</sup>
VP width inf. velum ant. (mm)*	48.0 ± 3.8	0.9 ± 5.7	49.0 <sup>a</sup>	-2.0 <sup>a</sup>
VP width inf. velum mid. (mm)*	46.2 ± 4.0	1.4 ± 5.6	38.5	-3.9 <sup>a</sup>
VP width inf. velum pos. (mm)*	37.9 ± 5.6	-0.3 ± 7.4	30.2	-5.4 <sup>a</sup>
VP width sup. velum ant. (mm)*	23.9 ± 3.1	-2.6 ± 5.9	30.4	-0.9 <sup>a</sup>
VP width sup. velum mid. (mm)*	22.7 ± 3.6	-3.6 ± 6.4	30.0	1.0 <sup>a</sup>
VP width sup. velum pos. (mm)*	20.0 ± 5.9	-2.5 ± 8.0	22.7 <sup>a</sup>	-5.0 <sup>a</sup>
VP distance (mm)	4.0 ± 2.9	-11.5 ± 4.4	4.3 <sup>a</sup>	-11.5 <sup>a</sup>
LVP extravelar length (mm)	29.4 ± 3.3	-3.6 ± 5.1	29.0 <sup>a</sup>	-5.9 <sup>a</sup>
LVP intravelar length (mm)	14.7 ± 2.3	-8.8 ± 4.7	13.3 <sup>a</sup>	-9.6 <sup>a</sup>

\* N = 5 for Male

<sup>a</sup> Within measurement range

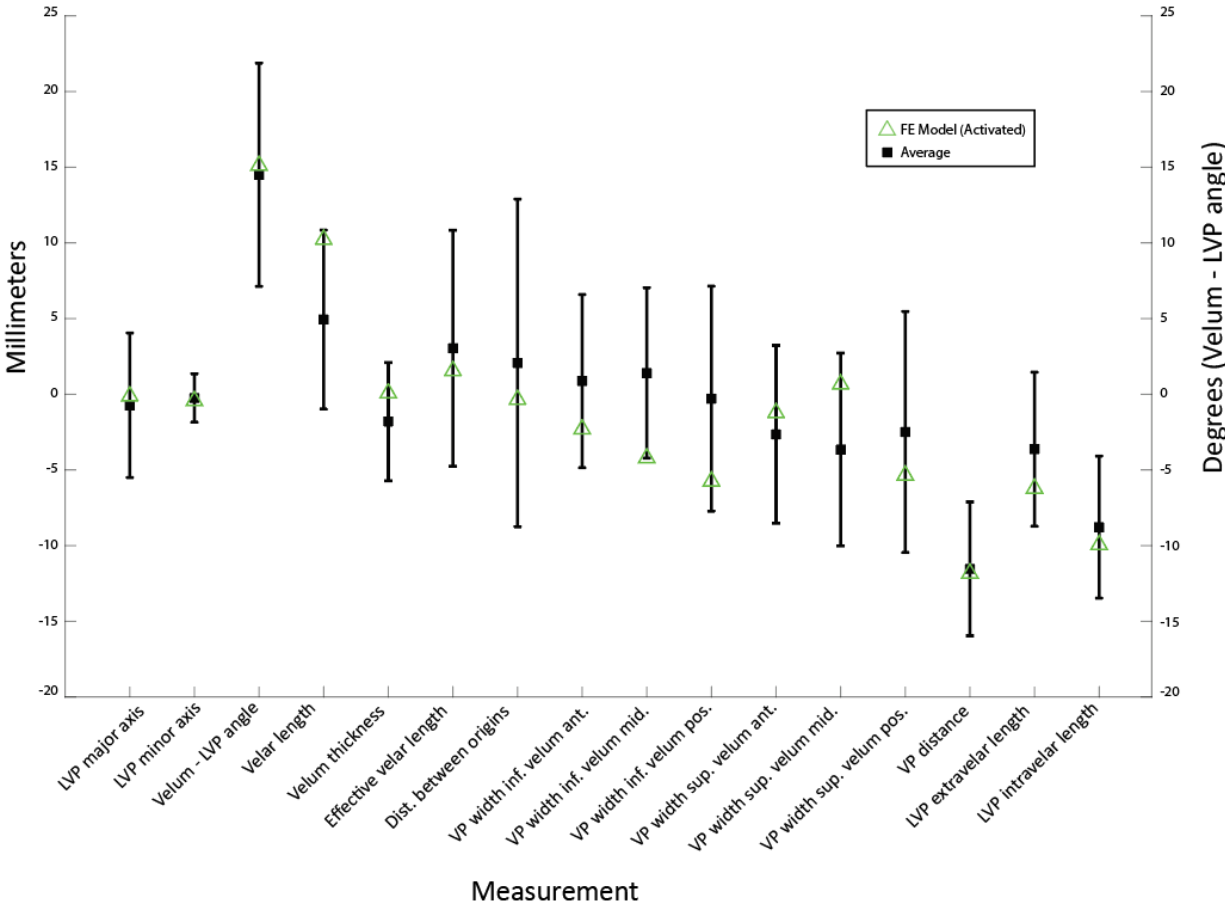


Figure 5.5: The average change (and standard deviation) in measurement criteria from rest to /s/ phonation. Green triangles mark the difference in the FE model between rest and activation.

Model Closure

Increasing LVP activation resulted in greater posterior closure. In low percentage LVP activations, there were points where the addition of lateral wall activation resulted in greater closure (Figure 6). However, at higher LVP activation percentages (>2% activation), this resulted

in no improvement in posterior closure, either declining significantly, or in the 15% case, staying relatively consistent with the initial closure percentage.

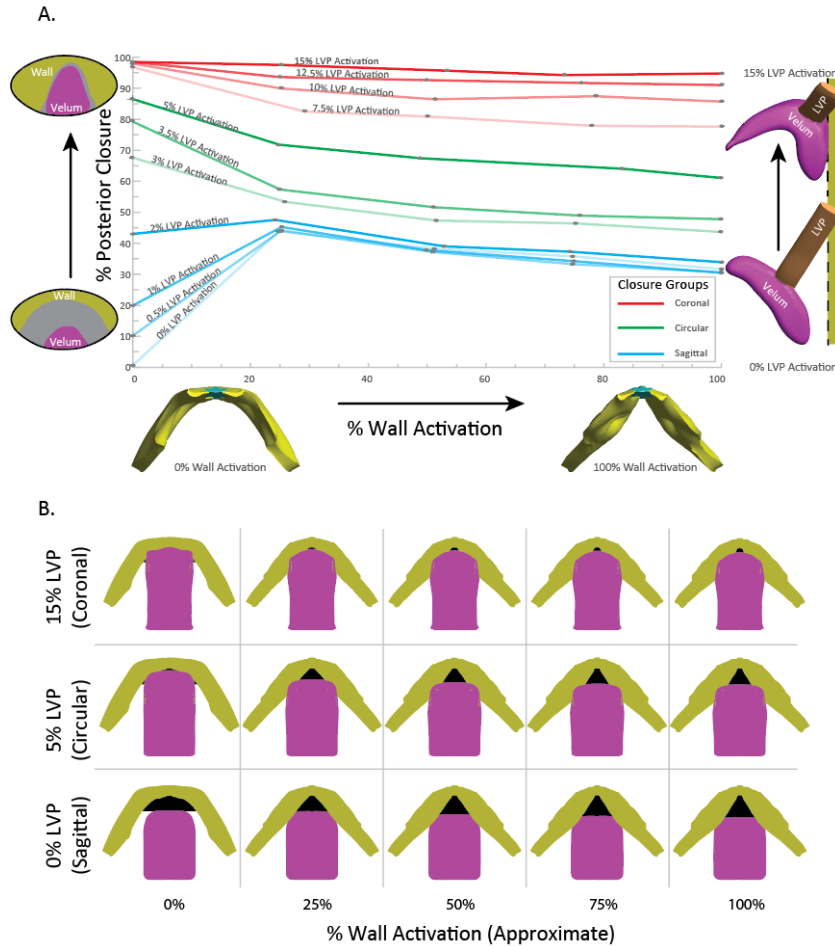


Figure 5.6: A) Plot of wall activation against posterior closure at different LVP activation levels. X-axis is the % wall activation, with two axial/transverse depictions of the wall geometry at 0% activation (left) and 100% activation (right). The Y-axis is the % posterior closure, starting from the percent of LVP activation (from 0 to 15%, right). The value of the LVP activation is the number above each line. The LVP activation dictates the motion and height of the velum as it contacts the pharyngeal wall. % posterior closure was calculated from the amount of non-overlapped space in the current models compared to the model at rest. The colors correspond to the closure pattern grouping: red for coronal (velum dominant), green for circular (combination), and blue for sagittal (wall dominant) B) The transverse views of the 15%, 5, and 0% LVP activations simulations are arranged in a grid based on their relative time points (approximately 0, 25, 50, and 100% wall activation). The black areas in the views are the regions measured closed compared to the open model (0% LVP, 0% wall activation – bottom left) used to calculate the percentage of posterior closure.

## 5.5 Discussion

### *Model Simulations*

The development of the velopharyngeal model to include an active, lateral portion of the pharyngeal wall represents an important advancement in subject specific models of velopharyngeal closure. The lateral wall is known to heavily assist in sagittal and circular closure patterns (Perry, 2011), and at the very least provides form-fitting envelopment for the velum in the coronal pattern. The grouping of models by LVP activation percent into coronal, circular, or sagittal (Fig 5.6) were based on the relative contributions of the LVP for initial closure and the effect of wall activation on that initial percentage. In the sagittal group, increasing LVP activation increased the amount of initial closure, but all models in this group benefited from an amount of lateral wall activation in increasing closure percentages at around 25% wall activation. The coronal groups showed very high closure with just the LVP activation alone, with the 15% activation nearing 100% closure. The coronal groups showed very high closure with just the LVP activation alone, with the 15% LVP activation nearing 100% closure. The circular closure pattern group rests between the coronal and sagittal groups in the amount of initial posterior closure, and remains so throughout wall activation.

Previous models have included limited static lateral wall boundaries in their FE models (Anderson et al., 2019; Srodon et al., 2012) Preliminary models developed by Srodon et al.(2012) additionally only assessed LVP functionality with closure with semi-2D models rather than 3D. Anderson et al.(2019) provided an accurate and complex geometry for the FE modeling of the velopharyngeal anatomy, which included the lateral pharyngeal wall geometry with the superior pharyngeal constrictor muscle among the host of additional muscles making up the pharynx. However, the focus for that work was specific to isolating the effect of only the LVP

and palatoglossus muscle activations and not additional contributions of the superior pharyngeal constrictor muscle and movement of the lateral pharyngeal walls. The range of simulated LVP activation in isolation required for velopharyngeal closure varies throughout different FE models. Anderson et al. (2019) highlights that 30% activation was sufficient to drive closure. Inouye et al. (2016) demonstrated closure at 17% LVP activation (without the musculus uvulae). Tran et al. 2022, demonstrated 14 to 23 % LVP activation was required to achieve closure in patients with velopharyngeal dysfunction, while our model predicted 15% LVP activation for closure. For models that combine lateral wall and LVP activation, a model was found to predict the average change of all measurements from rest to phonation (within one standard deviation) with 5% LVP activation and 4.16% wall activation. It was observed that for models above 2% LVP activation (Figure 6), higher wall activation decreased closure. Additionally, simulations with LVP activations at or lower than 2% were the increased closure from wall activation, maximizing it around 25% wall activation.

EMG studies of the lateral wall, particularly the SPC (Bell, 1976) shows that only a moderate percentage of the SPC muscle's capability is activated during phonation. Our results (Fig 6A) highlight that the lateral wall activation was only beneficial in supporting velopharyngeal closure when the LVP muscle demonstrated low activation percentages (Figure 6A, blue, sagittal closure pattern simulation). This lateral wall activation corresponded to approximately 25% muscle activation necessary to support sagittal closure patterns for normal velopharyngeal function. Increased lateral wall activation, beyond 25%, resulted in variable velopharyngeal closure, either slightly hindering (worsening) or stabilizing the closure percentages. This tracks with the expectation that the lateral wall need not be fully activated to provide adequate velopharyngeal closure, and in some cases may be selectively optimized against velopharyngeal closure depending on the amount of LVP activation that is present.

Previous research by Watterson et al. (2021) has suggested that the traditional categories used to classify velopharyngeal closure patterns may not accurately represent discrete categories of VP closure due to the substantial variability and inconsistency in how closure patterns are clinically rated. The findings of the current study further support this notion, suggesting that various combinations of muscular and soft tissue structures contribute to velopharyngeal closure movements that work in tandem to optimize function necessary to achieve closure. Considering this perspective, along with the quantitative FE model findings, it is plausible that velopharyngeal closure moves along a continuum, with the coronal and sagittal patterns serving as the endpoints with varying degrees of contribution from the soft palate and lateral walls. This would imply that a variety of movements exist between these two classifications, with variations of more circular-like closure patterns/movements along the continuum (Fig 5.6). Findings from the FE model support development of quantitative cutout values to categorize velopharyngeal closure patterns to support more reliable assessments of velopharyngeal closure. The utilization of the FE model provides quantitative data that may assist with classifying movement of the VP port. Continued development of this methodology may support greater accuracy for identifying primary contributors to VP closure and better classify VP closure patterns to support clinical decision making.

#### *Clinical Implications*

Personalized FE models to help with surgical planning are not uncommon in orthopedic context (Aubert et al., 2019; Moncayo-Matute et al., 2022), and have been explored for velopharyngeal insufficiency (Tran et al., 2022), but there remains a challenge to balance the fidelity of a personalized FE modeling approach with time and resources of a clinical team. Overly complex models, recreated one-to-one based on scans of a patient's anatomy are significant investments in manpower and resources, and an overabundance of details may not

be entirely necessary for a particular intervention. The FE model developed in this study aimed to move the ball forward in producing a testable model that is based on average measurements of a few number of important criteria, but simple enough that its dimensions can easily be rescaled to match any particular patient's anatomy at a clinician's discretion, without the need for a fully unique geometry to be built from scratch. The validation of the FE model's ability to predict average changes in measurements from rest to phonation shows that the addition of the lateral pharyngeal wall (with muscle action resembling the SPC) is a beneficial improvement in the development of a generalized velopharyngeal model, especially considering the permutations of potential closure patterns involving the lateral wall. Findings also contribute to novel insights related to the relative contributions of structures necessary for achieving velopharyngeal closure, which may have implications for improving qualitative clinical assessments and reduce subjectivity from ratings of velopharyngeal closure patterns (Watterson et al., 2020). The anatomic and quantitative insights obtained from this FE model, provides a foundation to support development of future patient-specific models and identify areas of anatomic need for children with velopharyngeal dysfunction.

#### *Limitations of study*

The decrease in posterior closure percentage with higher lateral wall activation may be the result of several factors. In our model, high wall activation resulted in pressure in the posterior velum, which resulted in anterior displacement. This displacement appears to increase the amount of open space posterior to the velum. Physiologically, however, the effective closure of the velopharyngeal sphincter may be less sensitive to this pressure, either through activation of the musculus uvulae (MU) to extend the velum into posterior contact (Boorman and Sommerlad, 1985; Inouye et al., 2015; Perry, 2011), or a layer of soft tissue wrapping around the

superior pharyngeal constrictor that is more amenable to deformation, making it more likely to seal around the velum in contact. This study did not incorporate measurements or modeling of the MU, but future models can apply the current framework with a MU implementation for greater fidelity. Additionally, the action of several other muscles (such as the tensor veli palatini and several interconnected muscle groups located along the lateral wall) were not included in the model. Adding these muscles would increase both measurement and FE model complexity, but may influence the final simulation results. However, with the current FE model, the ability to match participant measurements appears strongly feasible with the current muscle modeling approach of the LVP and pharyngeal wall. Additional research on the scope of what must be included in FE models of velopharyngeal closure would do well to help to further bolster the potential clinical applications of this kind of velopharyngeal modeling.

Additionally, the subjects studied were all of adult age. There is strong evidence that the comparative scaling of the velopharyngeal landmarks change during aging (Haenssler et al., 2020; Mason et al., 2016), such that children will have different velopharyngeal function than adults. While we expect that this FE modeling approach could be used in the future for all ages using patient-specific measurements for clinical applications, further investigation on the model's predictive accuracy with children will be an excellent future step. A greater number of participants and additional incorporation of participants across the age span may provide more generalizable results.

## **Conclusion**

This FE model is the first to include the properties and contributions of the lateral pharyngeal walls and SPC muscle necessary for achieving VP closure. Now validated, this method can be used to build robust, patient-specific models for individuals with repaired cleft

palate and/or velopharyngeal insufficiency. It is particularly optimized for understanding relative anatomic contributions necessary to achieve velopharyngeal closure. Model results support improved understanding of velopharyngeal biomechanics and may aid in future clinical/surgical decision making.

### **Acknowledgements**

The authors would like to acknowledge the expertise and skill of the iCO Lab research team members, who have contributed invaluable to the subject measurements and MRI segmentations that lead to the development of this model. We would additionally like to thank Dr. Vi Tran, whose previous experience in velopharyngeal modeling was of great assistance in the early stages of this project. Finally, we would like to thank the UVA MRI radiology and medical imaging research staff for their help in obtaining subject data.

### **Funding**

This work was supported in part by the National Center for Advancing Translational Sciences of the National Institutes of Health under Award Numbers KL2TR003016/UL1TR003015. The authors also gratefully acknowledge the support from the University of Virginia Center for Engineering in Medicine and the Hartwell Foundation. The content is solely the responsibility of the authors and does not necessarily represent the official views of the National Institutes of Health.

## Chapter 6

### Conclusions

*Where we go from there is a choice I leave to you.*

- Neo (*The Matrix*, 1999)

## 6.1 Summary

In this dissertation, we have developed three different FE modeling frameworks for investigating clinically relevant questions.

In [Chapter 3](#), we built a battery of 78 injury models to look at the implication of location and form of a muscle, and found a VML injury's disruption of a cross-section parallel to the anatomical cross-sectional plane is more likely to predict force-loss than the volume of the injury itself. We also found that injuries which overlaps the position of the distal aponeurosis are less likely to diminish the muscle's force production, whereas injuries closer to the proximal tendon are the most efficient at causing force-loss per volume of muscle damaged. We additionally showed that we were able to predict the force-loss using a model of a similar injury to those experienced by rats in a commonly used VML surgery, lending support to the predictions made for the other injury models testing other combinations of shapes and locations.

In [Chapter 4](#), we designed a modified constitutive model of muscle that allowed for force-velocity behavior in quasi-static simulations as a plugin for the free finite element software package FEBio. We validated the constitutive model's behavior through a series of experiments including single element models and multi-element cylindrical meshes. We then applied the model in a tapering cross-section to look maximum fiber velocities during isometric and eccentric activations. Finally, we used a previously developed model of the biceps femoris long head muscle during sprinting to study the impact the force-velocity material might have on fiber strain. We found that fiber strain distributions were indeed influenced by maximum fiber velocities, and that change was dependent on the width of our force-velocity curves by modulating  $V_{max}$ , as well the presence of and speed of any applied displacements.

In Chapter 5, we built a model of velopharyngeal closure that was novel in the use of the lateral pharyngeal wall as an active participant. We build a model consisting of the levator veli palatini, the velum, the posterior and lateral pharyngeal walls, and pharyngeal raphe. The fiber orientation of the lateral and posterior walls allows them to act as the superior pharyngeal constrictor, driving inwards towards the velum during activation. Our new model was able to predict the change in average measures (within one standard deviation) for all of our 16 of our measurement criteria. Additionally, we were able to use the model with different combinations of levator and wall activation, to observe the combinations of activations necessary to recreate the three main types of velopharyngeal closure, (coronal, sagittal, and circular).

## **6.2 Contributions**

In this dissertation, there are several new contributions, including the creation of new methods to model muscle with finite elements, and through those methods, new discoveries about the form and function of muscle. Summarized here are important developments that resulted from the work in Chapters 3, 4, and 5.

### **A method to test VML injury in complex muscles**

Previous studies have coupled finite element modeling with the volume removal associated with VML (Passipieri et al., 2019; Westman et al., 2019), but to my knowledge any attempts of modeling in a model of complex pennation, such as the tibialis anterior, have not been attempted. This may be due to the increasing complexity of meshes required to accurately capture a muscle behavior. Developing the process of building and testing the Rat TA VML models efficiently required a significant amount of trial-and-error. The bottleneck of this process that needed to be overcome was the meshing process itself. In order to sufficiently test a neatly defined volume being removed from the muscle, one could attempt to delete groups of

elements from a uniformly distributed mesh. However, unless a mesh is unusually fine, this can become challenging and time-consuming, and often leaves much to desired as injury edges are often not smooth, but instead jagged collections of elements. Even a particularly fine mesh doesn't guarantee this method will be successful, and you take on additional computational time per model with more elements. The second method, which is the one that I ended up using in Chapter 3, is defining the boundary of injury locations before meshing. Using a negative of the VML injury (a shape of set dimensions), I maneuvered the injury into position used Boolean intersections to automatically generate smooth VML boundaries. This result in nodes that will be distributed on an injury's boundary faces when meshed, even in the muscle's internal volume. Furthermore, inducing an injury becomes a matter of removing those elements as a group (through editing the FE definition document). A pleasant side effect of this approach is that you can define multiple boundaries per model, combine them in a single mesh, and iterate on which element groups are removed at a single time, which I heavily took advantage of to generate a large number of unique models. Although relatively simplistic in execution, I believe this method has merit in future studies of VML, particularly in understanding how any individual muscle's ability to produce force is changed by an injury by identifying key areas of muscle geometry that are at risk for generating greater force-loss, or areas that are more resilient.

### **New insight into the complex relationship between VML injury and force loss in the rat TA**

The results of the modeling experiments in Chapter 3 showed a marked increase in correlation between cross-sectional area loss and force-loss, compared to the equivalent comparison of volume-loss and force-loss. This indicates that the percent volume or percent mass metric commonly used in many experiments for defining a VML injury is not necessarily the best indicator of muscle force-loss. Additionally, the injuries that disrupted cross-sectional area closest to the converging fibers near the proximal aponeurosis were more volume efficient in

driving force-loss than elsewhere in the TA model, while injuries near the internal distal aponeurosis had the worst efficiency. These observations can likely be translated to human muscle, as the human TA also has an internal distal aponeurosis, and could possibly be used to predict force-loss in human muscles, even on a subject-specific basis.

### **A new constitutive muscle model with force-velocity behavior available in an open-source plugin**

The plugin developed for Chapter 4 has use for researchers interested in force-velocity implications in their own muscle simulations. It is based on the open-source FEBio platform, and is free to share, use, and modify for anyone, maximizing potential impact. Additionally, by basing the plugin on a previous and well-used muscle constitutive model (Blemker et al., 2005), there is a built-in level of understanding and familiarity for many modelers, and could even help facilitate backwards compatibility with older FE muscle models.

### **Implications about the need for force-velocity in models**

We tested a variety of scenarios in Chapter 4 with the force-velocity material, and found there are indeed cases in which introducing a FV material could have substantial impact on how a muscle behaves, particularly in force-generation and fiber strain. With lower  $V_{\max}$  values, fiber strain can deviate more and more from a model without force-velocity behavior. We additionally discovered that the force-velocity behavior may narrow the range of fiber strain throughout a muscle. I believe the results in Chapter 4 shows that there is a compelling argument for including force-velocity behavior in muscle models, or at least should serve as a reminder that researchers should consider the potential implications of the effects when they design their own FE experiments.

### **A method for incorporating the lateral wall in soft palate simulations**

In Chapter 5, we built a model of the velopharyngeal wall that included the levator veli palatini muscle, as well as the lateral pharyngeal wall as an active contributor to closure, particularly by modeling the action of the superior pharyngeal constrictor muscle. To our knowledge, there have been no attempts to build a 3D FE model that includes the muscular contributions from the lateral wall. We additionally validated the model to show that it can predict differences between rest and phonation, and that it can reveal combinations of muscle activation that can cause certain closure patterns. Both of which hint towards this modeling approach's usefulness as a future tool for clinicians to look at individual anatomy and investigate the outcomes of different interventions.

### **6.3 Future Directions**

#### **Using mechanics to build the next generation of regenerative therapies**

The modeling approach used in Chapter 3 to build and test VML injuries in the rat TA could easily be adapted to any skeletal muscle. It could very well be manageable for future modeling projects in which groups of muscles are combined in a single FE experiment together, with variations of injuries distributed across the various muscles, to better represent the complex trauma that occurs in high-energy trauma. The insights in the TA model also show that not every part of the muscle is created equal in terms of force-generation. One might imagine a potential therapeutic to target the most important regions of the muscle to rehabilitate force-generation in cases where repairing the entirety of a VML might be unfeasible. Perhaps there could be a scenario in which subject-specific finite element models of a patient's muscle are made using MRI images of the injured muscle, and if they have an intact lateral version of that muscle, use the negative of the VML injury with the model of the intact muscle in the same manner we did with our TA models. Similar to our FE experiment, they could predict the force loss in regions of

the muscle by isolating parts of the VML injury in sub-sections, in order to decide of which regions would be the most efficient to repair.

Additionally, with the ability to represent the mechanical state of the rat TA through the use of our model (intact or otherwise), researchers can tailor the force-loss they want for their regenerative experiments by designing and testing different injury shapes and locations. They might also tailor the designs of the implants or biomaterials in response to stresses, strains, and shears that could be detected in the FE model of a VML injury that might otherwise be difficult or impossible to measure.

#### **Advanced constitutive modeling to include different fiber types and motor recruitment**

The implementation of the force-velocity behavior adds additional options for detail in FE muscle simulations. The success of the plugin developed in Chapter 4 shows it might be a basis for additional development; it could very easily be expanded to capture even greater muscle behavioral fidelity, and would definitely be worthy of some investigation. The different fiber types (oxidative, glycolytic, and hybrid forms) all exhibit different force-velocity profiles (Bottinelli et al., 1996), but are unequally distributed throughout a muscle. By developing a vector-field based approach to distributing fiber types markers within a FE model, interpolating the distribution of the field at each node, then assigning force-velocity parameters unique to each fiber type, one could generate a unique FE model that handles fiber heterogeneity. As an extension to that, one could also imagine a system in which fiber-recruitment is handled based on fiber types, in which activation order is assigned based on each element's interpolation of the fiber-type field. While such extra detail may not be necessary for many FE simulation goals, the ability to put all these features in a plugin format allows for researchers to make that choice for themselves with no hassle.

### **Using lateral wall simulations to predict surgical outcomes**

The validation of the lateral wall velopharyngeal closure model we developed bodes well for the potential use of the same type of model being used on a subject-specific basis. Additional research will likely need to be done in order to see if our approach works on subject-to-subject predications rather than the averaged measurement approach we used. But if that is successful, the same kind of surgical predictive experimental modeling done with the posterior wall (Tran et al., 2022) could be expanded. In designing their strategies for achieving closure, surgeons can now consider the potential for the lateral walls to act with their augmentations. For example, they may decide it is not necessary to perform a large flap transfer from the posterior wall into the velum, if they can model and simulate that a smaller, thinner transfer will work well with a patient's lateral wall anatomy and behavior. The ability to now capture the behavior of closure in both dimensions of a closure pattern (anterior-posterior and lateral-medial) can potentially give clinicians a powerful tool in patient care.

### **6.4 Final Thoughts**

Research can be unpredictable. When developing the research plan for this dissertation, there were several exciting developments that arose, resulting in the opportunity to different address muscle-related clinical problems. While varying in topic matter, there was a clear approach for each question that allowed the leveraging of an FE-based approach. Expertise and methodology developed for use each project reinforced each other, even if as different experimental questions began to take shape. Knowledge and skills for building a large number of injured muscles in FEBio for Chapter 3 was applied in designing the force-velocity material in Chapter 4. Likewise, the skill to build effective anatomical models from MRI and other measurements in Chapter 3 also aided the velopharyngeal model in Chapter 5, which required a new approach in

imaging and muscle geometry. Furthermore, internal tools and methodology designed for Chapter 4 became incredibly useful in the analysis of data in Chapter 3 and 5, whereas the approach of Chapter 5 also influenced how the other two chapters.

In conclusion, if the chapters of this dissertation could be reduced to a single common thread, it would likely be that muscle is deceptively complex. Despite prediction of muscle behavior from knowledge about full range of its structural hierarchy, the culmination of all those little relationships in a whole muscle often manifests in unexpected ways. During the period of my research, FE models often acted unpredictably. The most interesting discoveries were made while investigating out *why* these models broke from expectation. FE modeling's ability to build these experiments that can have surprising results is a core reason why it is a powerful research tool. The applications of FE modeling with muscle are incredibly numerous, alongside the huge variety of skeletal muscle forms and functions within humans. There are over 600 skeletal muscles in the human body, each with their own geometries and characteristics. And among humans, accounting for the unique anatomies of each individual in a population of over 8 billion results in a startlingly large number of over 4.8 trillion unique skeletal muscles currently on Earth. With such variety, FE modeling is a logical tool to help researchers close the gaps in muscle clinical research and gain the understanding to better address human health challenges, learning more about muscle one simulation at a time.

## Chapter 7: Appendix

## Chapter 3

Table 7.1 is the complete set of data taken from all intact and VML models.

Table 7.1: Complete results of all models.

Model	Description	Volume (mm <sup>3</sup> )	Force (N)	% Volume Loss	% Force Loss	% Force Loss / % Volume Loss	% Maximum CSA Loss	Aponeurosis Length Below Injury (mm)	% of Injury Length Above Aponeurosis
Intact	No VML in mesh, used for optimization	418.90	5.58	0.00	0.00	N/A	0.00	0.00	N/A
Intact A	10x5 mm template (centered)	418.90	5.54	0.00	0.00	N/A	0.00	0.00	N/A
Intact B	10x5 mm template (proximal, distal)	418.90	5.44	0.00	0.00	N/A	0.00	0.00	N/A
Intact C	10x5 mm template (rounded, centered)	418.90	5.63	0.00	0.00	N/A	0.00	0.00	N/A
Intact D	10x5x3 mm template (rounded, fit maximize)	418.90	5.51	0.00	0.00	N/A	0.00	0.00	N/A
Intact E	6 mm biopsy punch template	418.90	5.60	0.00	0.00	N/A	0.00	0.00	N/A
Intact F	1 mm strip template (axial)	418.90	5.64	0.00	0.00	N/A	0.00	0.00	N/A
Intact G	1 mm strip template (longitudinal)	418.90	5.57	0.00	0.00	N/A	0.00	0.00	N/A
Intact H	Multicut 5 mm width template	418.90	5.62	0.00	0.00	N/A	0.00	0.00	N/A
Intact I	Multicut 1 mm strip template	418.90	5.51	0.00	0.00	N/A	0.00	0.00	N/A
A1	10x5 mm (centered)	343.27	4.86	18.05	12.27	0.68	16.78	1.68	16.78
B1	10x5 mm (proximal)	336.30	3.91	19.72	28.08	1.42	51.00	0.00	0.00
B2	10x5 mm (distal)	337.46	5.05	19.44	7.17	0.37	56.80	7.39	73.90
C1	10x5 mm (rounded, centered)	335.06	4.44	20.01	21.14	1.06	45.47	0.00	0.00
D1	10x5x3 mm (rounded, fit maximize)	291.61	2.66	30.39	51.72	1.70	75.01	0.00	0.00
E1	6 mm biopsy punch (distal)	371.29	5.36	11.37	4.15	0.36	56.90	5.54	92.31
E2	6 mm biopsy punch (proximal)	395.02	5.06	5.70	9.56	1.68	35.80	0.00	0.00
E3	6 mm biopsy punch (centered)	362.84	4.95	13.38	11.55	0.86	51.10	0.00	0.00
E4	6 mm biopsy punch (centered, through)	316.11	2.04	24.54	63.57	2.59	91.80	0.00	0.00
E5	6 mm biopsy punch (centered, E4 minus E3)	372.17	4.88	11.16	12.85	1.15	40.70	0.00	0.00
F1	1 mm strip (width of muscle, distal)	412.39	5.61	1.55	0.50	0.32	42.00	1.00	100.00
F2	1 mm strip (width of muscle, proximal)	414.38	5.51	1.08	2.22	2.05	29.90	0.00	0.00
F3	1 mm strip (width of muscle, centered)	408.16	5.51	2.57	2.20	0.86	47.60	0.00	0.00
G1	1 mm x 10 mm strip (centered, longitudinal)	395.81	5.35	5.51	3.95	0.72	12.50	0.00	0.00

H 1	Section 1	398.25	5.07	4.93	9.70	1.97	46.87	0.00	0.00
H 1 2	Section 1 through 2	386.93	4.87	7.63	13.37	1.75	46.87	0.00	0.00
H 1 3	Section 1 through 3	373.36	4.67	10.87	16.79	1.54	46.87	0.00	0.00
H 1 4	Section 1 through 4	352.77	4.47	15.79	20.46	1.30	46.87	0.00	0.00
H 1 5	Section 1 through 5	334.99	4.36	20.03	22.36	1.12	46.87	0.00	0.00
H 1 6	Section 1 through 6	324.59	4.29	22.51	23.61	1.05	46.87	0.49	4.16
H 1 7	Section 1 through 7	308.73	4.24	26.30	24.50	0.93	47.56	2.32	17.15
H 1 8	Section 1 through 8	292.38	4.19	30.20	25.37	0.84	47.56	4.46	28.47
H 2	Section 2	407.58	5.40	2.70	3.83	1.42	45.40	0.00	0.00
H 2 3	Section 2 through 3	394.01	5.22	5.94	7.07	1.19	45.40	0.00	0.00
H 2 4	Section 2 through 4	373.42	4.99	10.86	11.20	1.03	45.40	0.00	0.00
H 2 5	Section 2 through 5	355.64	4.81	15.10	14.32	0.95	45.40	0.00	0.00
H 2 6	Section 2 through 6	345.24	4.73	17.58	15.78	0.90	46.31	0.49	6.04
H 2 7	Section 2 through 7	329.38	4.66	21.37	16.99	0.79	47.56	2.32	23.46
H 2 8	Section 2 through 8	313.03	4.62	25.27	17.79	0.70	47.56	4.46	37.07
H 3	Section 3	405.33	5.43	3.24	3.33	1.03	43.63	0.00	0.00
H 3 4	Section 3 through 4	384.74	5.21	8.15	7.23	0.89	43.97	0.00	0.00
H 3 5	Section 3 through 5	366.96	5.04	12.40	10.20	0.82	43.97	0.00	0.00
H 3 6	Section 3 through 6	356.56	4.96	14.88	11.75	0.79	46.31	0.49	7.35
H 3 7	Section 3 through 7	340.70	4.89	18.67	13.02	0.70	47.56	2.32	27.44
H 3 8	Section 3 through 8	324.35	4.87	22.57	13.23	0.59	47.56	4.46	42.09
H 4	Section 4	398.31	5.41	4.92	3.76	0.76	43.97	0.00	0.00
H 4 5	Section 4 through 5	380.53	5.25	9.16	6.50	0.71	43.97	0.00	0.00
H 4 6	Section 4 through 6	370.13	5.16	11.64	8.05	0.69	46.31	0.49	9.55
H 4 7	Section 4 through 7	354.27	5.09	15.43	9.40	0.61	47.56	2.32	33.50
H 4 8	Section 4 through 8	337.92	5.04	19.33	10.29	0.53	47.56	4.46	49.19
H 5	Section 5	401.12	5.48	4.24	2.51	0.59	43.49	0.00	0.00
H 5 6	Section 5 through 6	390.72	5.40	6.73	3.85	0.57	46.31	0.49	16.40
H 5 7	Section 5 through 7	374.86	5.33	10.51	5.13	0.49	47.56	2.32	48.33
H 5 8	Section 5 through 8	358.51	5.28	14.42	5.97	0.41	47.56	4.46	64.26
H 6	Section 6	408.50	5.55	2.48	1.21	0.49	46.31	0.49	42.82
H 6 7	Section 6 through 7	392.64	5.48	6.27	2.37	0.38	47.56	2.32	78.13
H 6 8	Section 6 through 8	376.29	5.44	10.17	3.19	0.31	47.56	4.46	87.29
H 7	Section 7	403.04	5.54	3.79	1.32	0.35	47.56	1.84	100.00
H 7 8	Section 7 through 8	386.69	5.49	7.69	2.19	0.28	47.56	3.98	100.00
H 8	Section 8	402.55	5.55	3.90	1.19	0.31	38.40	2.14	100.00
I 1	Section 1	414.98	5.48	0.94	0.54	0.58	16.65	0.00	0.00
I 1 2	Section 1 through 2	411.87	5.43	1.68	1.47	0.88	39.53	0.00	0.00
I 1 3	Section 1 through 3	406.36	5.31	2.99	3.58	1.19	63.13	0.00	0.00
I 1 4	Section 1 through 4	403.20	5.01	3.75	9.02	2.41	76.77	0.00	0.00
I 1 5	Section 1 through 5	400.51	4.26	4.39	22.76	5.18	88.50	0.00	0.00
I 1 6	Section 1 through 6	399.14	2.48	4.72	54.95	11.65	94.48	0.00	0.00
I 1 7	Section 1 through 7	398.04	1.06	4.98	80.85	16.24	99.11	0.00	0.00
I 2	Section 2	415.79	5.48	0.74	0.54	0.73	22.88	0.00	0.00
I 2 3	Section 2 through 3	410.28	5.43	2.06	1.40	0.68	46.49	0.00	0.00
I 2 4	Section 2 through 4	407.12	5.38	2.81	2.36	0.84	60.12	0.00	0.00
I 2 5	Section 2 through 5	404.43	5.31	3.45	3.65	1.06	71.86	0.00	0.00
I 2 6	Section 2 through 6	403.06	5.21	3.78	5.52	1.46	77.84	0.00	0.00
I 2 7	Section 2 through 7	401.96	4.86	4.04	11.87	2.94	82.46	0.00	0.00

I 3	Section 3	413.39	5.48	1.31	0.62	0.47	23.61	0.00	0.00
I 3 4	Section 3 through 4	410.23	5.45	2.07	1.07	0.52	37.24	0.00	0.00
I 3 5	Section 3 through 5	407.54	5.42	2.71	1.69	0.62	48.98	0.00	0.00
I 3 6	Section 3 through 6	406.17	5.38	3.04	2.36	0.78	54.96	0.00	0.00
I 3 7	Section 3 through 7	405.07	5.26	3.30	4.48	1.36	59.58	0.00	0.00
I 4	Section 4	415.74	5.49	0.75	0.34	0.46	13.63	0.00	0.00
I 4 5	Section 4 through 5	413.05	5.47	1.40	0.74	0.53	25.37	0.00	0.00
I 4 6	Section 4 through 6	411.68	5.45	1.72	1.09	0.63	31.35	0.00	0.00
I 4 7	Section 4 through 7	410.58	5.41	1.99	1.87	0.94	35.98	0.00	0.00
I 5	Section 5	416.21	5.49	0.64	0.31	0.48	11.73	0.00	0.00
I 5 6	Section 5 through 6	414.84	5.48	0.97	0.54	0.56	17.72	0.00	0.00
I 5 7	Section 5 through 7	413.74	5.46	1.23	1.00	0.81	22.34	0.00	0.00
I 6	Section 6	417.53	5.50	0.33	0.15	0.44	5.98	0.00	0.00
I 6 7	Section 6 through 7	416.43	5.49	0.59	0.33	0.55	10.61	0.00	0.00
I 7	Section 7	417.80	5.50	0.26	0.13	0.48	4.63	0.00	0.00

## Chapter 4

An additional interesting behavior was found with the FV material, but could not be included in the original manuscript that Chapter 4 was based off of, due to figure limits in the original journal submission. The average strain in the tapering cross-section model, under isometric conditions, underwent exponential decay relative to  $V_{\max}$  (Fig 4.10). The range of strain also appears to be attenuated with  $V_{\max}$ , with the lower FV models having a narrower range of strain, with a higher total mean, until eventual convergence with the NFV model. It appears that fibers with low  $V_{\max}$  values limit the rate at which connecting fibers can shorten (otherwise there would be no force to balance the quasi-static simulation for those fibers shortening faster than  $V_{\max}$ ). This behavior is briefly commented on in the discussion section of this chapter.

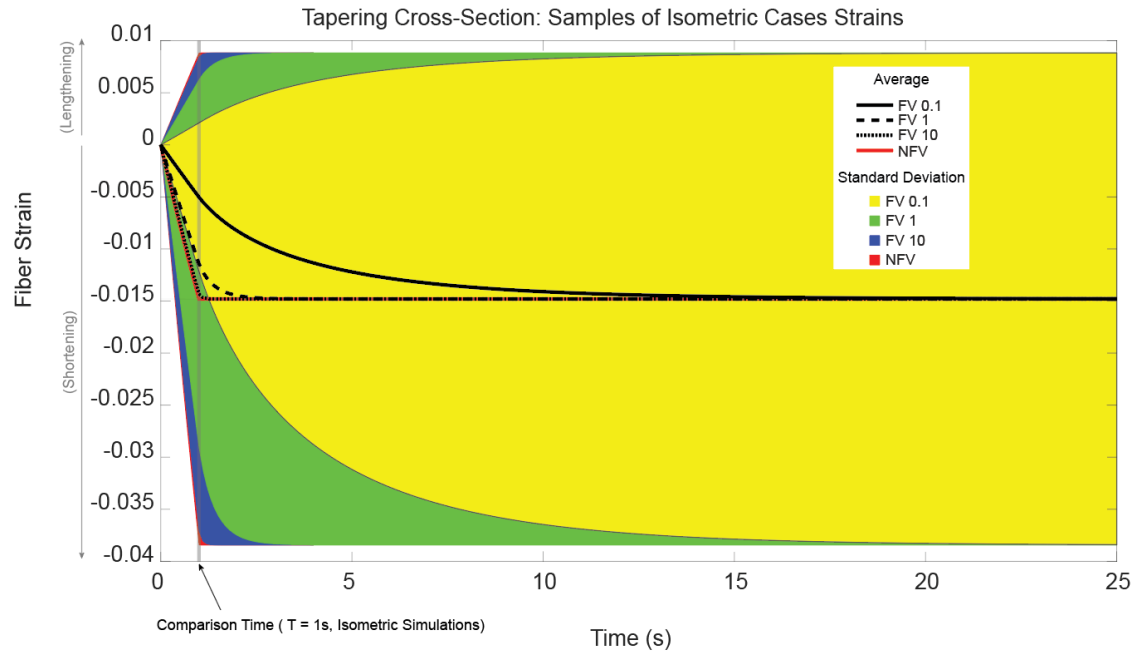


Figure 7.2: Tapering Cross-Section Model average and standard deviation fiber strain over time (1 second is the comparison point as seen in figure 4.6).

## Chapter 5

Figure 7.3 is an expanded form of the measurements of rest and phonation for the 12 participants.

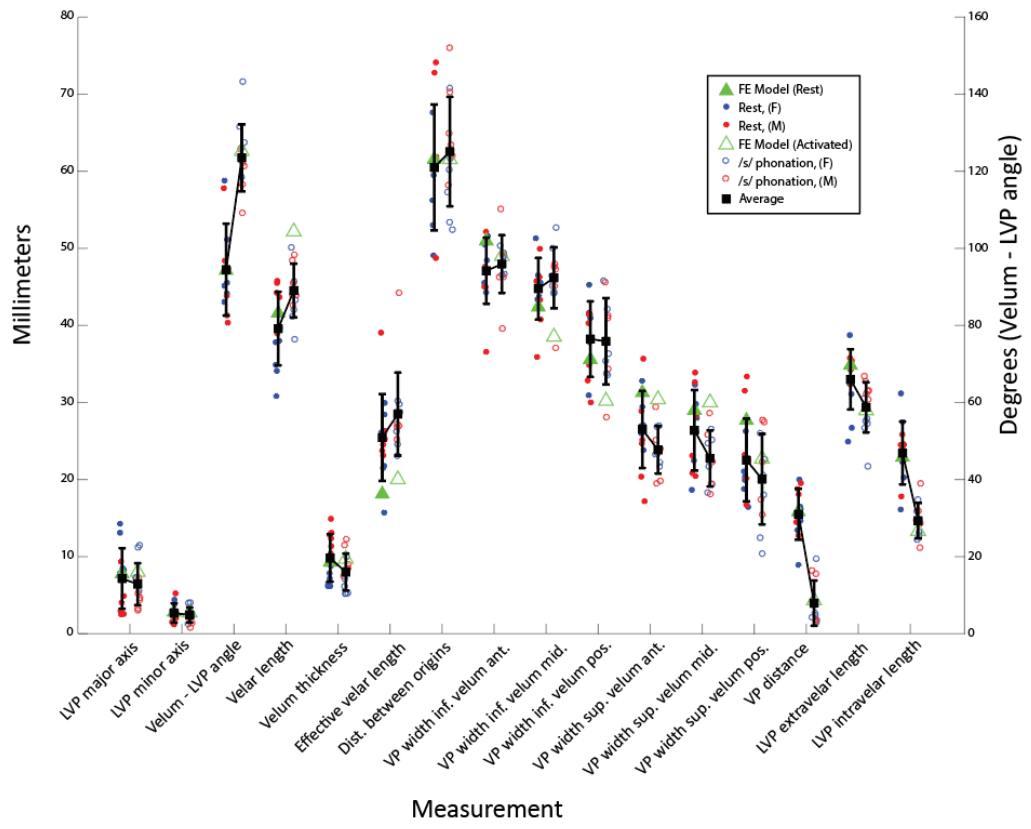


Figure 7.3: Plot showing the difference in measurements for all measurement criteria. Average and standard deviation is based on the whole participant group. Blue dots: female measurements. Red Dots: male measurements.

## Chapter 8: Citations

- Alcazar, J., Csapo, R., Ara, I., Alegre, L.M., 2019. On the Shape of the Force-Velocity Relationship in Skeletal Muscles: The Linear, the Hyperbolic, and the Double-Hyperbolic. *Front. Physiol.* 10. <https://doi.org/10.3389/fphys.2019.00769>
- Anderson, P., Fels, S., Stavness, I., Pearson, W.G., Gick, B., 2019. Intravelar and Extravelar Portions of Soft Palate Muscles in Velic Constrictions: A Three-Dimensional Modeling Study. *Journal of Speech, Language, and Hearing Research* 62, 802–814. [https://doi.org/10.1044/2018\\_JSLHR-S-17-0247](https://doi.org/10.1044/2018_JSLHR-S-17-0247)
- Aubert, K., Germaneau, A., Rochette, M., Rigoard, P., Vendeuvre, T., 2019. Personalized finite element model for full weight-bearing after tibial plateau fracture surgery. *Computer Methods in Biomechanics and Biomedical Engineering* 22, S138–S140. <https://doi.org/10.1080/10255842.2020.1714217>
- Azizi, E., Deslauriers, A.R., 2014. Regional heterogeneity in muscle fiber strain: the role of fiber architecture. *Front Physiol* 5, 303. <https://doi.org/10.3389/fphys.2014.00303>
- Bell, -Berti Fredericka, 1976. An Electromyographic Study of Velopharyngeal Function in Speech. *Journal of Speech and Hearing Research* 19, 225–240. <https://doi.org/10.1044/jshr.1902.225>
- Bennett, H.J., Rider, P.M., Domire, Z.J., DeVita, P., Kulas, A.S., 2014. Heterogeneous fascicle behavior within the biceps femoris long head at different muscle activation levels. *Journal of Biomechanics* 47, 3050–3055. <https://doi.org/10.1016/j.jbiomech.2014.06.032>
- Berry, D.A., Moon, J.B., Kuehn, D.P., 1999. A Finite Element Model of the Soft Palate. *The Cleft Palate Craniofacial Journal* 36, 217–223. [https://doi.org/10.1597/1545-1569\\_1999\\_036\\_0217\\_afemot\\_2.3.co\\_2](https://doi.org/10.1597/1545-1569_1999_036_0217_afemot_2.3.co_2)
- Best, T.M., McElhaney, J., Garrett, W.E., Myers, B.S., 1994. Characterization of the passive responses of live skeletal muscle using the quasi-linear theory of viscoelasticity. *Journal of Biomechanics* 27, 413–419. [https://doi.org/10.1016/0021-9290\(94\)90017-5](https://doi.org/10.1016/0021-9290(94)90017-5)
- Birch, M.J., Srodon, P.D., 2009. Biomechanical properties of the human soft palate. *Cleft Palate Craniofac J* 46, 268–274. <https://doi.org/10.1597/08-012.1>
- Blemker, S., Delp, S., 2005. Three-Dimensional Representation of Complex Muscle Architectures and Geometries. *Annals of Biomedical Engineering* 33, 661–673.
- Blemker, S., Pinsky, P., Delp, S., 2005. A 3D Model of Muscle Reveals the Causes of Nonuniform Strains in the Biceps Brachii. *Journal of Biomechanics* 38, 657–665.
- Bodine-Fowler, S., 1994. Skeletal muscle regeneration after injury: An overview. *Journal of Voice* 8, 53–62. [https://doi.org/10.1016/S0892-1997\(05\)80319-4](https://doi.org/10.1016/S0892-1997(05)80319-4)
- Boorman, J.G., Sommerlad, B.C., 1985. Musculus uvulae and levator palati: their anatomical and functional relationship in velopharyngeal closure. *Br J Plast Surg* 38, 333–338. [https://doi.org/10.1016/0007-1226\(85\)90237-1](https://doi.org/10.1016/0007-1226(85)90237-1)
- Bottinelli, R., Canepari, M., Pellegrino, M.A., Reggiani, C., 1996. Force-velocity properties of human skeletal muscle fibres: myosin heavy chain isoform and temperature dependence. *J Physiol* 495, 573–586.
- Chi, S.-W., Hodgson, J., Chen, J.-S., Reggie Edgerton, V., Shin, D.D., Roiz, R.A., Sinha, S., 2010. Finite element modeling reveals complex strain mechanics in the aponeuroses of

- contracting skeletal muscle. *Journal of Biomechanics* 43, 1243–1250.  
<https://doi.org/10.1016/j.jbiomech.2010.01.005>
- Choi, H.F., Chincisan, A., Magnenat-Thalmann, N., 2015. A Collective Approach for Reconstructing 3D Fiber Arrangements in Virtual Musculoskeletal Soft Tissue Models, in: Doyle, B., Miller, K., Wittek, A., Nielsen, P.M.F. (Eds.), *Computational Biomechanics for Medicine*. Springer International Publishing, Cham, pp. 117–128.  
[https://doi.org/10.1007/978-3-319-15503-6\\_11](https://doi.org/10.1007/978-3-319-15503-6_11)
- Chumanov, E.S., Heiderscheit, B.C., Thelen, D.G., 2011. Hamstring Musculotendon Dynamics during Stance and Swing Phases of High-Speed Running. *Medicine & Science in Sports & Exercise* 43, 525. <https://doi.org/10.1249/MSS.0b013e3181f23fe8>
- Chumanov, E.S., Heiderscheit, B.C., Thelen, D.G., 2007. The effect of speed and influence of individual muscles on hamstring mechanics during the swing phase of sprinting. *Journal of Biomechanics* 40, 3555–3562. <https://doi.org/10.1016/j.jbiomech.2007.05.026>
- Corona, B.T., Rivera, J.C., Owens, J.G., Wenke, J.C., Rathbone, C.R., 2015. Volumetric muscle loss leads to permanent disability following extremity trauma. *J Rehabil Res Dev* 52, 785–792. <https://doi.org/10.1682/JRRD.2014.07.0165>
- Corona, B.T., Ward, C.L., Baker, H.B., Walters, T.J., Christ, G.J., 2014. Implantation of In Vitro Tissue Engineered Muscle Repair Constructs and Bladder Acellular Matrices Partially Restore In Vivo Skeletal Muscle Function in a Rat Model of Volumetric Muscle Loss Injury. *Tissue Eng Part A* 20, 705–715. <https://doi.org/10.1089/ten.tea.2012.0761>
- Dao, T.T., Tho, M.-C.H.B., 2018a. A Systematic Review of Continuum Modeling of Skeletal Muscles: Current Trends, Limitations, and Recommendations. *Applied Bionics and Biomechanics* 2018, e7631818. <https://doi.org/10.1155/2018/7631818>
- Dao, T.T., Tho, M.-C.H.B., 2018b. A Systematic Review of Continuum Modeling of Skeletal Muscles: Current Trends, Limitations, and Recommendations [WWW Document]. *Applied Bionics and Biomechanics*. <https://doi.org/10.1155/2018/7631818>
- de Blacam, C., Smith, S., Orr, D., 2018. Surgery for Velopharyngeal Dysfunction: A Systematic Review of Interventions and Outcomes. *The Cleft Palate Craniofacial Journal* 55, 405–422. <https://doi.org/10.1177/1055665617735102>
- Dienes, J.A., Hu, X., Janson, K.D., Slater, C., Dooley, E.A., Christ, G.J., Russell, S.D., 2019. Analysis and Modeling of Rat Gait Biomechanical Deficits in Response to Volumetric Muscle Loss Injury. *Front. Bioeng. Biotechnol.* 7. <https://doi.org/10.3389/fbioe.2019.00146>
- Dolan, C.P., Dearth, C.L., Corona, B.T., Goldman, S.M., 2022a. Retrospective characterization of a rat model of volumetric muscle loss. *BMC Musculoskelet Disord* 23, 814. <https://doi.org/10.1186/s12891-022-05760-5>
- Dolan, C.P., Motherwell, J.M., Franco, S.R., Janakiram, N.B., Valerio, M.S., Goldman, S.M., Dearth, C.L., 2022b. Evaluating the potential use of functional fibrosis to facilitate improved outcomes following volumetric muscle loss injury. *Acta Biomaterialia* 140, 379–388. <https://doi.org/10.1016/j.actbio.2021.11.032>
- Dudas, J.R., Deleyiannis, F.W.B., Ford, M.D., Jiang, S., Losee, J.E., 2006. Diagnosis and Treatment of Velopharyngeal Insufficiency: Clinical Utility of Speech Evaluation and Videofluoroscopy. *Annals of Plastic Surgery* 56, 511. <https://doi.org/10.1097/01.sap.0000210628.18395.de>
- Edman, K.A., 1988. Double-hyperbolic force-velocity relation in frog muscle fibres. *J Physiol* 404, 301–321. <https://doi.org/10.1113/jphysiol.1988.sp017291>
- Ehret, A.E., Böl, M., Itskov, M., 2011. A continuum constitutive model for the active behaviour of skeletal muscle. *Journal of the Mechanics and Physics of Solids* 59, 625–636. <https://doi.org/10.1016/j.jmps.2010.12.008>

- Ekstrand, J., Healy, J.C., Waldén, M., Lee, J.C., English, B., Hägglund, M., 2012. Hamstring muscle injuries in professional football: the correlation of MRI findings with return to play. *Br J Sports Med* 46, 112–117. <https://doi.org/10.1136/bjsports-2011-090155>
- Eng, C., Smallwood, L., Pia Rainero, M., Lahey, M., Ward, S., Lieber, R., 2008. Scaling of Muscle Architecture and Fiber Types in the Rat Hindlimb. *Journal of Experimental Biology* 211, 2336–2345.
- Evangelidis, P.E., Massey, G.J., Pain, M.T.G., Folland, J.P., 2015. Biceps Femoris Aponeurosis Size: A Potential Risk Factor for Strain Injury? *Medicine & Science in Sports & Exercise* 47, 1383–1389. <https://doi.org/10.1249/MSS.0000000000000550>
- Fedorov, A., Beichel, R., Kalpathy-Cramer, J., Finet, J., Fillion-Robin, J.-C., Pujol, S., Bauer, C., Jennings, D., Fennessy, F., Sonka, M., Buatti, J., Aylward, S., Miller, J.V., Pieper, S., Kikinis, R., 2012. 3D Slicer as an image computing platform for the Quantitative Imaging Network. *Magnetic Resonance Imaging* 30, 1323–1341. <https://doi.org/10.1016/j.mri.2012.05.001>
- Fiorentino, N.M., Blemker, S.S., 2014. Musculotendon variability influences tissue strains experienced by the biceps femoris long head muscle during high-speed running. *Journal of Biomechanics* 47, 3325–3333. <https://doi.org/10.1016/j.jbiomech.2014.08.010>
- Fiorentino, N.M., Lin, J.S., Ridder, K.B., Guttman, M.A., McVeigh, E.R., Blemker, S.S., 2013. Rectus Femoris Knee Muscle Moment Arms Measured in Vivo During Dynamic Motion With Real-Time Magnetic Resonance Imaging. *Journal of Biomechanical Engineering* 135. <https://doi.org/10.1115/1.4023523>
- Fiorentino, N.M., Rehorn, M.R., Chumanov, E.S., Thelen, D.G., Blemker, S.S., 2014. Computational models predict larger muscle tissue strains at faster sprinting speeds. *Med Sci Sports Exerc* 46, 776–786. <https://doi.org/10.1249/MSS.0000000000000172>
- Garg, K., Ward, C.L., Hurtgen, B.J., Wilken, J.M., Stinner, D.J., Wenke, J.C., Owens, J.G., Corona, B.T., 2015. Volumetric muscle loss: Persistent functional deficits beyond frank loss of tissue. *Journal of Orthopaedic Research* 33, 40–46. <https://doi.org/10.1002/jor.22730>
- Garrett, W.E., Califf, J.C., Bassett, F.H., 1984. Histochemical correlates of hamstring injuries. *Am J Sports Med* 12, 98–103. <https://doi.org/10.1177/036354658401200202>
- Gillis, G.B., Biewener, A.A., 2002. Effects of surface grade on proximal hindlimb muscle strain and activation during rat locomotion. *Journal of Applied Physiology* 93, 1731–1743. <https://doi.org/10.1152/japplphysiol.00489.2002>
- Glade, R.S., Deal, R., 2016. Diagnosis and Management of Velopharyngeal Dysfunction. *Oral and Maxillofacial Surgery Clinics* 28, 181–188. <https://doi.org/10.1016/j.coms.2015.12.004>
- Greising, S.M., Corona, B.T., McGann, C., Frankum, J.K., Warren, G.L., 2019. Therapeutic Approaches for Volumetric Muscle Loss Injury: A Systematic Review and Meta-Analysis. *Tissue Engineering Part B: Reviews* 25, 510–525. <https://doi.org/10.1089/ten.teb.2019.0207>
- Greising, S.M., Warren, G.L., Southern, W.M., Nichenko, A.S., Qualls, A.E., Corona, B.T., Call, J.A., 2018. Early rehabilitation for volumetric muscle loss injury augments endogenous regenerative aspects of muscle strength and oxidative capacity. *BMC Musculoskeletal Disord* 19. <https://doi.org/10.1186/s12891-018-2095-6>
- Grogan, B.F., Hsu, J.R., Consortium, S.T.R., 2011. Volumetric Muscle Loss. *JAAOS - Journal of the American Academy of Orthopaedic Surgeons* 19, S35.
- Haenssler, A.E., Fang, X., Perry, J.L., 2020. Effective Velopharyngeal Ratio: A More Clinically Relevant Measure of Velopharyngeal Function. *J Speech Lang Hear Res* 63, 3586–3593. [https://doi.org/10.1044/2020\\_JSLHR-20-00305](https://doi.org/10.1044/2020_JSLHR-20-00305)

- Handsfield, G.G., Bolsterlee, B., Inouye, J.M., Herbert, R.D., Besier, T.F., Fernandez, J.W., 2017. Determining skeletal muscle architecture with Laplacian simulations: a comparison with diffusion tensor imaging. *Biomech Model Mechanobiol* 16, 1845–1855. <https://doi.org/10.1007/s10237-017-0923-5>
- Heiderscheit, B.C., Sherry, M.A., Silder, A., Chumanov, E.S., Thelen, D.G., 2010. Hamstring Strain Injuries: Recommendations for Diagnosis, Rehabilitation, and Injury Prevention. *Journal of Orthopaedic & Sports Physical Therapy* 40, 67–81. <https://doi.org/10.2519/jospt.2010.3047>
- Herzog, W., Lee, E.J., Rassier, D.E., 2006. Residual force enhancement in skeletal muscle. *The Journal of Physiology* 574, 635–642. <https://doi.org/10.1113/jphysiol.2006.107748>
- Hessel, A.L., Lindstedt, S.L., Nishikawa, K.C., 2017. Physiological Mechanisms of Eccentric Contraction and Its Applications: A Role for the Giant Titin Protein. *Front Physiol* 8, 70. <https://doi.org/10.3389/fphys.2017.00070>
- Hill, A.V., 1938. The heat of shortening and the dynamic constants of muscle. *Proceedings of the Royal Society of London. Series B - Biological Sciences* 126, 136–195. <https://doi.org/10.1098/rspb.1938.0050>
- Hodgson, J.A., Finni, T., Lai, A.M., Edgerton, V.R., Sinha, S., 2006. Influence of structure on the tissue dynamics of the human soleus muscle observed in MRI studies during isometric contractions. *Journal of Morphology* 267, 584–601. <https://doi.org/10.1002/jmor.10421>
- Hopper, R.A., Tse, R., Smartt, J., Swanson, J., Kinter, S., 2014. Cleft Palate Repair and Velopharyngeal Dysfunction. *Plastic and Reconstructive Surgery* 133, 852e. <https://doi.org/10.1097/PRS.0000000000000184>
- Hughes, T., 2000. *The Finite Element Method: Linear Static and Dynamic Finite Element Analysis*.
- Huxley, A.F., 1957. Muscle structure and theories of contraction. *Prog Biophys Biophys Chem* 7, 255–318.
- Inouye, J., Pelland, C., Lin, K., Borowitz, K., Blemker, S., 2015. A computational model of velopharyngeal closure for simulating cleft palate repair. *Journal of Craniofacial Surgery* 26, 658–662.
- Inouye, J.M., Lin, K.Y., Perry, J.L., Blemker, S.S., 2016. Contributions of the musculus uvulae to velopharyngeal closure quantified with a 3D multi-muscle computational model. *Ann Plast Surg* 77, S70–S75. <https://doi.org/10.1097/SAP.0000000000000777>
- Johnson, W.L., Jindrich, D.L., Roy, R.R., Reggie Edgerton, V., 2008. A three-dimensional model of the rat hindlimb: Musculoskeletal geometry and muscle moment arms. *Journal of Biomechanics* 41, 610–619. <https://doi.org/10.1016/j.jbiomech.2007.10.004>
- Jordan, H.N., Schenck, G.C., Ellis, C., Rangarathnam, B., Fang, X., Perry, J.L., 2017. Examining Velopharyngeal Closure Patterns based on Anatomic Variables. *J Craniofac Surg* 28, 270–274. <https://doi.org/10.1097/SCS.00000000000003284>
- Karalaki, M., Fili, S., Philippou, A., Koutsilieris, M., 2009. Muscle Regeneration: Cellular and Molecular Events. *In Vivo* 23, 779–796.
- Katz, B., 1939. The relation between force and speed in muscular contraction. *J Physiol* 96, 45–64. <https://doi.org/10.1113/jphysiol.1939.sp003756>
- Knaus, K.R., Handsfield, G.G., Blemker, S.S., 2022. A 3D model of the soleus reveals effects of aponeuroses morphology and material properties on complex muscle fascicle behavior. *Journal of Biomechanics* 130, 110877. <https://doi.org/10.1016/j.jbiomech.2021.110877>
- Koning, J.J.D., Molen, H.F.V.D., Woittiez, R.D., Huijing, P.A., 1987. Functional characteristics of rat gastrocnemius and tibialis anterior muscles during growth. *Journal of Morphology* 194, 75–84. <https://doi.org/10.1002/jmor.1051940107>

- Krivickas, L.S., Dorer, D.J., Ochala, J., Frontera, W.R., 2011. Relationship between force and size in human single muscle fibres. *Experimental Physiology* 96, 539–547. <https://doi.org/10.1113/expphysiol.2010.055269>
- Kruse, A., Rivas, C., Weide, G., Tilp, M., Jaspers, R.T., 2021. Stimuli for Adaptations in Muscle Length and the Length Range of Active Force Exertion—A Narrative Review. *Front Physiol* 12, 742034. <https://doi.org/10.3389/fphys.2021.742034>
- Kuehn, D.P., Folkins, J.W., Cutting, C.B., 1982. Relationships Between Muscle Activity and Velar Position. *The Cleft Palate Journal* 19, 25–35.
- Kummer, A.W., 2011. Types and Causes of Velopharyngeal Dysfunction. *Semin Speech Lang* 32, 150–158. <https://doi.org/10.1055/s-0031-1277717>
- Lam, D.J., Starr, J.R., Perkins, J.A., Lewis, C.W., Eblen, L.E., Dunlap, J., Sie, K.C.Y., 2006. A Comparison of Nasendoscopy and Multiview Videofluoroscopy in Assessing Velopharyngeal Insufficiency. *Otolaryngol Head Neck Surg* 134, 394–402. <https://doi.org/10.1016/j.otohns.2005.11.028>
- Lambertz, D., Perot, C., Almeida-Silveira, M.I., Goubel, F., 2000. Changes in stiffness induced by hindlimb suspension in rat Achilles tendon. *European Journal of Applied Physiology* 81, 252–257. <https://doi.org/10.1007/s004210050039>
- Langridge, B., Griffin, M., Butler, P.E., 2021. Regenerative medicine for skeletal muscle loss: a review of current tissue engineering approaches. *J Mater Sci: Mater Med* 32, 15. <https://doi.org/10.1007/s10856-020-06476-5>
- Leahy, T.P., Nuss, C.A., Evans, M.K., Fung, A.K., Shetye, S.S., Soslowsky, L.J., 2022. Achilles Tendon Ruptures in Middle-Aged Rats Heal Poorly Compared With Those in Young and Old Rats. *Am J Sports Med* 50, 170–181. <https://doi.org/10.1177/03635465211055476>
- Leitner, C., Vostrikov, S., Tilp, M., Hager, P.A., Cossettini, A., Benini, L., Baumgartner, C., 2020. Human Fascicle Strain Behavior During Twitch using Ultrafast Ultrasound, in: 2020 IEEE International Ultrasonics Symposium (IUS). Presented at the 2020 IEEE International Ultrasonics Symposium (IUS), pp. 1–4. <https://doi.org/10.1109/IUS46767.2020.9251488>
- Lieber, R.L., Fridén, J., 1988. Selective damage of fast glycolytic muscle fibres with eccentric contraction of the rabbit tibialis anterior. *Acta Physiologica Scandinavica* 133, 587–588. <https://doi.org/10.1111/j.1748-1716.1988.tb08446.x>
- Lieber, R.L., Ward, S.R., 2011. Skeletal muscle design to meet functional demands. *Philosophical Transactions of the Royal Society B: Biological Sciences* 366, 1466–1476. <https://doi.org/10.1098/rstb.2010.0316>
- Lim, J.-Y., Choi, S.J., Widrick, J.J., Phillips, E.M., Frontera, W.R., 2019. Passive force and viscoelastic properties of single fibers in human aging muscles. *Eur J Appl Physiol* 119, 2339–2348. <https://doi.org/10.1007/s00421-019-04221-7>
- Lin, H.-C., Cheng, C.-H., Chen, G., 2019. The prevalence of Passavant’s ridge in patients with velopharyngeal insufficiency in a Taiwan Chinese population. *J Dent Sci* 14, 15–20. <https://doi.org/10.1016/j.jds.2018.10.002>
- Maas, H., Baan, G.C., Huijing, P.A., Yucesoy, C.A., Koopman, B.H.F.J.M., Grootenboer, H.J., 2003. The Relative Position of EDL Muscle Affects the Length of Sarcomeres Within Muscle Fibers: Experimental Results and Finite-Element Modeling. *Journal of Biomechanical Engineering* 125, 745–753. <https://doi.org/10.1115/1.1615619>
- Maas, S.A., Ellis, B.J., Ateshian, G.A., Weiss, J.A., 2012. FEBio: finite elements for biomechanics. *J Biomech Eng* 134, 011005. <https://doi.org/10.1115/1.4005694>
- Maas, S.A., LaBelle, S.A., Ateshian, G.A., Weiss, J.A., 2018. A Plugin Framework for Extending the Simulation Capabilities of FEBio. *Biophysical Journal* 115, 1630–1637. <https://doi.org/10.1016/j.bpj.2018.09.016>

- Mahdy, M.A.A., 2019. Skeletal muscle fibrosis: an overview. *Cell Tissue Res* 375, 575–588. <https://doi.org/10.1007/s00441-018-2955-2>
- Marcucci, L., Reggiani, C., Natali, A.N., Pavan, P.G., 2017. From single muscle fiber to whole muscle mechanics: a finite element model of a muscle bundle with fast and slow fibers. *Biomech Model Mechanobiol* 16, 1833–1843. <https://doi.org/10.1007/s10237-017-0922-6>
- Marsh, J.L., 2004. The evaluation and management of velopharyngeal dysfunction. *Clinics in Plastic Surgery* 31, 261–269. [https://doi.org/10.1016/S0094-1298\(03\)00124-X](https://doi.org/10.1016/S0094-1298(03)00124-X)
- Mason, K.N., 2024. Magnetic Resonance Imaging for Assessing Velopharyngeal Function: Current Applications, Barriers, and Potential for Future Clinical Translation in the United States. *The Cleft Palate Craniofacial Journal* 61, 235–246. <https://doi.org/10.1177/10556656221123916>
- Mason, K.N., Black, J., 2023. Incorporating Velopharyngeal MRI into the Clinical Decision-Making Process for a Patient Presenting with Velopharyngeal Dysfunction Following a Failed Palatoplasty. *The Cleft Palate Craniofacial Journal* 10556656231173500. <https://doi.org/10.1177/10556656231173500>
- Mason, K.N., Perry, J.L., Riski, J.E., Fang, X., 2016. Age related changes between the level of velopharyngeal closure and the cervical spine. *J Craniofac Surg* 27, 498–503. <https://doi.org/10.1097/SCS.0000000000002403>
- Mintz, E.L., Passipieri, J.A., Franklin, I.R., Toscano, V.M., Afferton, E.C., Sharma, P.R., Christ, G.J., 2020. Long-Term Evaluation of Functional Outcomes Following Rat Volumetric Muscle Loss Injury and Repair. *Tissue Engineering Part A* 26, 140–156. <https://doi.org/10.1089/ten.tea.2019.0126>
- Mintz, E.L., Passipieri, J.A., Lovell, D.Y., Christ, G.J., 2016. Applications of In Vivo Functional Testing of the Rat Tibialis Anterior for Evaluating Tissue Engineered Skeletal Muscle Repair. *JoVE (Journal of Visualized Experiments)* e54487. <https://doi.org/10.3791/54487>
- Moncayo-Matute, F.P., Peña-Tapia, P.G., Vázquez-Silva, E., Torres-Jara, P.B., Moya-Loaiza, D.P., Abad-Farfán, G., Andrade-Galarza, A.F., 2022. Surgical planning and finite element analysis for the neurocraneal protection in cranioplasty with PMMA: A case study. *Heliyon* 8, e10706. <https://doi.org/10.1016/j.heliyon.2022.e10706>
- Morgan, D.L., 1990. New insights into the behavior of muscle during active lengthening. *Biophysical Journal* 57, 209–221. [https://doi.org/10.1016/S0006-3495\(90\)82524-8](https://doi.org/10.1016/S0006-3495(90)82524-8)
- Morgan, D.L., Proske, U., 2006. Sarcomere popping requires stretch over a range where total tension decreases with length. *J Physiol* 574, 627–628. <https://doi.org/10.1113/jphysiol.2006.574201>
- Mukund, K., Subramaniam, S., 2020. Skeletal muscle: A review of molecular structure and function, in health and disease. *Wiley Interdiscip Rev Syst Biol Med* 12, e1462. <https://doi.org/10.1002/wsbm.1462>
- Nam, S.M., 2018. Surgical treatment of velopharyngeal insufficiency. *Arch Craniofac Surg* 19, 163–167. <https://doi.org/10.7181/acfs.2018.02082>
- Nickel, M., Scheer, C., Hammel, J.U., Herzen, J., Beckmann, F., 2011. The contractile sponge epithelium sensu lato – body contraction of the demosponge *Tethya wilhelma* is mediated by the pinacoderm. *Journal of Experimental Biology* 214, 1692–1698. <https://doi.org/10.1242/jeb.049148>
- Pappas, G.P., Asakawa, D.S., Delp, S.L., Zajac, F.E., Drace, J.E., 2002. Nonuniform shortening in the biceps brachii during elbow flexion. *Journal of Applied Physiology* 92, 2381–2389. <https://doi.org/10.1152/jappphysiol.00843.2001>

- Passipieri, J.A., Baker, H.B., Siriwardane, M., Ellenburg, M., Vadhavkar, M., Saul, J., Tomblyn, S., Burnett, L., Christ, G., 2017. Keratin Hydrogel Enhances In Vivo Skeletal Muscle Function in a Rat Model of Volumetric Muscle Loss. *Tissue Engineering: Part A* 23, 556.
- Passipieri, J.A., Hu, X., Mintz, E., Dienes, J., Baker, H.B., Wallace, C.H., Blemker, S.S., Christ, G.J., 2019. In Silico and In Vivo Studies Detect Functional Repair Mechanisms in a Volumetric Muscle Loss Injury. *Tissue Engineering Part A*.  
<https://doi.org/10.1089/ten.tea.2018.0280>
- Perry, J.L., 2011. Anatomy and Physiology of the Velopharyngeal Mechanism. *Semin Speech Lang* 32, 83–92. <https://doi.org/10.1055/s-0031-1277712>
- Perry, J.L., Mason, K., Sutton, B.P., Kuehn, D.P., 2018. Can Dynamic MRI Be Used to Accurately Identify Velopharyngeal Closure Patterns? *The Cleft Palate Craniofacial Journal* 55, 499–507. <https://doi.org/10.1177/1055665617735998>
- Perry, J.L., Sutton, B.P., Kuehn, D.P., Gamage, J.K., 2014. Using MRI for Assessing Velopharyngeal Structures and Function. *Cleft Palate Craniofac J* 51, 476–485.  
<https://doi.org/10.1597/12-083>
- Proske, U., Morgan, D., Brockett, C., Percival, P., 2004. Identifying Athletes at Risk of Hamstring Strains and How to Protect Them. *Clinical and Experimental Pharmacology and Physiology* 31, 546–550. <https://doi.org/10.1111/j.1440-1681.2004.04028.x>
- Rahemi, H., Nigam, N., Wakeling, J.M., 2015. The effect of intramuscular fat on skeletal muscle mechanics: implications for the elderly and obese. *Journal of The Royal Society Interface* 12, 20150365. <https://doi.org/10.1098/rsif.2015.0365>
- Rassier, D.E., 2008. Pre-power stroke cross bridges contribute to force during stretch of skeletal muscle myofibrils. *Proc Biol Sci* 275, 2577–2586.  
<https://doi.org/10.1098/rspb.2008.0719>
- Rassier, D.E., Herzog, W., 2004. Considerations on the history dependence of muscle contraction. *J Appl Physiol* (1985) 96, 419–427.  
<https://doi.org/10.1152/jappphysiol.00653.2003>
- Rehorn, M.R., Blemker, S.S., 2010. The effects of aponeurosis geometry on strain injury susceptibility explored with a 3D muscle model. *Journal of Biomechanics* 43, 2574–2581.  
<https://doi.org/10.1016/j.jbiomech.2010.05.011>
- Rehorn, M.R., Schroer, A.K., Blemker, S.S., 2014. The passive properties of muscle fibers are velocity dependent. *J Biomech* 47, 687–693.  
<https://doi.org/10.1016/j.jbiomech.2013.11.044>
- Röhrle, O., Pullan, A.J., 2007. Three-dimensional finite element modelling of muscle forces during mastication. *Journal of Biomechanics* 40, 3363–3372.  
<https://doi.org/10.1016/j.jbiomech.2007.05.011>
- Roots, H., Offer, G.W., Ranatunga, K.W., 2007. Comparison of the tension responses to ramp shortening and lengthening in intact mammalian muscle fibres: crossbridge and non-crossbridge contributions. *J Muscle Res Cell Motil* 28, 123–139.  
<https://doi.org/10.1007/s10974-007-9110-0>
- Ross, S.A., Domínguez, S., Nigam, N., Wakeling, J.M., 2021. The Energy of Muscle Contraction. III. Kinetic Energy During Cyclic Contractions. *Frontiers in Physiology* 12.
- Ross, S.A., Wakeling, J.M., 2016. Muscle shortening velocity depends on tissue inertia and level of activation during submaximal contractions. *Biol Lett* 12, 20151041.  
<https://doi.org/10.1098/rsbl.2015.1041>
- Schiaffino, S., Reggiani, C., 2011. Fiber Types in Mammalian Skeletal Muscles. *Physiological Reviews* 91, 1447–1531. <https://doi.org/10.1152/physrev.00031.2010>

- Schneider, C.A., Rasband, W.S., Eliceiri, K.W., 2012. NIH Image to ImageJ: 25 years of image analysis. *Nat Methods* 9, 671–675. <https://doi.org/10.1038/nmeth.2089>
- Sefton, E.M., Kardon, G., 2019. Connecting muscle development, birth defects, and evolution: An essential role for muscle connective tissue. *Curr Top Dev Biol* 132, 137–176. <https://doi.org/10.1016/bs.ctdb.2018.12.004>
- Shadi, M.S., Hegazi, M.A., Ghandour, H.H., Othman, N.M., Khaled, D.M., 2022. Patterns of velopharyngeal closure during speech in individuals with normal habitual resonance: A nasoendoscopic analysis. *Auris Nasus Larynx* 49, 995–1002. <https://doi.org/10.1016/j.anl.2022.04.002>
- Shprintzen, R.J., Marrinan, E., 2009. Velopharyngeal insufficiency: diagnosis and management. *Curr Opin Otolaryngol Head Neck Surg* 17, 302–307. <https://doi.org/10.1097/MOO.0b013e32832cbd6b>
- Soman, A., Hedrick, T.L., Biewener, A.A., 2005. Regional patterns of pectoralis fascicle strain in the pigeon *Columba livia* during level flight. *Journal of Experimental Biology* 208, 771–786. <https://doi.org/10.1242/jeb.01432>
- Srodon, P.D., Miquel, M.E., Birch, M.J., 2012. Finite Element Analysis Animated Simulation of Velopharyngeal Closure. *The Cleft Palate-Craniofacial Journal* 49, 44–50. <https://doi.org/10.1597/10-131>
- Standring, Susan, 2021. Pharynx, in: *Gray's Anatomy: The Anatomical Basis of Clinical Practice*. Elsevier.
- Steinmetz, P.R.H., Kraus, J.E.M., Larroux, C., Hammel, J.U., Amon-Hassenzahl, A., Houliston, E., Wörheide, G., Nickel, M., Degnan, B.M., Technau, U., 2012. Independent evolution of striated muscles in cnidarians and bilaterians. *Nature* 487, 231–234. <https://doi.org/10.1038/nature11180>
- Stienen, G.J., Versteeg, P.G., Papp, Z., Elzinga, G., 1992. Mechanical properties of skinned rabbit psoas and soleus muscle fibres during lengthening: effects of phosphate and Ca<sup>2+</sup>. *J Physiol* 451, 503–523.
- Sullivan, S.R., Taylor, H.O.B., Stiles, E., Nuss, R.C., Balkin, D.M., Mulliken, J.B., 2023. Videofluoroscopy Versus Nasopharyngoscopy of Lateral Pharyngeal Wall Movement for Assessment of Velopharyngeal Insufficiency. *Journal of Craniofacial Surgery* 34, 40. <https://doi.org/10.1097/SCS.00000000000008945>
- Testa, S., Fornetti, E., Fuoco, C., Sanchez-Riera, C., Rizzo, F., Ciccotti, M., Cannata, S., Sciarra, T., Gargioli, C., 2021. The War after War: Volumetric Muscle Loss Incidence, Implication, Current Therapies and Emerging Reconstructive Strategies, a Comprehensive Review. *Biomedicine* 9, 564. <https://doi.org/10.3390/biomedicine9050564>
- Tidball, J.G., 2011. Mechanisms of Muscle Injury, Repair, and Regeneration, in: *Comprehensive Physiology*. John Wiley & Sons, Ltd, pp. 2029–2062. <https://doi.org/10.1002/cphy.c100092>
- Timmins, R.G., Shield, A.J., Williams, M.D., Lorenzen, C., Opar, D.A., 2015. Biceps Femoris Long Head Architecture: A Reliability and Retrospective Injury Study. *Medicine & Science in Sports & Exercise* 47, 905. <https://doi.org/10.1249/MSS.0000000000000507>
- Tran, T., Perry, J., Blemker, S., Mason, K., 2022. Simulation of Velopharyngeal Biomechanics Identifies Differences in Sphincter Pharyngoplasty Outcomes: A Matched Case–Control Study. *The Cleft Palate Craniofacial Journal* 10556656221122634. <https://doi.org/10.1177/10556656221122634>
- Vafek, E.C., Plate, J.F., Friedman, E., Mannava, S., Scott, A.T., Danelson, K.A., 2018. The effect of strain and age on the mechanical properties of rat Achilles tendons. *Muscles Ligaments Tendons J* 7, 548–553. <https://doi.org/10.11138/mltj/2017.7.3.548>

- Watterson, T., Wendel, J., Grames, L.M., Warner, A., 2021. The Reliability of Visual Ratings of Velopharyngeal Physiology for Speech. *The Cleft Palate Craniofacial Journal* 58, 546–556. <https://doi.org/10.1177/1055665620961911>
- Weidner, S., Tomalka, A., Rode, C., Siebert, T., 2022. How velocity impacts eccentric force generation of fully activated skinned skeletal muscle fibers in long stretches. *Journal of Applied Physiology* 133, 223–233. <https://doi.org/10.1152/jappphysiol.00735.2021>
- Westman, A.M., Dyer, S.E., Remer, J.D., Hu, X., Christ, G.J., Blemker, S.S., 2019. A coupled framework of in situ and in silico analysis reveals the role of lateral force transmission in force production in volumetric muscle loss injuries. *Journal of Biomechanics* 85, 118–125. <https://doi.org/10.1016/j.jbiomech.2019.01.025>
- Woo, A.S., 2012. Velopharyngeal Dysfunction. *Semin Plast Surg* 26, 170–177. <https://doi.org/10.1055/s-0033-1333882>
- Wu, X., Corona, B., Chen, X., Walters, T., 2012. A Standardized Model of Volumetric Muscle Loss Injury for the Development of Tissue Engineering Therapies. *BioResearch open access* 1.
- Young, A., Spinner, A., 2024. Velopharyngeal Insufficiency, in: *StatPearls*. StatPearls Publishing, Treasure Island (FL).
- Zajac, F.E., 1989. Muscle and tendon: properties, models, scaling, and application to biomechanics and motor control. *Crit Rev Biomed Eng* 17, 359–411.
- Zhong, X., Epstein, F.H., Spottiswoode, B.S., Helm, P.A., Blemker, S.S., 2008. Imaging two-dimensional displacements and strains in skeletal muscle during joint motion by cine DENSE MR. *Journal of Biomechanics* 41, 532–540. <https://doi.org/10.1016/j.jbiomech.2007.10.026>